Accretion disc reverberation mapping of the narrow-line Seyfert 1 galaxy Mrk 1239

DAKSHESH KOLOLGI

Accretion disc reverberation mapping of the narrow-line Seyfert 1 galaxy Mrk 1239

Dakshesh Kololgi

A thesis presented for the degree of

Master of Physics

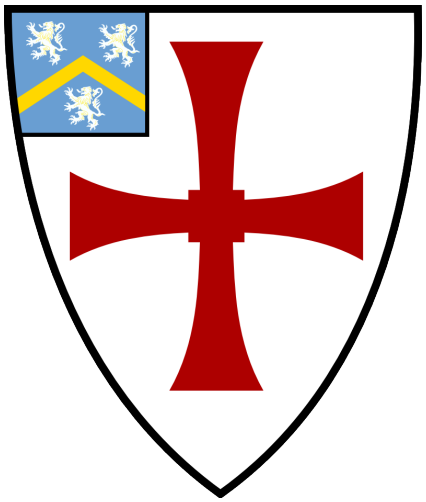

Centre for Extragalactic Astronomy

The University of Durham

United Kingdom

November 2023

Abstract

Accretion allows the SMBHs that power AGN to grow across cosmic time and it plays a major role in the formation history of galaxies. Small angular sizes and large distances prevent us from studying AGN through direct imaging, however, inferring their geometry can be achieved through reverberation mapping. By substituting spatial resolution for time resolution, the variable nature of AGN emission can be exploited to study AGN beyond the reach of direct imaging techniques. Many recent investigations have revealed a discrepancy with theoretical accretion disc models, specifically the Shakura-Sunyaev thin disc model. These studies find that although the lag spectrum follows the expected $\tau \propto \lambda^{\frac{4}{3}}$ relation the lags and therefore disc sizes are larger on average by a factor of 4.41, 4.29, and 3.27 than the theoretical thin disc lags for Sour, Javelin and PyROA respectively when the u band is set as the driver.

The first investigation in this thesis outlines a comprehensive comparison of Javelin and PyROA, which are modern reverberation mapping algorithms that extract time lags to a higher precision than the legacy cross-correlation methods. We find consistency between all three algorithms and with existing data after implementing qualitative parameter optimisations to reduce effects such as aliasing and contamination from unexpected emissions. We then applied this knowledge to optical light curves for a reverberation mapping study of the highly obscured AGN, Mrk

1239. In line with several other studies, we observe that the lag spectrum is consistent with the expected $\frac{4}{3}$ power law but that the observed lags are a factor of $3-4$ larger than the thin disc prediction. When the u band was set as the driver, $\tau_{\lambda_0} = 2.50 \pm 2.63$ days with an unfixed power law $\beta = 0.93 \pm 0.70$ and $\tau_{\lambda_0} = 1.46 \pm 0.12$ days for a fixed $\beta = \frac{4}{3}$. These lag estimates are 0.34σ and 2.5σ from the theoretical disc size estimate at the driving wavelength of 1.61. A better understanding of the systematics of Sour, Javelin and PyROA must be undertaken because some values are inconsistent between the algorithms. Furthermore, we attempted to connect the unusually flat spectral shape, which according to the thin disc model should be $F_\nu \propto \lambda^{\frac{4}{3}}$ of the disc component spectrum (reconstructed from the flux decomposition of the light curves). However, a rimmed disc model was not able to reconcile the flat spectral shape with the observed lags and we conclude that the spectral shape is a result of dust extinction that is non-disc in origin, most likely originating from a thick dusty torus that covers the disc emission. A thin disc model fits the unreddened disc spectrum well with an Eddington ratio of $\dot{m} \approx 0.3$, resulting in a larger-than-expected disc size. Applying the rimmed disc model to the unreddened fluxes again with an Eddington ratio of $\dot{m} \approx 0.3$ was able to reconcile the spectral shape as well as the disc sizes in the u, B, and g' bands, we find that the observed lags are smaller than the rimmed disc model by a factor of $3-5$ for the r', i', and z_s bands. This is the first reverberation mapping study of an obscured AGN and we sought to connect Mrk 1239's spectral properties with the scales of structures observed with reverberation mapping to further our understanding of accretion discs and the processes within AGN in the context of the unified model.

Supervisors: Dr Hermine Landt-Wilman and Dr Simone Scaringi

Acknowledgements

I would like to thank Dr Hermine Landt-Wilman, Dr Simone Scaringi, my friends and family for their invaluable support and guidance during this past year, and for enabling me to realise my dreams of becoming a physicist.

Contents

Declaration

The work in this thesis is based on research carried out at the Centre for Extragalactic Astronomy, Department of Physics, University of Durham, England. No part of this thesis has been submitted elsewhere for any other degree or qualification, and it is the sole work of the author unless referenced to the contrary in the text.

List of Figures

List of Tables

Nomenclature

AGN Active galactic nucleus

AGN Active galactic nuclei

SMBH Supermassive black hole

BEL Broad emission line

NEL Narrow emission line

BLR Broad line region

NLR Narrow line region

UV Ultraviolet

Chapter 1

Introduction

1.1 AGN and The Unified Model

Active galactic nuclei or AGN are regions on the order of $1\,pc$ at the centre of some galaxies whose extreme luminosities cannot be explained by stellar densities alone. AGN emit radiation across the entire electromagnetic spectrum, from radio waves through to gamma rays, often even outshining their host galaxy (ESA/Hubble, 2023). Galaxies that contain AGN are known as 'active' galaxies. AGN are the most luminous persistent sources of electromagnetic radiation in the Universe and are powered by matter in-falling into a supermassive black hole (SMBH). Due to their extreme luminosities, the radiation released by AGN, in the form of winds and radio plasma jets, plays a crucial role in galactic evolution (Morganti, 2017) in a process known as AGN feedback. Additionally, they provide an important tool to track the evolution of the Universe, providing observational insight into the presence of supermassive black holes early in the Universe's history - challenging the timeline proposed by ΛCDM. Most recently, the CEERS survey discovered CEERS_1019, an actively accreting SMBH with mass $10^{6.95}$ $\mathrm{M}_\odot$ just 500 Myr ($z = 8.679$) after the big bang (Larson et al., 2023) accreting at $1.2\times$ the Eddington limit. AGN can be roughly defined as containing an SMBH with an Eddington ratio (ratio of bolometric AGN luminosity and the Eddington luminosity) exceeding $\frac{L_{Bolometric}}{L_{Edd}} = 10^{-5}$, where $L_{Edd} = 1.5 \times 10^8 \ \frac{\mathrm{M_{BH}}}{\mathrm{M}_\odot}$ Netzer (2015) for a solar

composition gas. The classic model for AGN morphology is characterised by the components;

- Subparsec accretion disc: Optically thick and can be geometrically thin or thick.
- Broad-line region (BLR): $1000\,\mathrm{Km\,s^{-1}}$ width, high-density, dust-free molecular gas clouds at Keplerian velocities.
- Narrow line region (NLR): $500\,\mathrm{Km\,s^{-1}}$, lower-density, lower-velocity ionised gas.
- Dusty torus: axisymmetric dusty structure $0.1 - 10\,\mathrm{pc}$ in minor diameter.
- Radio jet: some AGN contain collimated radio jets perpendicular to the plane of the accretion disc that can reach up to $\sim 1\,\mathrm{Mpc}$ scales in size.

The two main types of AGN (type 1 and type 2) are distinguished by the presence of broad emission lines (BEL) arising from the broad line region (BLR) in type 1 AGN and their lack of presence in type 2 AGN. The lack of BELs in type 2 AGN is explained through the inclination angle of the orbital plane around the SMBH with respect to an observer; the dusty torus is thick so that at some inclination angles it covers the emission from the accretion disc and BLR. Thus, the BELs vanish as the emission is largely absorbed by dust and only narrow emission lines (NELs) remain. The existence of a dusty torus is hinted at by several photometric NIR RM campaigns (Koshida et al., 2014) reveal IR bands lag on a timescale of a few months to a year, which is significantly longer than the timescales of a few days for the UV-optical continuum—indicating a structure at the outer edge of the AGN. The NIR lag timescales of a few months to a year corroborate the existence of a dusty structure because for a viscous thin disc the temperature profile predicts that the temperature should fall lower than the dust sublimation temperature 2000 K. Ongoing attempts are being made to explain the several observed types of AGN

by varying the basic properties outlined thus far and accounting for their luminosities into a unified model (figure 1.1). Understanding the structure of AGN helps develop an intuition for the emission and variability characteristics of AGN so that each component's emission can be related to observed spectra and how variability from one component can be delayed in time with respect to others. Leading to a unified and comprehensive understanding of AGN morphologies.

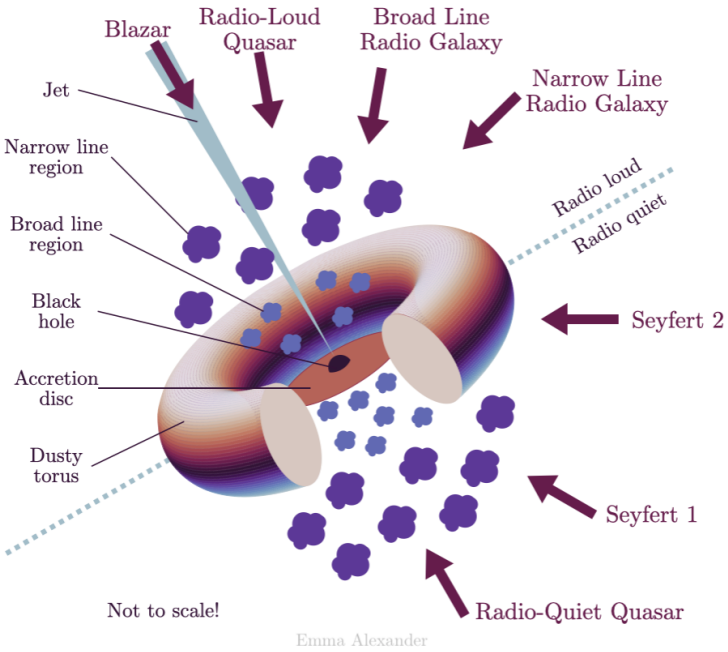

Figure 1.1: Unified model of AGN with arrows showing how the viewing angle determines the type of AGN. The dashed line illustrates the different possibilities of radio-loud/quiet AGN Emma Alexander (2023).

It remains an enigma as to how massive SMBHs such as CEERS_1019 could have formed in less than 1 Gyr. Accretion seems to be vital to the growth of supermassive black holes (SMBHs), powering AGN, the most luminous sources in the Universe (Salpeter, 1964). The process of accretion is thought to funnel matter into the SMBH through the accretion disc, thought to be geometrically thin and optically thick (Shakura and Sunyaev, 1973) when sufficiently below the Eddington limit. Alternatively, the super-Eddington limit is an area of active study and is thought to play a role in the early mass growth of SMBHs (Du et al., 2016;

Pacucci et al., 2017; Regan et al., 2019; Donnan et al., 2023). At this limit, photon pressure becomes significant and the disc thickness increases to that of a 'slim' disc as shown by Abramowicz et al. (1988). Understanding how accretion allows black hole masses to grow is a key component in the presence of high-mass black holes and the evolution of their host galaxies. Ultimately, studying AGN and accretion places constraints on ΛCDM.

1.1.1 Black Hole Accretion

AGN power is thought to be fuelled by accretion, in-falling matter liberating gravitational potential energy. For supermassive black holes greater than $10^8\,\mathrm{M}_\odot$, accretion is described by Bondi accretion (Bondi and Hoyle, 1944) or spherical accretion by a compact object in a medium of gas. The in-falling matter traverses tendex line trajectories, a slow inward spiral, due to the viscous shear stresses this matter forms a continuous disc of matter localised to a $2-D$ orbital plane (with thickness r negligible compared to the disc radius R, $r << R$) radiating away energy, which in turn reduces its angular momentum allowing for the inward spiral. Accretion discs facilitate the growth of SMBHs and the large luminosities of AGN.

The rate of inward flow is regulated by outward radiation pressure from radiation emitted by the viscous heating of gas in the disc, resulting in the Eddington limit for luminosity. This is the maximum limit a body can achieve when there is a balance between radiation acting outwards and gravitational force acting inwards. Each radius of the disc exists in local thermodynamic equilibrium and emits a black body with a characteristic temperature. In general, the opacity of the gas is highly frequency-dependent and a function of the physical state of the gas. Calculating the radiation pressure can be simplified by assuming the gas is completely ionised and composed of hydrogen so that the opacity is given by Thomson scattering, the elastic scattering (in the limit $\frac{h\nu}{m_e c^2} \rightarrow 0$, valid for all photon energies below

100 keV) of electromagnetic radiation by a charged particle (for further details see Krolik (1999)). This results in the Eddington luminosity in equation 1.1 that depends only on the mass of the radiating object. Where m_p and σ_T are the proton mass and the Thomson scattering cross-section respectively.

$$L_{Edd} = \frac{4\pi G M_{SMBH}\, c\, m_p}{\sigma_T} \tag{1.1}$$

The Eddington luminosity implies a limiting rate for which matter can be accreted because the luminosity of the disc is a result of in-falling matter. Therefore, a fraction ϵ of the accreting rest mass energy is converted into radiation through the release of gravitational potential energy (equation 1.2). ϵ is known as the radiative efficiency.

$$L = \epsilon \dot{M} c^2 \tag{1.2}$$

$$\dot{M}_{Edd} = \frac{4\pi M_{SMBH}\, m_p}{\epsilon c \sigma_T} \tag{1.3}$$

Equation 1.2 suggests the existence of a self-regulating inward flow of matter in a thin accretion disc. The accretion cannot be higher than implied by equation 1.3, otherwise matter will be blown away by radiation pressure. We assume a radiative efficiency of $\epsilon \sim 0.1$ when calculating Eddington ratios based on the Soltan argument (Davis and Laor, 2011) which states that, over a Hubble time, the SMBHs that power quasars accrete gas as well as stars to grow to masses we see today, this results in a predictable number density of quasars which has shown to be verified by Yu and Tremaine (2002). However, it is possible for super-Eddington accretion (observed from reverberation mapping by Cackett et al. (2020)); observationally so if the SMBH accretes and radiates at high efficiency or if the SMBH radiates with a low efficiency so that $L < L_{Edd}$ in an advection dominated scenario.

1.1.2 Accretion Disc Structure and Variability

Infalling matters requires a loss of gravitational potential energy as well as angular momentum. Due to angular momentum conservation, there must be a corresponding increase of angular momentum of matter for a given infall. For example, the specific angular momentum of matter at the innermost stable circular orbit (ISCO) of a black hole is 4 orders of magnitude smaller than in the orbit of a typical galaxy (Krolik, 1999) and therefore, accretion hinges on eliminating all but a small fraction of a given piece of matter's initial angular momentum. Matter is expected to fall into a common orbital plane (forming an accretion disc) because matter travelling on orbits inclined with respect to one another will collide in the plane of intersection, thereby the momenta of matter normal to the plane of intersection will cancel each other out. Eventually, these collisions stabilise matter originating with different angular momenta into a disc where each orbital radius has the same specific momentum. For luminosities $L << L_{Edd}$ radiation pressure alone cannot support the matter against gravity and the system is two-dimensional because the vertical thickness is much smaller than the disc radius as there is not enough radiation pressure to support a thick disc against gravity at substantial altitudes above the disc plane. The opposite is true when $\frac{L}{L_{Edd}} \sim 1$ where the disc scale height may be comparable to the disc radius.

In the Shakura-Sunyaev thin accretion disc, the in-falling matter is assumed to be an optically thick, molecular gas (Shakura and Sunyaev, 1973). The local emission can be approximated as a blackbody spectra, with a characteristic temperature, T (and emission wavelength, λ_{max}, from Wien's displacement law) that is a function of the radius, r, from the SMBH centre. Several accretion disc models have been proposed that range from the standard thin disc Shakura-Sunyaev model (Shakura and Sunyaev, 1973), to advection-dominated accretion discs (Narayan and Yi, 1995) and relativistic accretion discs (Li et al., 2005). All contain the same concept of an

accretion disc temperature profile, with the highest temperatures present near the innermost stable circular orbit and decreasing temperatures as the radius increases.

The α-disc model proposed by Shakura and Sunyaev (1973) proposed that turbulence-enhanced viscosity was the mechanism by which angular momentum could be efficiently transferred outwards. Whereby the effective viscosity is parameterised by $\nu_\alpha = \alpha c_s h$. Where c_s and h are the sound speed and scale height respectively. α is a parameter between 0 and 1 with 0 representing no accretion. The thinness of an accretion disc is defined by equation 7.2 in Krolik (1999). Gravitational potential energy is released by infalling matter at a rate of $L = \frac{GM\dot{M}}{R}$. However, from the virial theorem, half of this goes into the local heating of gas and the other half is radiated away as the observed luminosity (Peterson, 1997).

$$L = \frac{GM\dot{M}}{2R} = 2\pi R^2 \sigma T^4 \tag{1.4}$$

Equation 1.4 is half of the liberated gravitational potential energy that can be observed. Accounting for viscous energy dissipation, equation 1.4 can yield a temperature profile as a function of disc radius in equation 1.5.

$$T\left(R\right) = \left[\frac{3GM\dot{M}}{8\pi\sigma R^3}\left[1 - \left(\frac{R_{ISCO}}{R}\right)^{\frac{1}{2}}\right]\right]^{\frac{1}{4}} \tag{1.5}$$

The $\left[1 - \left(\frac{r_{ISCO}}{r}\right)^{\frac{1}{2}}\right]$ term ensures a hard cut-off at the innermost stable circular orbit (ISCO), a general relativistic limit in which a test particle can stably orbit a massive object (Misner et al., 2017). AGN emission can be separated into 'continuum' and 'line' emissions. The former is thought to be emission from the accretion disc of matter in-falling around the SMBH (Peterson, 2001; Rashed et al., 2015). Growing evidence suggests that strong x-ray emissions from the innermost regions of the AGN are reprocessed by surrounding gas into the UV/optical dominated accretion disc continuum. Continuum emission then drives reprocessing in

AGN structures outside the accretion disc to produce AGN emission lines (Jha et al., 2022; Cackett et al., 2007). Observed emission is, therefore, a combination of continuum and line emissions. There are also gaps in observed spectra due to neutral hydrogen absorption in the extreme ultraviolet (UV, 10^6 Hz) and in the infrared to radio due to Earth's atmospheric absorption (Peterson, 1997). Broad emission lines ($500\,\mathrm{Km\,s^{-1}} \Delta\nu_{FWHM} 10^4\,\mathrm{Km\,s^{-1}}$ (Peterson, 1997)) are present in the spectra of several types of AGN and can be explained well by the BLR (figure 1.1). They are driven by photoionisation at UV energies of the BLR gas clouds by the continuum emission, thought to originate from the accretion disc with the line widths explained by Doppler broadening. Similarly, narrow lines are explained by the low-density, ionised (by the continuum) gas in the NLR. Additionally, the presence of emission line obscuration and a broad infrared (IR) emission can be explained by the presence of an axisymmetric dusty torus reprocessing UV/optical seed photons. Thus, we see that features in the observed spectra of AGN are linked to their structures and this allows us to infer this structure by analysing the observed emission. These ideas form the basis of this report as it outlines the application of stochastic modelling and statistical techniques to infer the scale of component structures within AGN. Heuristically, variability time scales of emission spectra indicate a rough size for the varying source. For a source to vary coherently, it must be causally connected based on light-travel time. It is from this that we can infer that the scale of the continuum generating accretion disc must be on the order of light-days (Peterson, 2001) and the BLR to be light-months to years.

Several monitoring campaigns have found that UV and optical continua are closely coupled. This sets us up to understand the theory behind reverberation mapping, which is a tool that uses time-domain analysis to infer size scales based on light-travel time. The model discussed thus far however has several limitations as the interior structures of AGN are still poorly understood. Notably, observational evidence differs from the predicted sizes of the accretion disc and the BLR some-

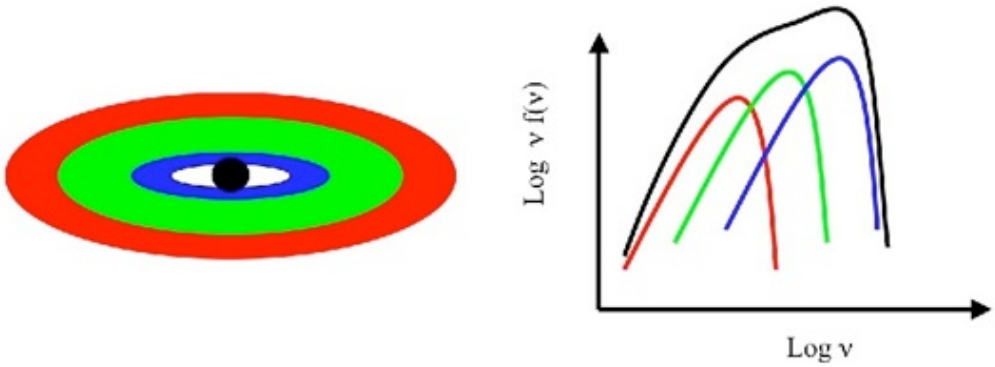

Figure 1.2: Idealised accretion disc spectrum (solid black line) showing blackbody contributions from accretion disc annuli (multicoloured lines) (Jeanette Gladstone).

times by a few orders of magnitude (Peterson, 2001; Jha et al., 2022). This will be elaborated on further in the research questions sections and the discussion of the results.

Several accretion disc models have been proposed, namely the Shakura-Sunyaev (thin disc) model, which results in a decreasing temperature profile. Higher temperatures exist near the inner regions which decrease with increasing disc radius. For SMBHs, the accretion disc emission peaks in UV/optical wavelengths which then drives reprocessing in the BLR and the dusty torus. The origin of the UV/optical variability is thought to be due to the reprocessing of X-ray emission (McHardy et al., 2016) from the innermost regions of AGN. Whereas the UV/Optical continuum is due to the accretion process itself. With the variability of the disc being driven by a central source, then light travel-time across the disc radius implies delays in responses at different wavelengths (Mudd et al., 2018). The thin disc model suggests each annulus of the accretion disc behaves as a blackbody emission (described by the Planck function, $B_\nu(\lambda, T)$) with a characteristic emission wavelength λ and, therefore, an effective temperature, T in equation 1.6 (Jha et al., 2022), ignoring the cut-off at R_{ISCO}.

$$T(R_{Disc}) = \left(\frac{3GM_{SMBH}\dot{M}}{8\pi\sigma(R_{Disc})^3}\right)^{\frac{1}{4}} \; for\, R_{Disc} >> R_{ISCO}, \tag{1.6}$$

where G, M_{SMBH}, $\dot{M}$ represent the gravitational constant, supermassive black hole mass, and the mass accretion rate. σ and R_{Disc} are the Stefan-Boltzmann constant and accretion disc radius respectively. The total flux-spectrum is the contribution of flux from each disc annulus which can be described by equation 1.7.

$$F_\nu = \int_{R_{inner}}^{R_{outer}} B_\nu(\lambda, T)\, d\Omega = \int_{R_{inner}}^{R_{outer}} \frac{2hc \cdot 2\pi R\, cos(i)}{\lambda^3 \cdot (e^{\frac{hc}{\lambda k_B T}} - 1) \cdot D^2}\, dR, \tag{1.7}$$

where R_{inner} and R_{outer} are the inner and outer limits of the accretion disc respectively and $d\Omega$ represents the solid angle with respect to an observer, depending on the disc inclination angle i and distance D. The accretion disc radius as a function of emission wavelengths can then be stated in equation 1.8 and an idealised depiction in figure 1.2.

$$R_\lambda = R_{\lambda_0} \left[\left(\frac{\lambda}{\lambda_0} \right)^\beta \right], \tag{1.8}$$

where the radii in equations 1.5 and 1.8 are connected by Wien's displacement law, $\lambda_{Peak} = \frac{b}{T}$ ($b \approx 2898\,\mu\text{m} \cdot \text{K}$ is Wien's displacement constant) which states that the peak of a black body spectra is inversely proportional to the absolute temperature of the black body. R_{λ_0} can be thought of the disc radius at a reference wavelength, λ_0 Jha et al. (2022) and $\beta = \frac{4}{3}$ assuming a thin disc model. Hence, equation 1.6 predicts that $R_{DISC} \propto \lambda^\beta$ with $\beta = \frac{4}{3}$. Shakura and Sunyaev (1973) argues that there will be a significant contribution to the opacity in the inner regions of the disc due to inelastic Compton scattering of high-frequency photons off electrons and hence modifying the thermal spectrum to a Wien distribution rather than a Planck distribution. However, this $R_{Disc} >> R_{ISCO}$ approximation justifies the use of the Planck function in equation 1.7 as the UV and optical emitting regions of the disc are not expected to be near the innermost-stable circular orbit. This allows us to test different disc models by fitting this power law for RM time lags

from accretion discs as in equation 1.9.

$$\tau = \frac{R_{\lambda_0}}{c}\left[\left(\frac{\lambda}{\lambda_0}\right)^{\beta} - 1\right]. \tag{1.9}$$

However, due to each annuli of the accretion disc emitting as a black body and not a single temperature each observed wavelength corresponds to multiple annuli. This requires accounting for flux-weighting of a superposition of multiple black body spectra and results in the introduction of a corrective factor for the reference wavelength which accounts for the flux contributions from different annuli (see Mudd et al. (2018); Fausnaugh (2017) for a full derivation). This correction is typically on the order of unity. Generally, spectral energy distributions (SEDs) of accretion discs can be characterised by a power law shape $F_\nu \propto \nu^{-\alpha}$. The emission from the accretion disc is thought to comprise the continuum component of the overall AGN SED. Under the thin disc assumptions of equation 1.5, $\alpha = \frac{1}{3}$. Depending on the type of disc, α is typically between 0 and 1. The power law shape is a reasonable description of AGN SEDs, however, when looking over several decades of frequency, we see many finer details such as broad depressions and bumps that provide clues to the origin of the emission (fig. 1.3). These various continuum components are dominated by different physical processes. The blue line in fig. 1.3 is known as the 'big blue bump' due to the significant amount of energy emitted as a strong, broad feature that dominates between 4000Å to 1000Å. This is thought to be produced by the accretion disc and defines the characteristic $F_\nu \propto \nu^{\frac{1}{3}}$. SED local minimum in the vicinity of 10^4Å. This is thought to represent the hot thermal spectrum (big blue bump) and a cool thermal spectrum at wavelengths greater than 10^4Å produced from warm ($T > 2000\,\mathrm{K}$) dust grains, known as the IR bump.

Accretion disc models are currently mainly characterised by their behaviour at different accretion rate flows or Eddington ratios and the angular momentum at the

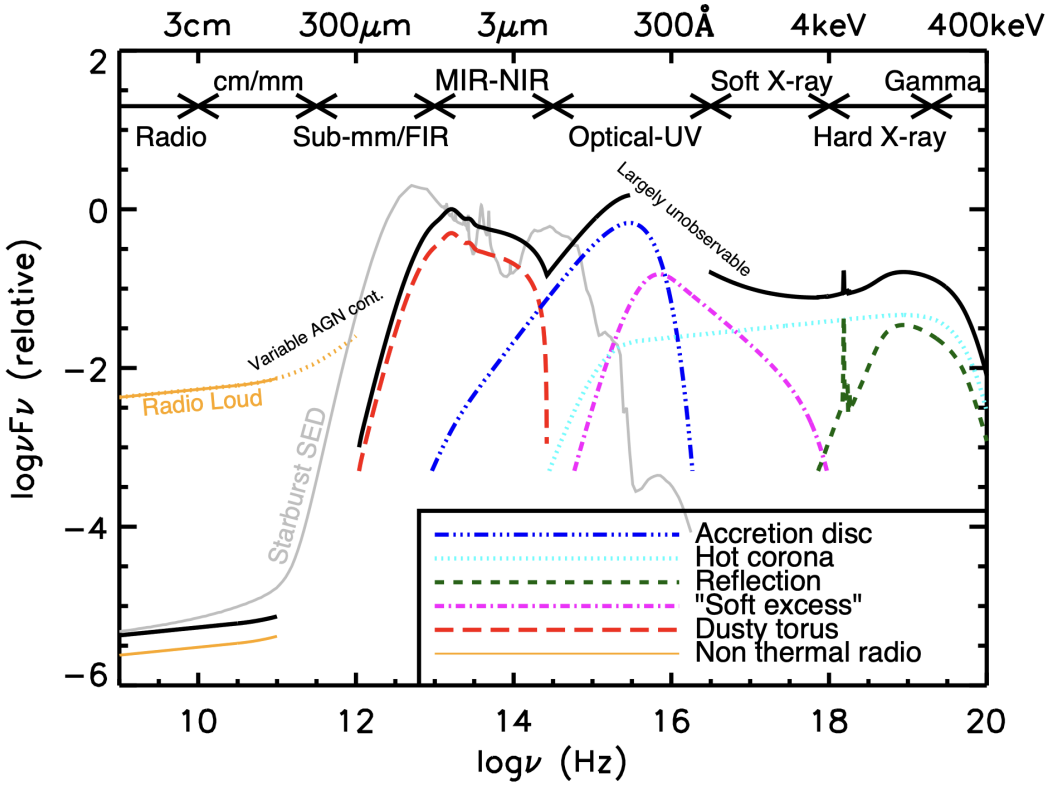

Figure 1.3: AGN SED taken from Harrison (2014) with the solid black curve representing the total SED and the coloured lines representing the individual components. The large gap in optical-UV frequencies is unobservable due to the interstellar medium made up of neutral hydrogen.

outer disc (Czerny, 2019). Bondi or spherically symmetric accretion has negligible angular momentum and is typical in very weakly active galaxies or dynamical stellar collapse. For Eddington ratios $\dot{m} \sim 0.01$ and the angular momentum a fraction of the Keplerian angular momentum, the flow is advection-dominated and is typical of low luminosity AGN. For higher accretion rates, the accretion matter can cool effectively due to the higher densities so the flow becomes optically thick emitting locally as a black body and the angular momentum is locally Keplerian. The emission is described well by a thin disc. When the accretion rate is super-Eddington (i.e. $\dot{m} \geq 1$), the accretion efficiency is lower than for a standard thin disc despite R_{ISCO} moving inwards. The local emission is no longer just the thermal dissipation from a black body because a non-trivial fraction of energy is 'lost' into the SMBH event horizon. Such a disc is known as a slim disc as the disc thickness is

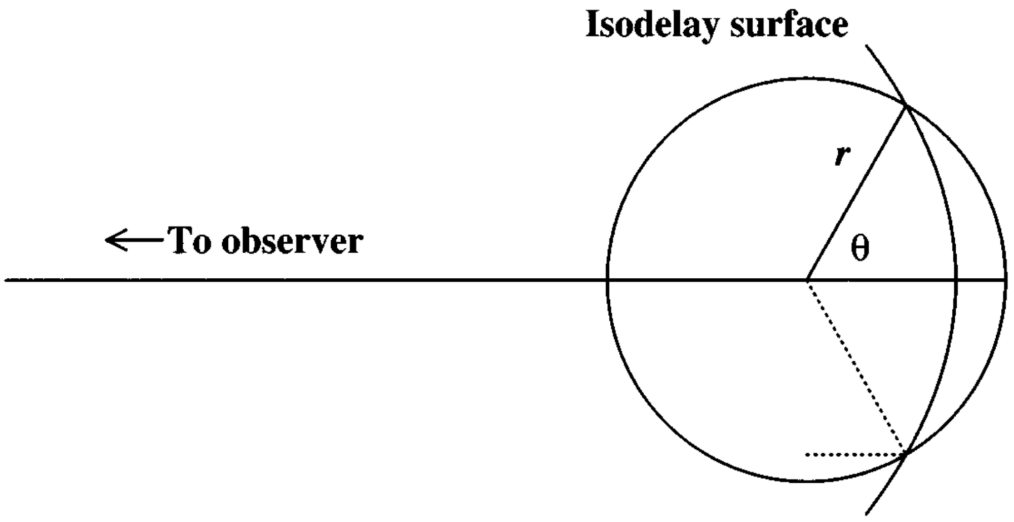

Figure 1.4: Idealised model of a reverberating structure located at a radius r from the centrally emitting ionising source. Source photons (dotted line) travelling radially outward reach the reverberating structure and are instantaneously reprocessed some of which are emitted in the observer's direction. Therefore, the reprocessed photons lag the source photons by some time τ that depends only on the difference in light path length.

no longer negligible relative to the disc radius. At sub-Eddington accretion rates, the slim accretion disc SED converges to that of a standard thin disc but typically the power law is redder than that of a thin disc, $F_\nu \propto \lambda$ (Donnan et al., 2023).

1.2 Reverberation Mapping

1.2.1 Overview of Reverberation Mapping

The basis of reverberation mapping (RM) is the greater light-travel time from source to reprocessing object to observer compared to the direct path from source to observer. As suggested previously, the time delays associated with the difference in light paths provide indirect information on the size and structure of AGN. In practice, RM involves measuring time delays between flux variations (flux against time, known as a light curve) of an ionising source and the flux variations of an irradiated region (Cackett et al., 2021) as changes in the irradiating flux drive

changes in the reprocessed emission. These time delays are identified as time lags, τ (figure 1.4), of a light curve of a photometric passband corresponding to a line emission from a light curve corresponding to a smooth, continuous part of the spectrum or spectral energy distribution (SED). For a given time delay, τ, after the continuum emission, an observer will receive the reprocessed photons from an isodelay surface or surface of constant time delay characterised by a radius, r, the distance from the continuum source. Then the reprocessed response is given by the intersection of the isodelay surface and the reverberating region at radius r (Peterson, 1997).

$$\tau = \frac{(1 + cos\theta)r}{c} \tag{1.10}$$

The intersection of these surfaces forms rings with radius $rsin\theta$ and surface area $2\pi r^2 sin\theta d\theta$ such that:

$$\psi(\theta)d\theta = 2\pi\zeta r^2 sin\theta d\theta, \tag{1.11}$$

Where ζ is a constant representing the responsivity of the reverberating region per unit area. The emission line response can then be converted to a function of τ, $\psi(\tau)d\tau = \psi(\theta)\left|\frac{d\theta}{d\tau}\right| d\tau = 2\pi\zeta rcd\tau$. In reality, the time lag τ will depend on the geometry of the accretion disc, reprocessing region, and the angle of observation. However, the mean lag will be;

$$\langle\tau\rangle = \frac{R}{c}, \tag{1.12}$$

where R is the typical size of the reprocessing region (Cackett et al., 2021). The angular resolution provided by RM is of the order of micro-arcseconds (1 light-day across at 100 Mpc is $\sim$ 2 micro-arcsecond) (Cackett et al., 2007) which provides unparalleled insights into otherwise unreachable regions. This report outlines the

use of RM to estimate information about the structure of AGN accretion discs, BLRs, and dusty tori.

RM makes two key assumptions (Peterson, 2001; Fausnaugh, 2017):

1. The continuum originates in a single central point source.
2. Light-travel time is the most important time scale and the reverberating medium responds instantaneously to continuum variations.

Then, assuming that the lagged reprocessed light curve $F_L(t)$ responds linearly to the continuum light curve $F_C(t)$ the relationship between the two can be represented as a convolution operation:

$$F_L(t) = \int \psi(\tau) F_C(t - \tau)\, d\tau, \tag{1.13}$$

where τ is the time lag, and $\psi(\tau)$ is the transfer function. The transfer function is determined by the matter distribution around the continuum, and it controls the response of the reprocessed light curve to a Dirac delta function continuum outburst (Fausnaugh, 2017; Thorne, 2022); in effect, it blurs the reprocessed light curve F_L and represents the unknown physical conditions present in the reverberating region. The goal of RM is to determine the geometry and kinematics of the reverberating region, encapsulated by $\psi(\tau)$, given F_C and F_L (Collier, 1999; Fausnaugh, 2017). The first moment of $\psi(\tau)$ defines a mean lag, $\langle\tau\rangle$, between the continuum and emission light curves and gives a characteristic size scale, $R = c\,\langle\tau\rangle$, for the reverberating region (Collier, 1999). Several methods exist to measure $\langle\tau\rangle$ from observed continuum and lagged light curves. This report will outline briefly three such methods implemented and compare their estimated lag accuracy.

1.2.2 Javelin

Javelin's methodology rests upon the idea that the accuracy of time lags can be enhanced if the continuum behaviour between the observed continuum and emission

is modelled. Kelly et al. (2009) and further work since then have found that AGN variability can be well described by a damped random walk model (DRW) (Kelly et al., 2009). This model is able to statistically predict the value of the light curve at an unmeasured time from the statistical properties of irregular samples (Zu et al., 2011). This is encapsulated by χ^2 statistics, the relationship between two random and mutually exclusive variables. More specifically, Javelin's formalism states that the continuum and emission lines are described by a Gaussian process (Rybicki and Kleyna, 1994) and the relationship between continuum and emission lines at different times can be described by an exponential auto-correlation function:

$$\langle F_C(t_i)F_C(t_j)\rangle = \sigma^2 e^{\frac{-|t_i-t_j|}{\tau_d}}. \tag{1.14}$$

Where $\sigma^2 = \frac{\hat{\sigma}^2\tau_d}{2}$. Physically, σ^2 corresponds to the amplitude of a damped random walk and τ_d the damping timescale otherwise known as the characteristic decorrelation timescale. The linear relationship between the driver and lagged light curves (equation 1.13) is assumed by Javelin to be a simple top-hat transfer function with width w and amplitude A. Other relevant covariances; $\langle F_C(t_i)F_C(t_j)\rangle$, $\langle F_L(t_i)F_L(t_j)\rangle$, and $\langle F_L(t_i)F_C(t_j)\rangle$ can be calculated by substituting for equation 1.13 and they describe elements of an autocorrelation matrix $\mathbf{F} = \left\langle \vec{F}\vec{F} \right\rangle$ as can be seen in equation 1.15.

$$\mathbf{F} = \begin{pmatrix} \langle F_C(t_i)F_C(t_j)\rangle & \langle F_C(t_i)F_L(t_j)\rangle \\ \langle F_L(t_i)F_C(t_j)\rangle & \langle F_L(t_i)F_L(t_j)\rangle \end{pmatrix} \tag{1.15}$$

A more detailed explanation of the choice of an exponential covariance matrix is described in Kelly et al. (2009); MacLeod et al. (2010). The formalism described by equation 1.15 can be straightforwardly extended to multiple reprocessed or 'line' light curves. Furthermore, adding uncorrelated noise (also Gaussian) can be described as terms on the leading diagonal. The assumption that the driving process is Gaussian then implies that a particular realisation of $\vec{F}$ is given by a generalised χ^2 distribution.

$$P(\overrightarrow{F}) \propto \sqrt{|\mathbf{F}|} e^{\left(-\frac{\overrightarrow{F}^T \mathbf{F}^{-1} \overrightarrow{F}}{2}\right)}. \tag{1.16}$$

Observed realisation of the light curve can then be described by the addition of a noise term $\overrightarrow{y} = \overrightarrow{F} + \overrightarrow{n} + \mathbf{L}\overrightarrow{q}$. With a probability distribution;

$$P(\overrightarrow{n}) \propto \sqrt{|\mathbf{n}|} e^{\left(-\frac{\overrightarrow{n}^T \mathbf{n}^{-1} \overrightarrow{n}}{2}\right)}, \tag{1.17}$$

where $\mathbf{n}$ is $\langle \overrightarrow{n}\, \overrightarrow{n} \rangle$, the noise covariance matrix. For n data points across n_l light curves, the response matrix $\mathbf{L}$ and linear coefficients $\overrightarrow{q}$ are a $n_l \times n$ matrix and a $n_l \times 1$ vector respectively. $\mathbf{L}$ and $\overrightarrow{q}$ are introduced to remove the mean fluxes from light curves for removing linear trends, de-trending, to filter out variability components that may originate from irrelevant processes for example from contamination from the host galaxy (a good example of this procedure is outlined by Hernández Santisteban et al. (2020)). This enables a likelihood function $\mathcal{L}$ to be defined ($P(\overrightarrow{y}|\overrightarrow{p})$, where $\overrightarrow{p}$ are the model parameters that describe the process in equation 1.19 i.e. the transfer function). $\mathcal{L}$ is to be maximised. First, Javelin fits τ_d and $\hat{\sigma}$ for the driver light curve by using Log-Gaussian priors for both centred around the flux median and standard deviation. This gives an idea of how much the driving light curve should vary relative to observed epochs. Javelin then uses this DRW model of the driving light curve to interpolate the lagged light curves before shifting, scaling and smoothing the driving light curve for comparison with the lagged light curves. Optimum fit parameters τ_i, w_i, and A_i for each light curve i can then be extracted. The optimum fit parameters for both the driver and the lagged light curves are sampled using 'emcee', an MCMC sampler developed by Foreman-Mackey et al. in 2012. Javelin is open-source software accessible at `https://github.com/nye17/javelin`.

1.2.3 PyROA

PyROA's methodology interpolates irregularly sampled light curve data as running optimal averages (ROAs), turning the data into smooth differentiable light curves. A ROA is technically an inverse-variance weighted average that minimises the resultant weighted average's variance and is helpful in producing realistic light curve interpolations. For a given time t along a light curve, the inverse-variance weighted average is evaluated with the diminishing influence of data points further away from t. The window function, w_i controls this and is by default a Gaussian. Each light curve, $X(t)$ (equation 1.15 (Donnan et al., 2021)), is interpolated from N data points, D_i each with an error σ_i. Where subscript i is an index over data.

$$X(t) = \frac{\sum_{i=1}^{N} D_i w_i(t)}{\sum_{i=1}^{N} w_i(t)}. \tag{1.18}$$

The value at any time value can then be calculated by the window function (equation 1.18) that calculates a weighted averaging over all N. Flexibility in a ROA is determined by the Δ parameter as it controls the number of effective parameters used to fit the light curve. A small Δ follows small light curve variations closely whereas a large Δ is stiffer. In the infinite limit of Δ the ROA becomes a rigid constant averaging evenly across all the data with one effective parameter. The ROA at $\Delta = 0$ has N effective parameters and fits the data perfectly.

$$w_i(t) = \frac{1}{\sigma_i^2} e^{-\frac{1}{2}\left(\frac{t-t_i}{\Delta}\right)^2}. \tag{1.19}$$

Optimising the value of Δ is important to balance between an overly flexible model (too small a Δ) and an overly stiff model (too large a Δ) or Occam's bias. To do so, PyROA quantifies the number of effective parameters $P_i(\Delta)$ (equation 1.19).

$$P_i(\Delta) = \frac{\partial X(t_i)}{\partial D_i} = \frac{w_i(t_i)}{\sum_k w_k(t_i)} = \frac{\sigma_i^{-2}}{\sum_k \sigma_i^{-2} e^{-\frac{1}{2}\left(\frac{t-t_i}{\Delta}\right)^2}}. \tag{1.20}$$

Then the optimal value for Δ is calculated using the Bayesian Inference Criterion (BIC), which is a 'badness of fit' statistic that penalties models with too many effective parameters. Light curves at different photometric wavelengths are simply assumed to be scaled and shifted versions of the continuum. This assumes that the shape of the variability by $X(t)$ is the same for each light curve (equation 1.20). This model allows for an extra variance term, s_i, to be added Further details can be found in Donnan et al. (2021).

$$f_i(t) = A_i X(t - \tau_i) + B_i. \tag{1.21}$$

A_i is the root-mean square flux, B_i is the mean flux, and $X(t)$ is the driving continuum light curve so that τ_i is measured relative to this light curve. PyROA fits this model using a Bayesian approach. The posterior probability (probability of model given data is maximised by the best-fitting parameters) can be linked to the log-likelihood (probability of the data given a model) and the BIC to find the best-fit parameters for $\{A_i, B_i, \tau_i,\ s_i\}$ by repeated MCMC sampling using 'emcee'. PyROA takes uniform distributions as priors for the parameters in equation 1.21 as range estimates. Then each light curve is scaled and shifted back in time according to $\{A_i, B_i, \tau_i,\ s_i\}$. s_i parameters are also added in quadrature to the flux errors. The stacked light curves are then treated as a single light curve where the ROA, $X(t)$ is calculated. Calculation of the number of effective parameters and the BIC can then inform successive samples of the Markov chain. PyROA is open-source software and accessible at `https://github.com/FergusDonnan/PyROA`.

1.2.4 Sour

Cross-correlation functions (CCFs) were first implemented in a reverberation mapping analysis by Gaskell and Peterson (1987) to estimate the sizes of emission line regions in quasars. This investigation used the sour code which is a recent CCF implementation developed by Edelson et al. (2017). CCFs of time series are defined as

in equation 1.22, where the $\star$ denotes the cross-correlation operation and $*$ denotes a complex conjugate. The CCF is entirely a function of the time-value difference or lag τ, and it will produce a peak (although not necessarily symmetric) for a τ value that maximises the similarity between the time series $f(t)$ and $g(t)$.

$$(f \star g)(\tau) = \int_{-\infty}^{+\infty} f^*(t) g(t+\tau) dt \tag{1.22}$$

Real light curves are unevenly sampled and Sour linearly interpolates along the time series before calculating the CCF. This is known as the interpolated cross-correlation method or ICCF method. Real data are also discrete and finite such that equation 1.22 becomes equation 1.23. Given two discrete time series, f_1 with times t_1 and f_2 with times t_2, the CCF is calculated by linearly interpolating f_2. For a lag τ, f_2 is estimated at every $t_1 + \tau$ by interpolating between the two nearest points of f_2. Then the CCF can be calculated after pairing the interpolated f_2 data with f_1 (Gaskell and Sparke, 1986).

$$(f \star g)(\tau) = \sum_{m=0}^{N-1} \overline{f^*(m)} g(|m+\tau|) \tag{1.23}$$

ICCF peaks are generally not symmetric; thus, to ensure the error interpretability of the ICCF peak, the interpolation and CCF calculation are done twice, with an interpolation on both of the time series. The CCF results from the two light curves are then averaged to produce a final value. This ensures consistency with the definition in equation 1.22 as it is a symmetric function. Typically a centroid estimate of the ICCF's peak is used as the time lag measurement between two light curves. The error estimates from ICCFs can be greatly enhanced by accounting for the variance in the time lags. The FR/RSS (flux randomisation/ random subset selection) method by Peterson et al. (1998) was developed to address this problem and Sour also integrates this into its analysis. FR/RSS provides model-independent time lag uncertainties. This is a Monte Carlo technique that builds up

a time lag distribution from multiple realisations of a CCF for a given pair of light curves. In each realisation, Gaussian noise is added onto each flux measurement depending on the flux error, assuming they are normally distributed. Additionally, for a light curve consisting of N points, the FR/RSS method picks a subset of points with replacement to create a new time series. The data points that were selected more than once had their error bars decreased by a factor of $R^{-\frac{1}{2}}$, where R is the number of times a data point is selected. $\left(1-\frac{1}{N}\right)$ is the probability that a data point is not selected in a given realisation so that $\left(1-\frac{1}{N}\right)^N \rightarrow \frac{1}{e}$ is the fraction of the data set not selected in a given realisation. This is because each data point has the same independent probability of not being selected. The CCF is then measured and the weighted mean of all the points above 80% of the highest CCF power value. Sour is open-source software and accessible at `https://github.com/SimonVaughanDataAndCode/sour`.

Chapter 2

Comprehensive Comparison of Reverberation Mapping Algorithms

This chapter provides a comprehensive comparison of Javelin (Zu et al., 2011), PyROA (Donnan et al., 2021), and traditional methods obtained by cross-correlation through Sour (Edelson et al., 2017). This comparison will be based on two RM campaigns of NGC 5548, Koshida et al. 2014 (Koshida et al., 2014) and Edelson et al. 2019 (Edelson et al., 2019). The former was published in 2014 and is of the dusty torus region and the latter published in 2019 is of the accretion disc. NGC 5548 is a type 1 Seyfert AGN and was one of the original listed by Carl Keenan Seyfert that showed broad emission lines. Comparing different algorithms informs the reliability of the results and therefore facilitates their physical interpretations and the robustness of the theory behind AGN structure and their emission. Developing optimal analysis strategies for datasets which vary in structure and observational parameters is another motivation for comparing multiple algorithms on the same datasets, this is especially beneficial given the different methodologies behind the algorithms being compared in this report.

2.1 Overview of Preliminary Datasets

2.1.1 Dusty torus

Many observations of AGN imply the existence of a thick dusty torus surrounding the SMBH and accretion disc, sometimes obscuring the disc emission from an observed line of sight. The near-infrared (NIR) continuum emission of AGN is considered to be dominated by the thermal re-emission from host dust (2000 K) driven by the thermal reprocessing of the UV-optical disc continuum (Landt et al., 2011). RM campaigns have sought to resolve the dusty torus by measuring time lags between the UV-optical continuum and NIR emission from the innermost part of the torus. The data set used in this investigation is from Koshida et al. (2014) for the type 1 AGN NGC 5548.

Data for NGC 5548 are from the V (optical continuum) and K (reprocessed thermal emission) photometric bands of the multicolor imaging photometer (MIP) on the MAGNUM telescope (Kobayashi et al., 1998). MIP has a field-of-view of $1.5 \times 1.5\,\mathrm{arcmin}^2$ and it simultaneously obtains images in the V and K bands by splitting the incident the incident into two different detectors. One is SITe CCD 1024×1024 pixels with $0.277\,\mathrm{arcsec\,pixel}^{-1}$ and the other is an SBRC InSb array of 256×256 pixels at $0.346\,\mathrm{arcsec\,pixel}^{-1}$. The V band at 544 nm avoids contamination from BELs from BLR reprocessing that are also variable and may make finding a variability timescale of the torus harder to measure. The K band at $2.19\,\mu$m is chosen as it is where the reprocessed dust emission dominates over the power-law disc continuum. For details on the data reduction procedures please refer to Koshida et al. (2014).

The photometric fluxes initially contained significant contributions from the host-galaxy starlight and were consequently subtracted by using Sakata et al. (2010)'s estimate of the host-galaxy flux in the V band. Sakata et al. (2010) estimated the host-galaxy flux by surface brightness fitting to corresponding high-resolution

HST and MAGNUM images. For the K band, the host-galaxy flux estimate was obtained from Suganuma et al. (2006). The host-galaxies are compiled in table 5 of Koshida et al. (2014). Additionally, two strong NELs, $[OIII]$ at $\lambda = 4959$Å and $\lambda = 5007$Å contaminate the V band were subtracted using the values obtained from Sakata et al. (2010). For more details, please refer to Koshida et al. (2014); Sakata et al. (2010).

2.1.2 Accretion disc

Accretion discs power AGN emission and studying their size and structure enables an enhanced understanding of SMBH accretion. An optically thick and geometrically thin viscous disc was first proposed by Shakura and Sunyaev (1973) to explain AGN continuum emission and Frank et al. (2002) proposed that magnetic re-connection in a corona above the disc can heat the outer disc leading to the 'lamp-post/reprocessing' model. The data set that was used to investigate these disc models was obtained from the UV/optical photometric light curves of (Edelson et al., 2019) taken by the Swift space telescope. Comparing UV/optical light curves enables a study of the accretion disc itself and from time lags the size and structure of the accretion disc can be inferred. The campaign by Edelson et al. (2019) is one of the first intensive-disc reverberation mapping campaigns (IDRMs), increasing the typical 100 samples obtained to executing $200 - 350$ samples by monitoring all UV/optical bands simultaneously and intensive blanketing. IDRMs can more accurately resolve shorter timescales of a few days expected from accretion discs.

This investigation uses the UV/optical Swift light curves ($W2$ (1928 Å), $M2$ (2246 Å), $W1$ (2600 Å), U (3465 Å), B (4392 Å), V (5468 Å)) for NGC 5548. For details on the Swift telescope's photometry calibration please refer to Poole et al. (2008); Breeveld et al. (2011). Swift's UV/optical photometry (UVOT) has a field of view of 17×17 arcmin with a CCD with 2048×2048 pixels and $0.502\,\mathrm{arcsec\,pixel^{-1}}$. For details on the UVOT data reduction for NGC 5548 please refer to Edelson et al. (2015). NGC 5548 was an optimal source because it shows strong variability in

the UV/optical bands and it is also apparent that the light curves are similar, thus making them ideal for an IDRM campaign to measure variability time scales on a few days.

2.2 Analysis and Results

The dusty torus region of NGC 5548 is expected to be ~ 60 Kishimoto et al. (2011) light-days. Furthermore, Koshida et al. (2014)'s weighted average dust reverberation lag is 60.9 ± 0.3 days. These data were obtained with a median monitoring interval of 3.0 days, excluding observational gaps due to solar conjunction and facility maintenance Koshida et al. (2014). Secondly, NGC 5548's accretion disc is 1 light day and Edelson et al. (2019) estimates the W2-V lag of 1.27 days. Table 2.1 summarises the lags obtained from Javelin, PyROA, and Sour with data from 6 observational epochs (Koshida et al., 2014). Table 2.1 also presents the weighted averages of all the epochs. These cross over any dust reformation processes that are estimated to be $5-6$ months (Landt et al., 2019). We observe good agreement between the three algorithms and the estimates provided in Koshida et al. (2014).

Figures 2.1 and 2.2 display the fits from Javelin and PyROA algorithms to the sparsely sampled light curves over the whole observing period (51992.5 to 54332.3) without considering the observational gaps. This was conducted to compare the behaviour of both algorithms during gaps between observing epochs. Qualitatively, the Javelin fit is more constrained than PyROA's within the gaps and can be attributed to the DRW model. PyROA's fit becomes unconstrained with a Gaussian transfer function however, Donnan et al. (2021) suggests using a Lorentzian transfer function for more constrained fits, as this was preliminary testing that function was not utilised here. Javelin, however, when presented with the same observational gaps has a constrained error overlay. Javelin's underlying DRW model and PyROA's lack of a model for the light curve shape can explain the difference in the error overlay. PyROA's unrealistic fitting in the presence of sampling gaps was

confirmed by using mock data from Donnan et al. (2021) and artificially creating gaps. This reproduced the discontinuities and unrealistic error overlays seen in figure 2.2. Despite PyROA's poor fitting, the time lags remained robust and are in good agreement with Javelin, PyROA and Koshida et al. (2014).

Aliasing of peaks within the lag distributions was especially a problem during Javelin's preliminary testing. Convergence to aliased lags was eliminated by constraining Javelin's MCMC search limits for the lag parameters. This was informed by identifying aliasing with pairs of peaks symmetric around $\tau = 0$. Constraining the lag prior was conducted individually for each observational epoch. Aliasing effects were strongest in the presence of observational gaps as Javelin mistakenly shifts the V-band continuum to match K-band emission by the gap period (Zu et al., 2011) because it minimises the data overlap. In contrast, PyROA does not exhibit aliasing features and the convergence is robust against changes in the lag search limits, albeit the convergence time is highly sensitive to the search limits. PyROA allows for initial estimates of time lags to help reduce the convergence time, however, convergence time is highly dependent on the priors and the lag limits being searched. The initial time-lag estimate parameter used for all observational epochs was set at 70 days which is the lag obtained from Landt et al. (2019).

These data were also compared with Sour (Edelson et al., 2017), an R package that uses an interpolated cross-correlation function that extracts time lags. To calculate errors, Sour used the 'flux randomisation and random subset selection' method outlined in Peterson et al. (1998). Aliasing due to sampling gaps was also an issue with Sour and the lag limit had to be finely constrained for every observing epoch. Lags were calculated from the centroid (full-width at half-maximum) width to reduce the likelihood of unrealistic lag estimates from the position of the peak. An example is shown in figure 2.3. Once again, aliases were identified using symmetric peaks about $\tau = 0$.

The relevant wavelength bands for the accretion disc RM campaign from Edelson

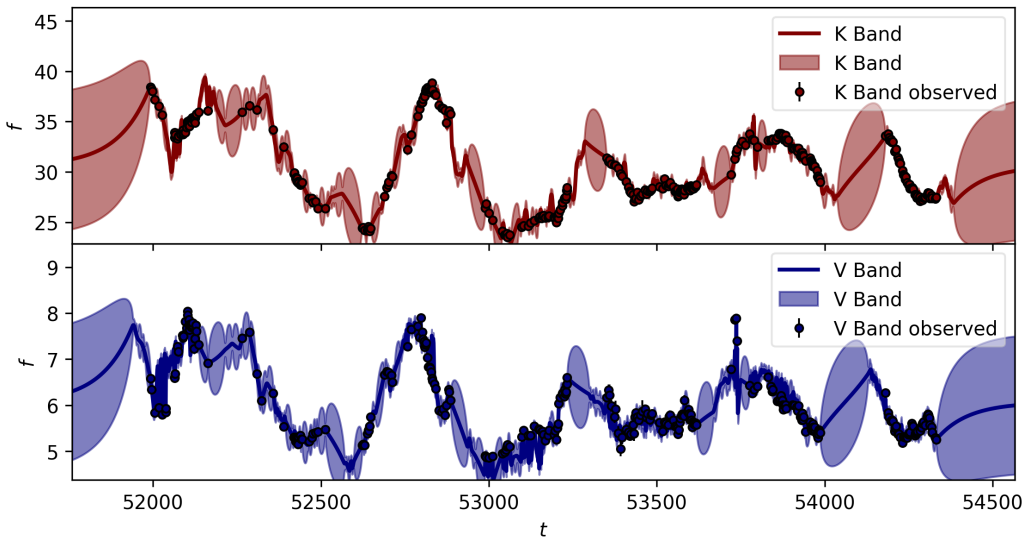

Figure 2.1: Javelin's fit of Koshida et al. (2014) from MJD 51992.5 – 54332.3 inclusive of the seasonal gaps due to different observing epochs. This was conducted with default parameters for burn-in steps, number of chains, and the number of walkers at 100. Flux and time units are in mJ and days respectively.

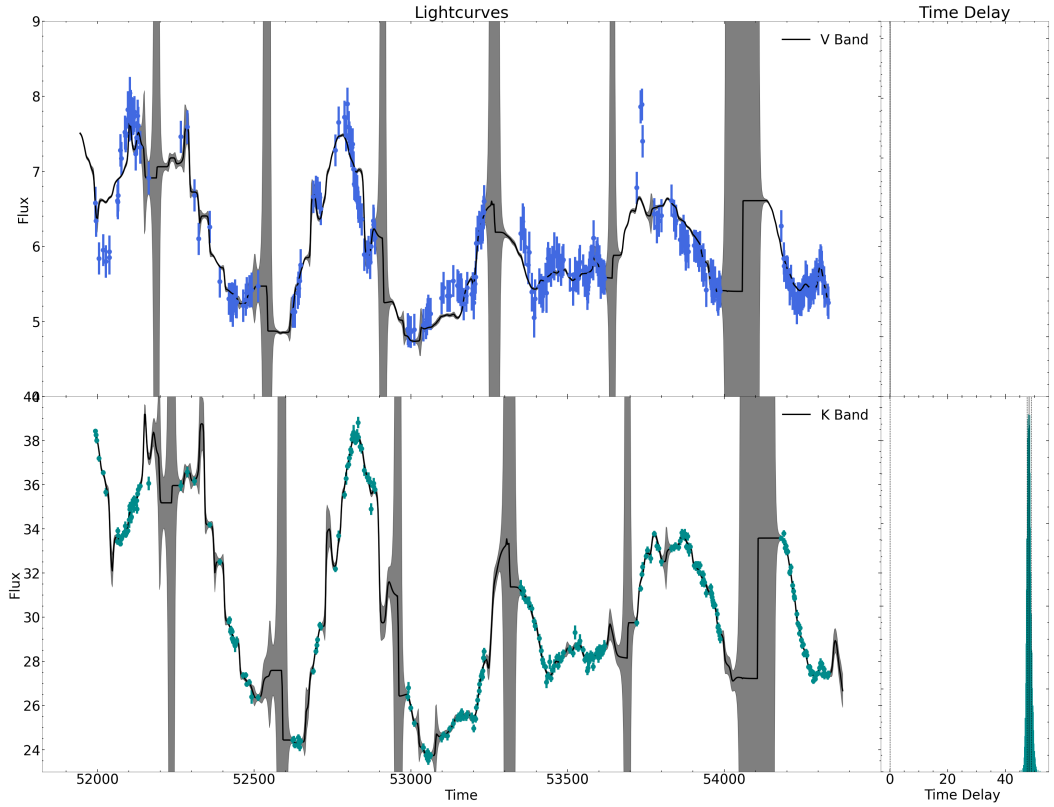

Figure 2.2: PyROA's fit of Koshida et al. (2014) from MJD 51992.5 – 54332.3 inclusive of the seasonal gaps due to different observing epochs. The degree of blurring, Δ, was set at the default $0.01 \leq \Delta \leq 10$.

Table 2.1: Summary of NGC 5548 time-lags between the V and K bands with data obtained from Koshida et al. (2014). Lag units are in days from MJD 51992.5 – 54332.3 inclusive of the seasonal gaps due to different observing epochs. The uncertainties are the minimum (lower) and maximum (upper) values on the lags. Analysis was conducted on all 6 observational campaigns with weighted averages provided in bold. Javelin and PyROA estimates should be compared with the Sour estimates which use a traditional cross-correlation method (Gaskell and Sparke, 1986).

MJD	Javelin Lag	PyROA Lag	Sour Lag
Weighted Average	$\mathbf{60.5^{63.5}_{57.8}}$	$\mathbf{62.9^{64.6}_{61.0}}$	$\mathbf{54.3^{57.9}_{50.5}}$
51992.5 - 52389.5	$61.9^{63.6}_{56.7}$	$57.6^{58.1}_{57.2}$	$47.4^{50.8}_{44.7}$
52308.6 - 52797.4	$53.7^{55.4}_{52.1}$	$49.1^{50.0}_{47.1}$	$54.0^{57.9}_{48.8}$
52638.6 – 52999.6	$77.8^{86.9}_{77.4}$	$67.5^{69.1}_{66.1}$	$53.4^{56.6}_{50.3}$
53168.4 – 53437.5	$52.4^{53.8}_{50.6}$	$86.5^{92.1}_{80.1}$	$78.9^{83.9}_{75.1}$
53350.6 – 53527.4	$49.5^{50.9}_{42.0}$	$70.1^{70.4}_{69.8}$	$37.4^{40.5}_{32.2}$
54181.6 - 54332.3	$64.9^{65.8}_{63.2}$	$60.5^{62.2}_{59.0}$	$51.7^{53.6}_{49.5}$

Table 2.2: NGC 5548 (UV/optical 1928 to 5468 Å) Edelson et al. Data Table Lag in days (MJD 56706.0 - 56833.6). The uncertainties are the minimum (lower) and maximum (upper) values.

Band	Javelin Lag	PyROA Lag	Sour Lag
W2	–	–	–
M2	$0.206^{0.506}_{0.079}$	$0.006^{0.058}_{-0.045}$	$-0.011^{0.135}_{-0.151}$
W1	$0.452^{0.699}_{0.259}$	$0.172^{0.227}_{0.118}$	$0.313^{0.443}_{0.176}$
U	$0.820^{0.967}_{0.679}$	$0.932^{1.003}_{0.863}$	$1.151^{1.285}_{1.022}$
B	$0.865^{0.986}_{0.748}$	$0.844^{0.926}_{0.763}$	$1.109^{1.268}_{0.942}$
V	$0.524^{0.650}_{0.356}$	$1.142^{1.279}_{0.997}$	$1.389^{1.684}_{1.164}$

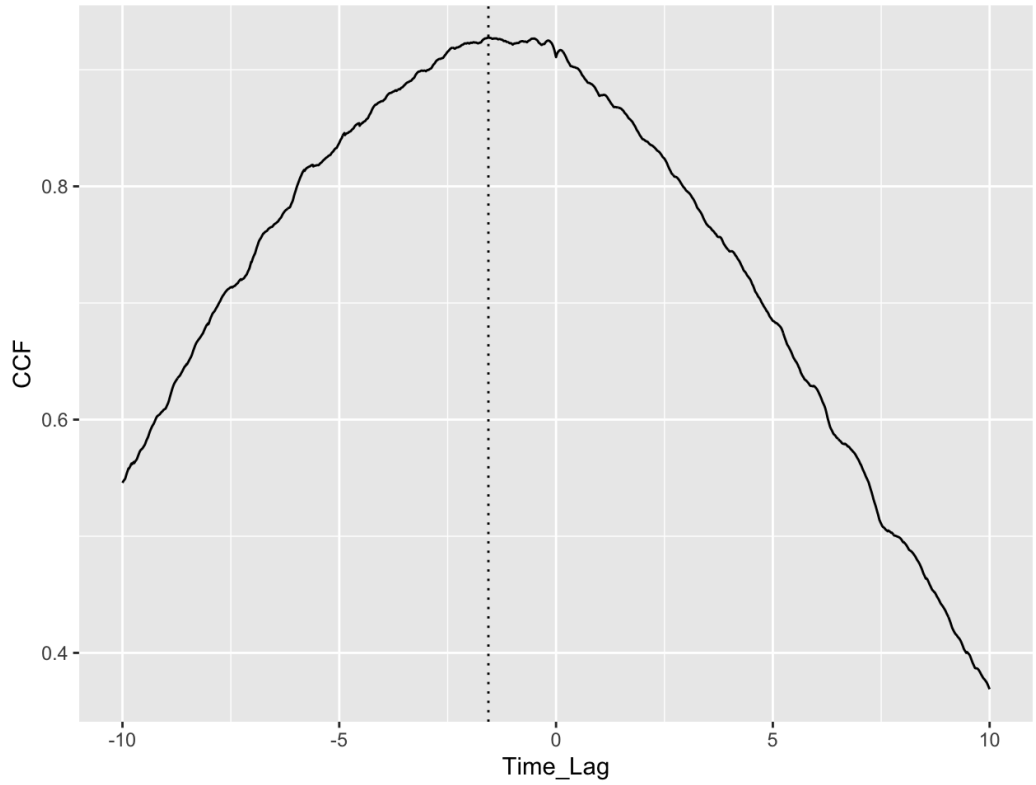

Figure 2.3: Interpolated cross-correlation for the V and K bands of Koshida et al. (2014) for the W2-V band light curves. The x-axis time lags are in days. The maximum lag and number of simulations were set at 10 and 500 respectively.

et al. (2019) were 5 UV/Optical bands (W2, M2, W1, U, B, V in order of increasing wavelength). Typical estimates of the size of NGC 5548's accretion disc is 1 light day (Ebrero et al., 2016). Time lags were calculated by comparing a wavelength band with the W2 band by assuming that it is the continuum driver. The dataset does not possess the sampling gaps seen for the dust RM campaign in Koshida et al. (2014) owing to the higher mean cadence of 0.440 days and an observation period of 127.6 days. Narrow lag distributions, indicating good convergences, were found with a burn-in and sampling iterations of 10000 for both Javelin and PyROA. Initial lag estimates for PyROA were obtained from Edelson et al. (2019). The effect of good cadence can be seen by the tight error overlays. After utilising the multi-threading functionality within Javelin, convergence times are similar to PyROA's at $\sim$ 30 mins.

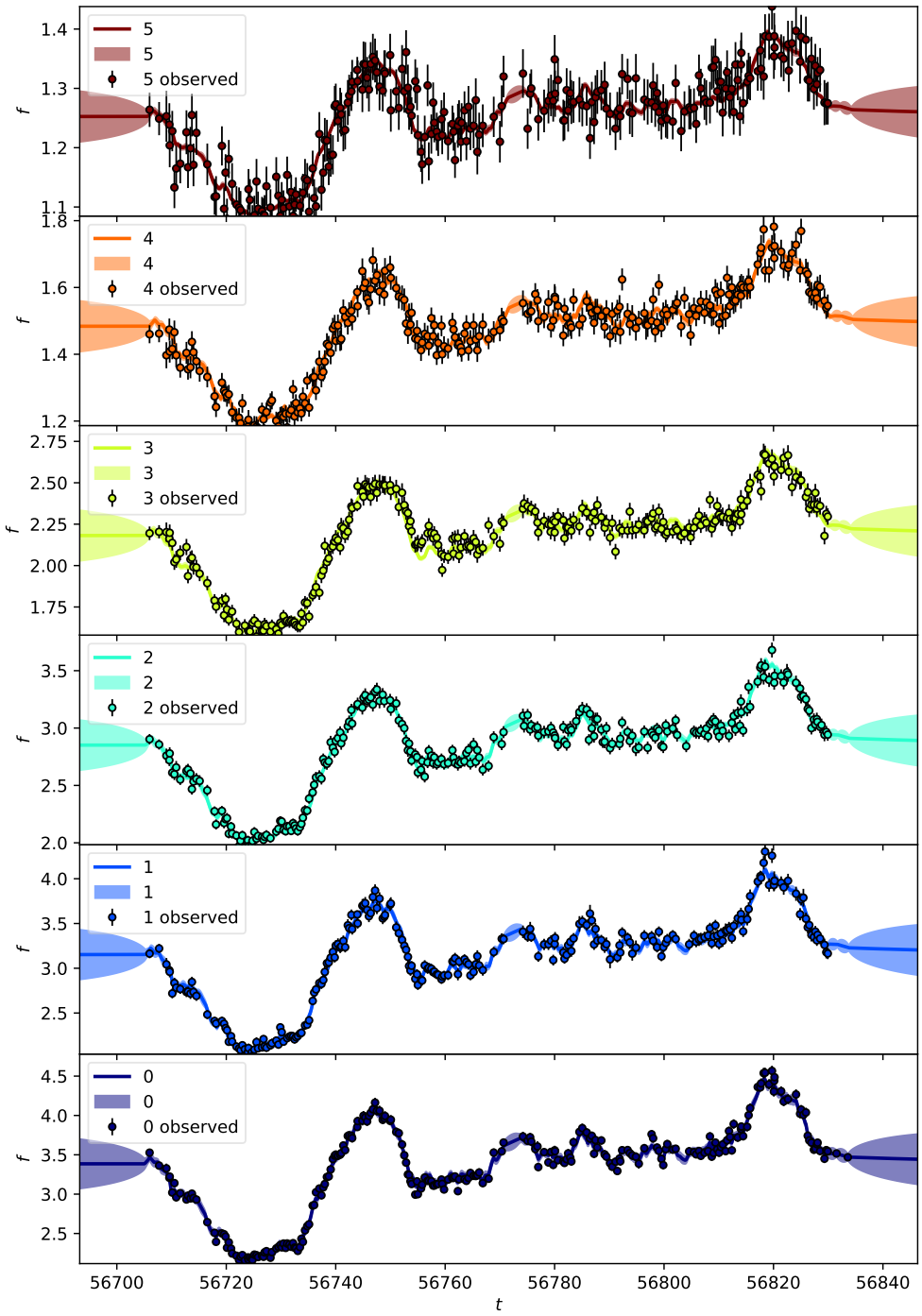

Figure 2.4: Javelin multi-band fit for Edelson et al. (2019). Flux units are in erg cm^{-2} s^{-1} Å^{-1} and time units are in days (MJD). Longer photometric bands correspond to redder colours with the W2 band being blue and brown corresponding to the V band.

Table 2.2 shows good agreement between the Javelin, PyROA and Sour for all wavebands apart from the M2 lags where there is an order of magnitude difference between the three lag estimates. The lag uncertainties are the minimum (lower) and maximum (upper) values. The Javelin uncertainties mean that the lag do not agree with PyROA and Sour, however, PyROA and Sour are in agreement. This suggests systematic differences in the uncertainty estimates between the three algorithms. Furthermore, Javelin seems to consistently overestimate the lags when compared to PyROA and Sour. When compared with the Javelin estimates in Edelson et al. (2019) further parameter optimisations and a poor convergence of the MCMC sampling could account for this systematic discrepancy. A notable feature in both PyROA and Sour, (but seemingly not Javelin) is that the U band lag is greater than the V band lag resulting from the 'Balmer excess' (Edelson et al., 2019). Further details of this phenomenon will be discussed in the next section. Finally, Javelin's disc mode was utilised in figure 2.6 to check whether the lag estimates converted into accretion disc radii are close to the Shakura-Sunyaev thin disc prediction of $R_\lambda \propto \lambda^{\frac{4}{3}}$. Javelin's disc mode shows very good agreement with the thin disc model, however, more detailed analysis and comparison with fits from PyROA and Sour needs to be conducted. Preliminary analysis suggests better agreement with the thin disc model for the M2, W1, and U bands but a substantial drop in radii estimates for the V bands. This drop is not present for PyROA and Sour and may account for the β discrepancy.

2.3 Discussion

2.3.1 Dusty Torus Reverberation Mapping

The weighted average time-lags for the dust RM campaign by Koshida et al. (2014) shown in table 2.1 show good agreement between all three algorithms, as they are the same order of magnitude and there is overlap between the minimum (lower) and maximum (upper) lag values across three columns. However, Javelin and PyROA

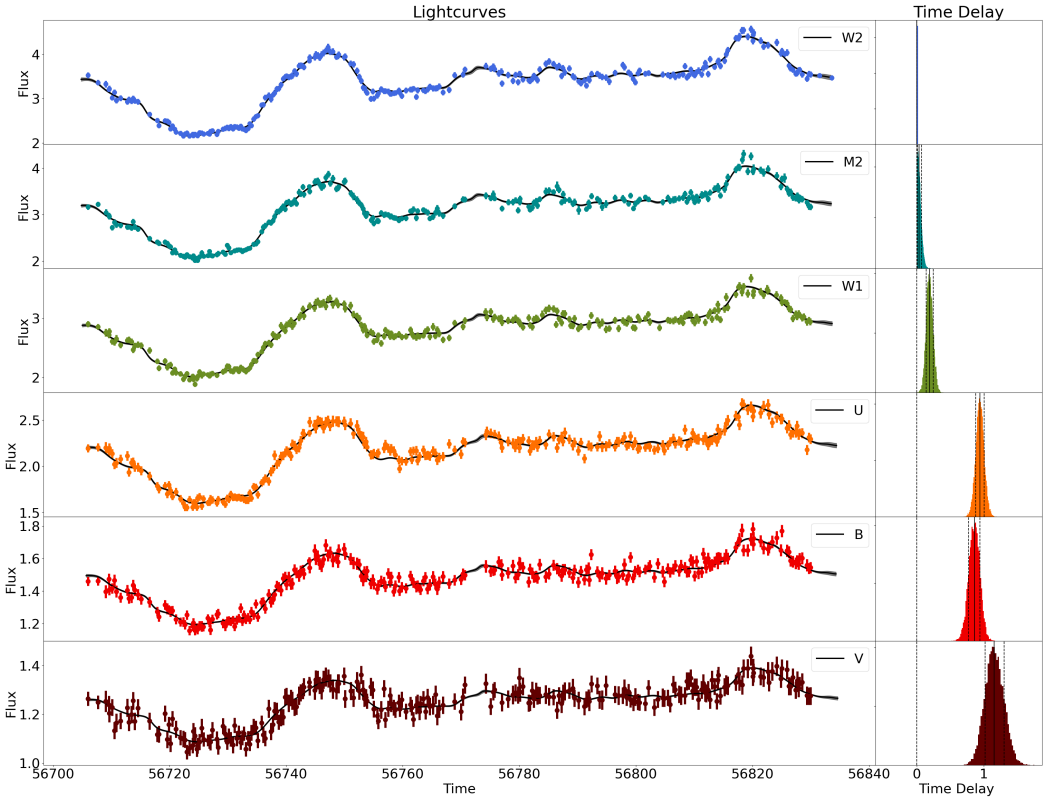

Figure 2.5: PyROA multi-band fit for Edelson et al. (2019). Flux units are in erg cm^{-2} s^{-1} Å^{-1} and time units are in days.

show better agreement with each other than with Sour. This may be because Javelin and PyROA are biased towards larger time lags. In the case of Javelin, this may be explained by larger than necessary lag search limits that produce wide lag distributions that may include aliased peaks, biasing towards larger lag estimates. Whereas for PyROA, it may be explained by a larger than necessary blurring with the transfer window width being too large, such that smaller timescale variability is smoothed over (Edelson et al., 2019). PyROA's unrealistic fit in figure 2.2 is due to a Gaussian transfer window function, the error overlay rapidly increases wherever there is a lack of data. Wider wings for the transfer window function would average over data points further away from the gaps and hence constrain the ballooning error overlay. This is presented in Donnan et al. (2021) with the best performance coming from a Lorentzian window function without significant differences in the time-lag estimates but some erroneous peaks arise on either side of the central time-

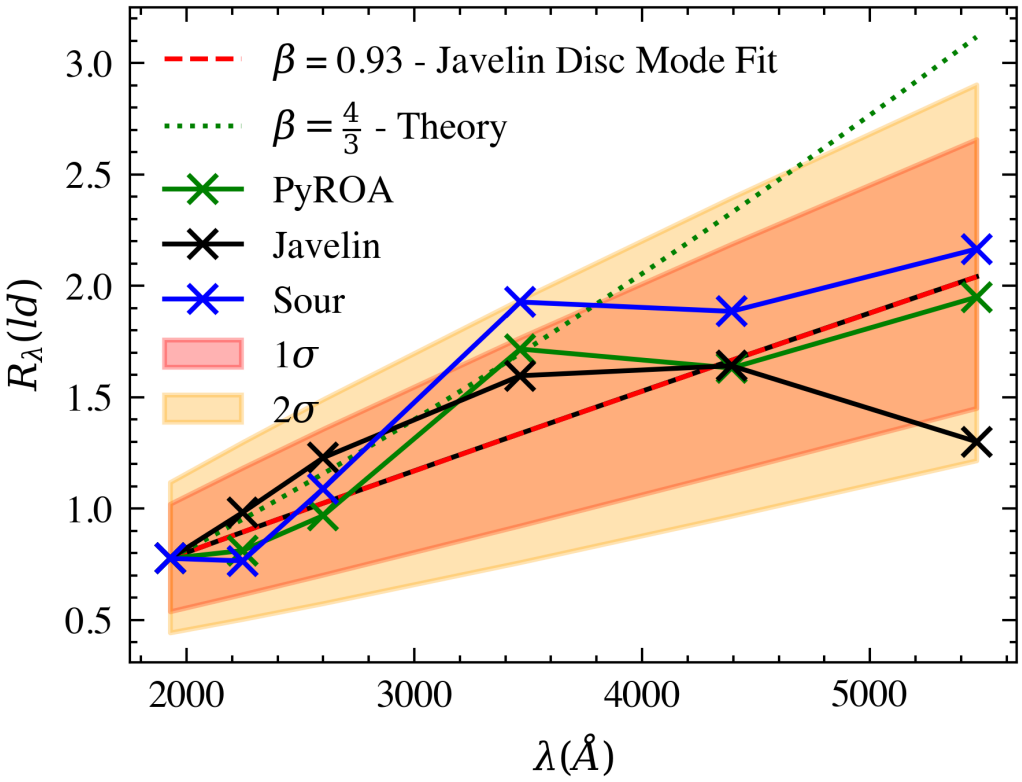

Figure 2.6: Javelin disc mode, time-lag radii against photometric wavelength band. The green dotted line shows the power law prediction for a thin disc and the red line shows the fit that Javelin produced with a $R_\lambda \propto \lambda^{0.93}$. The yellow and red error overlays show the 1σ and 2σ errors from Javelin's R_{λ_0} and β estimates. The blue, black and green lines with data points are the accretion disc lags converted into radii for Sour, Javelin and PyROA respectively.

lag peak. Testing the effects of different transfer window functions is an essential area of future study with PyROA. It should be noted that Edelson et al. (2019) also produces Javelin estimates that are slightly larger than the cross-correlation. It could also be the case that the Sour estimates are too low. On observation of Sour's cross-correlation plots for Koshida et al. (2014), we see the lack of a clear peak in several of the observing epochs, this is indicative of the tight maximum lag parameters that were set to eliminate aliases and could explain the discrepancy between Javelin, PyROA and Sour. From the perspective of aliasing, PyROA is the superior of the three and despite its poor fitting can produce accurate and robust time-lags. Quantitative testing of the robustness of the time-lag estimates against sampling gaps should be undertaken by varying the sampling rate and observing

changes in the lag estimate. No significant difference was observed in the errors between Javelin and PyROA despite the Javelin methodology underestimating the photometric uncertainties when compared to PyROA. However, this seems to be highly dependent on the source as Edelson et al. (2019) and Donnan et al. (2021) observed and demonstrated this effect. Further development of a method that integrates PyROA's error propagation into Javelin's code should be explored to fully test this effect. Finally, we note the existence of a time-varying accretion disc flux component contaminating the K band. The time-varying flux emission in the near-IR from the accretion disc is almost synchronous with that in the optical, this may lead to a systematic reduction in estimated time-lags. The resultant effect on the time-lags leads to an error $\sim$ 5% (Koshida et al., 2014). Accounting for this by assuming a power-law relation ($f_{KBand,\,Disc}(t) = f_{VBand}(t)(\frac{\nu_K}{\nu_V})^{\alpha_\nu}$, where $\alpha_\nu = 0, +\frac{1}{3}$ for with and without accretion disc contamination (Koshida et al., 2014)). Cross-correlation methods from Koshida et al. (2014) yield a $\sim 4\%$ error due to the accretion disc contamination, however, Javelin obtained $< 1\%$ (Koshida et al., 2014). Suggesting that the accretion disc contamination could explain the discrepancies observed between Javelin, PyROA and Sour and that Javelin is not sensitive enough, the DRW model assumed by Javelin is strictly only valid for variability longer than $3-5$ days ($\sim 5\%$ for a predicted time-lag of 70 days), more than enough to mask any systematic errors due to the accretion disc.

The broader context of a dust RM campaign in the V and K bands is to understand the structure geometry of the outer accretion disc, the BLR, and the dusty torus. In the unified paradigm of AGN, dust is distributed in a thick parsec-scale torus that obscures the view of BELs and disc continuum for large (for large inclination angles relative to the axis perpendicular to the disc plane). This is unsupported by observations (Dexter et al., 2020) that show an excess in the near-infrared (NIR) due to thermal emission from hot dust grains ($T = 1200 - 2000\,\mathrm{K}$). The excess may result from the inner edge of the dusty torus near the dust sublimation radius where the dust temperature is the highest because irradiation is maximal. Koshida

et al. (2014) find that the BLR reverberation radius for NGC 5548 is systematically smaller (factor of $4-5$) than the dust reverberation radius as reported by Suganuma et al. (2006) and suggest that gas clouds with hot dust are located between the BLR and the innermost torus radius. Further constraints on torus models such as those proposed by Czerny et al. (2017); Baskin and Laor (2018) could be provided by spectroscopic RM campaigns targeting the variability of BELs as suggested by Landt et al. (2019), that determine dust properties to greater precision than photometry. These models unify the origin of the BLR and dusty torus into an outflow launched by radiation pressure from the outer accretion disc. Landt et al. (2019) find that for NGC 5548, the dust temperature is $1450\,\mathrm{K}$, implying that the dust is carbonaceous and not close to its sublimation temperature (carbon has a sublimation temperature of $T \approx 1800 - 2000\,\mathrm{K}$. In this case, the inner torus radius is not set by dust sublimation. Almeyda et al. (2020) models the temporal response of the torus' IR dust emission to variations in the UV/optical continuum using the TORMAC reverberation mapping code and speculates that the innermost torus is populated by clouds containing graphite grains, in agreement with the picture suggested by Landt et al. (2019) for NGC 5548.

2.3.2 Accretion Disc Reverberation Mapping

The accretion disc RM campaign of Edelson et al. (2019) has a far better cadence than the dust RM campaign in Koshida et al. (2014) resulting in aliasing not being a significant contributor to lag estimation. Table 2.2 presents the good agreement between Javelin, PyROA and Sour except for the M2 band where we see different orders of magnitude for each and Javelin being two orders of magnitude higher than PyROA. The unrealistically negative Sour M2 band estimate may be due to the far wider lag distributions when compared with Javelin and PyROA. When combined with Sour's symmetric treatment of lags a negative estimate may be plausible. The extra wideness was tested and is primarily due to aliased peaks mixing with real lags, this may be eliminated depending on the source and optimising the lag search

constraints. Lags obtained from the peak position of the cross-correlation instead of the centroid may be an interesting test of this extra wideness. Although centroid lags were thought to be more representative of the physical scale of the reverberating region (Gaskell and Sparke, 1986), estimates may be biased by asymmetric cross-correlation functions, due to aliased peaks for example, whereas peak position estimates may yield more realistic results. In any case, Sour highlights the inaccuracy of traditional interpolated cross-correlation methods for accretion disc RM. Symmetric treatments of the lag distributions also exist in Javelin and PyROA's default methodologies, encapsulated by the symmetry of the convolution operation in equation 1.13 and the symmetry about the y-axis of the transfer functions (Chan et al., 2020). Javelin by default uses a top-hat function and PyROA assumes the same window width Δ, resulting in a uniform and symmetric transfer function for both (Donnan et al., 2021). However, due to the smaller lag uncertainties, negative lag estimates seem to have been avoided. Showing that Javelin and PyROA are superior for obtaining realistic and physical lag estimates and thus scales of the reverberating regions. Both also have the ability to accept asymmetric transfer functions which may bring accretion disc RM analyses more in-line with the thin disc model. The transfer function of the thin disc model is asymmetric which results in continuum light curves that are not only shifted and blurred but also skewed. Chan et al. (2020) estimated that the use of symmetric transfer functions may account for time lag estimates that are $\sim 20\%$ smaller than in actuality which, of course, results in smaller than expected scales for the reverberating regions. From the perspective of the accretion disc size problem, Javelin and PyROA have the flexibility to integrate this new level of precision and it would be interesting to investigate the increased accuracy with the use of more physical transfer functions.

Finally, the Javelin estimate for the V band is less than half of the PyROA and Sour estimate, however the maximum value uncertainty keeps it in agreement with the PyROA and Sour lags. It isl be due to the lag limit hyperparameter for the V band being overly constrained. Therefore, a larger lag limit with a greater number

of samples for the V band may bring it to expectations. This does not significantly deviate the $\beta = 0.93$ from the $\beta = \frac{4}{3}$ when fitting for an accretion disc power law, however, a better agreement could be achieved. Edelson et al. (2019) present a suggestion for the clear U band jump in lag estimates that involves the Balmer excess (by a factor ~ 2.2), an unknown admixture across the U band of accretion disc emission and diffuse continuum BLR emission (Edelson et al., 2019) across UV/optical wavelengths. Modelling of the BLR emission needs to be conducted to estimate the level of BLR continuum contamination. Interestingly, lags for Javelin, PyROA and Sour for the M2, W1, and U bands (despite the known Balmer excess) seem to be in better agreement with the thin disc model ($\beta = \frac{4}{3}$) than if the fit included the B and V bands.

The inter-band continuum lags for the ICCFs and Javelin in Table 3 from Edelson et al. (2019) for NGC 5548 is in agreement with the lags from Javelin, PyROA and Sour found in this investigation (table 2.2) are within 1σ. This investigation accurately repeated Edelson et al. (2019)'s results with Sour, an ICCF algorithm but also found that the newer algorithms Javelin and PyROA can reproduce ICCF lags with smaller uncertainties. Therefore, Javelin and PyROA more precisely fits the expected $\tau \propto \lambda^{\frac{4}{3}}$ relationship. However, all three methodologies are within 1σ except for Sour in the U band and Javelin in the V band. PyROA is generally closer to the expected theory than Javelin and the V band result for Javelin might be indicative that Javelin has a tendency to be more unstable than PyROA. However, unusual deviant lags are not present in Edelson et al. (2019)'s Javelin lags and given the asymmetric errors, it is likely that the Monte Carlo simulation did not have enough iterations to converge. Furthermore, a lack of convergence is also indicated by the Javelin errors being a factor of ~ 3 larger than Edelson et al. (2019). A similar excess of errors is seen with the PyROA and Sour lags in table 2.2, indicating poor convergence and insufficient simulations respectively. However, further testing showed that Javelin's anomalous V band lag could be alleviated by increasing the number of iterations or by restricting the range of possible lag values

further.

In the broader context of this investigation, many RM campaigns have found that disc sizes are larger by a factor of $2-3$. Edelson et al. (2019) finds that after excluding the U band (due to BLR emission) the disc size i.e. RM lags are a factor of ~ 2 larger than what would be expected from a thin disc. Edelson et al. (2019) states that because the uncertainties are small this is not necessarily inconsistent with the thin disc model. However, larger-than-expected disc sizes have been commonly observed in several RM campaigns (e.g. Mudd et al. (2018); Kokubo (2018)). A partial explanation for the larger-than-expected disc size by Edelson et al. (2019) is the BLR continuum excess observed primarily in the U band, which this investigation finds. Balmer continuum emission from the BLR should vary on longer timescales than the disc, so frequency-resolved RM analysis could be used to remove the BLR component instead of excluding contaminated bands as Edelson et al. (2019) has done. Usual RM techniques cannot easily distinguish between disc and BLR emission. A recent example of frequency-resolved RM is Cackett et al. (2022) whereby the lags are calculated from each Fourier frequency of a given band to, in principle, separate out reprocessing on different size scales. They apply a maximum-likelihood, frequency-resolved method (for further details please refer to the paper.) to the same AGN storm data set used in this investigation to produce 4 or 5 frequency bins depending on the light curve cadence. Figure 2 in Cackett et al. (2022) displays the lags in comparison to ICCF lags (not frequency resolved) from Fausnaugh et al. (2016). They find that lags resolved with frequency bins less than $0.1\,\mathrm{days}^{-1}$ (or a variability period of 10 days) do not evolve significantly, indicating that reprocessing from size scales less than $10\,\mathrm{light}-\mathrm{days}$ occurs quickly which is then biased by variability on scales larger than $10\,\mathrm{light}-\mathrm{days}$ to give a picture similar to the ICCF results from Fausnaugh et al. (2016) and table 2.2. Lags not produced from frequency-resolved incorporate timescales of $\sim 27\,\mathrm{days}$. Accretion disc response functions from Cackett et al. (2007) were used to match the ICCF lags for NGC 5548 and they found that frequency-resolved lags are more consistent with

a standard-sized accretion disc with a contribution from the BLR emission over a larger-than-expected thin disc. Where the BLR becomes an additional reprocessor at larger distances compared to the accretion disc.

2.4 Summary

This chapter is one of the first comprehensive comparisons of Javelin and PyROA with traditional cross-correlation methods for reverberation mapping. This was conducted on multi-wavelength band data from the dusty torus and the accretion disc regions of NGC 5548. This has primarily been done with the motivation of developing new and optimising existing light curve analysis techniques to produce realistic scale estimates for application to accretion disc modelling and precision cosmology. The latter involves constraining scale estimate structures within AGN and, therefore, estimations for the Hubble parameter. In summary;

- Lag estimates from Javelin, PyROA, and Sour agree with the expectation of ~ 70 light days for the dusty torus. Cross-correlation methods suffered from an underestimation of time-lags when compared with Javelin and PyROA which is attributed to aliasing effects that result from the poor cadence of the dataset. This may be evidence of accretion disc contamination and Javelin may mask the accretion disk contamination due to a lack of sensitivity on timescales of a few days. The significance of the accretion disc contamination must be modelled in future studies. Despite, PyROA's unrealistic fits, it produces realistic time-lag estimates and these unrealistic fits may be reduced with the use of alternative window functions. The robustness of all three against sampling and uncertainties must be studied to conclude which is optimal for the dusty torus regime.

- All three algorithms produce consistent accretion disc-like estimates for the Edelson et al. 2019 dataset. Aliasing effects are significantly reduced due

to the far better cadence of this dataset when compared with Koshida et al. 2014. Significant problems arise with the cross-correlation due to the symmetric treatment of lags and aliasing effects, this is also present with Javelin and PyROA but it does not result in unrealistic estimates. To obtain better agreement with the thin-disc model, asymmetric transfer functions should be implemented with Javelin and PyROA. Proper modelling of the BLR component to deal with the optical jump in lags as conducted by Cackett et al. (2022) to produce realistic scale estimates for structures within AGN. Doing so will facilitate a better grasp of the accretion disc size problem, estimating the black hole mass, and precise Hubble parameter estimates.

Chapter 3

Continuum Reverberation Mapping for Mrk 1239

3.1 Introduction

For a geometrically-thin disc (Shakura and Sunyaev, 1973), the temperature-radius profile follows $T(R) \propto R^{-\frac{3}{4}}$ and the corresponding time delay increases with wavelength as $\tau \propto \lambda^{\frac{4}{3}}$. As per the reprocessing picture, any time-lag, τ can be interpreted as $\tau \approx \frac{R}{c}$ of the disc due to light travel time c and the peak of a black-body emission is given by Wien's law $\lambda_{max} = \frac{b}{T}$. Where b is Wien's displacement constant. 'Slim' discs, at super-Eddington rates, should however show a different temperature-radius profile with $T(R) \propto R^{-\frac{1}{2}}$ resulting in a lag spectrum $\tau \propto \lambda^2$. Furthermore, the temperature profiles for the thin and slim discs produce spectral power-laws that are $F_\nu \propto \lambda^{-\frac{1}{3}}$ and $F_\nu \propto \lambda$, respectively.

There are now many disc (continuum) RM studies (Fausnaugh et al., 2016; Edelson et al., 2019; Hernández Santisteban et al., 2020) finding delay spectra compatible with $\tau \propto \lambda^{\frac{4}{3}}$ and thus consistent with the expected thin-disc temperature profile at sub-Eddington accretion rates. However, the inferred disc sizes are consistently larger than expected by typically a factor of ~ 3 (Mudd et al., 2018). Cackett et al. (2020) performed the first intensive continuum RM study for a super-Eddington

quasar and found a delay spectrum consistent with either a thin or slim disc but a SED that strongly followed $f_\nu \propto \lambda^{-\frac{1}{3}}$, expected for a thin disc temperature profile.

Several explanations have been proposed to explain the larger-than-expected lags (resulting in the factor of 3 larger disc size). Most recently, Starkey et al. (2023) introduces a 'steep rim' near the dust sublimation radius of the disc resulting in matching observed and predicted optical lags. Furthermore, Cackett et al. (2023) fit the 'steep rim' model to X-ray UVOT light curves from Mrk 817 and found that it accurately reproduced the lag spectrum. They found that it accounted for the larger-than-expected lags in the UV but also matched the flattening of the lags seen in the optical. It also corroborated the significant deviations from the expected lags in the X-ray.

A better test of the rimmed disc model would be to include longer-wavelength optical light curves, as the RM campaign used in this investigation, to validate the plateauing lag spectrum relation seen in Cackett et al. (2023). A rimmed disc's outer regions would be illuminated by the lamp post more strongly compared to a thin disc thereby increasing the local temperature and shortening the emitted wavelength, resulting in lags that appear to come from a larger radius if a thin disc is assumed. The effect of reddening has not been explored on RM lags thus far, which highlights uncertainty in the estimated accretion rate of AGN as it determines the observed flux level of the disc (variable in nature) emission. For a thin disc, the mass accretion rate $\dot{M} \propto R_{disc}^3$ and so a larger accretion rate would imply a larger disc radius - potentially being an explanation for the larger than expected disc sizes measured by current RM campaigns.

Here we present results from the first dedicated accretion disk reverberation mapping campaign on the narrow-line Seyfert 1 galaxy Mrk 1239. In Section 2, we discuss the science target and give the details of the observations and data reduction in Section 3. In Section 4, we outline the methods used to obtain lag estimates and theoretical predictions and present our results. In Section 5, we discuss the derived physical scales of the accretion disk and how they relate to the 'thin disk

model'. Finally, in Section 6, we present a short summary and our conclusions. We have assumed throughout cosmological parameters $H_0 = 69.6$ km s^{-1} Mpc^{-1}, $\Omega_m = 0.286$ and $\Omega_\lambda = 0.714$.

3.2 Target Selection

The object Mrk 1239 (Table 3.1) was shown to exhibit a narrow-line Seyfert 1 (NLS1) AGN by Rafanelli and Bonoli (1984). However, Pan et al. (2021) suggested that Mrk 1239 exhibits characteristics that make it closer to a Seyfert 2 AGN. Notably, the high degree of polarisation ($P \sim 5.6\%$) is heavily obscured with $E(B-V) = 1.6$. Mrk 1239 was the highest polarised source observed by Goodrich (1989) and the Balmer lines had a higher polarisation than the forbidden lines suggesting a physically distinct origin. Pan et al. (2021) finds the bolometric luminosity to be $L_{Bol} = 2.5 \pm 0.5 \times 10^{45}\,\mathrm{erg\,s^{-1}}$ and the black hole mass to be $M_{SMBH} = 9,4 \pm 0.6 \times 10^6\,\mathrm{M_\odot}$. Pan et al. (2021) obtained the black hole mass estimate by measuring the width of the Paschen β, γ, and δ BELs in the near-infrared (NIR) with a full with at half maximum (FWHM) of $FWHM_{\mathrm{NIR\,BEL}} = 1090 \pm 80\,\mathrm{kms^{-1}}$.

Based on the extinction-free model for transmitted AGN radiation, the luminosity at 5100 Å is scaled with a bolometric correction factor L_{5100} (Richards et al., 2006) to give the bolometric luminosity. Doi et al. (2015) reported that Mrk 1239 is a radio-quiet Fanaroff-Riley Type 1 galaxy with parsec-scale jet structures with evidence of non-stellar radio emission originating from the AGN. Interestingly, initial analyses of the soft X-ray spectrum in the range $0.3 - 3.0$ keV found it was remarkably consistent over 20 years, dominated by the host galaxy as the central engine is heavily obscured Pan et al. (2021). However, Buhariwalla et al. (2023) found evidence of ionised emission originating from two equally bright plasmas, one photoionised and one collisionally ionised. The former matches the outflow velocity of the forbidden $O-VII$ emission line and is constrained to originate from no closer than the inner radius of the torus (a few pc from the central source).

Table 3.1: Object properties. We have assumed throughout cosmological parameters $H_0 = 69.6$ km s^{-1} Mpc^{-1}, $\Omega_m = 0.286$ and $\Omega_\lambda = 0.714$.

Object	*RA (J2000)	[a]Dec (J2000)	[†]D_L (Mpc)	z
Mrk 1239	09 52 19.102	-01 36 43.46	87.2	0.019927

3.3 Overview of the Data

Despite the inner regions of Mrk 1239 being heavily obscured it exhibits strong variability at UV/optical wavelengths. It is thus an ideal candidate to probe the sizes of accretion disks, and to validate standard accretion disk theory. Using high signal-to-noise and high-cadence light curves, this reverberation mapping analysis aims to test standard accretion disk theory and to provide constraints on the size of the accretion disk in Mrk 1239.

The 7-band photometric light curves of Mrk 1239 were obtained from the Las Cumbres Observatory (LCO) global robotic telescope network. Mrk 1239 was observed as part of an intensive disc reverberation mapping campaign from 2021 December 21 to 2022 April 10 (111 days) achieving an average sub-daily cadence of ~ 0.415 days. The range of cadences in each band is given in the fourth column of table 3.2. Multi-band data was captured with the Sinistro cameras on the LCO 1-m robotic telescopes. Each covers a 26.5×26.5 arcmin^2 field of view with a $4K \times 4K$ pixel array of 15 μm CCD pixels with 0.389 arcsec pixel^{-1}). Exposures were taken in pairs (table 3.2 to account for cosmic ray impacts and for internal consistency of the flux error estimates.

CCD image data from the LCO archive provided bias and flat-field corrected images processed with *BANZAI* (McCully et al., 2018). Multi-aperture aperture photometry was extracted with *SEXTRACTOR* (Bertin and Arnouts, 1996) on every image. The images were smoothened in a 200 pixel mesh with a global background model, large enough to avoid extended sources influencing the background estimate. After subtracting the background model and performing the aperture

photometry, the aperture photometry was performed with a 5 arcsecond radius aperture, providing light curves robust against a range of atmospheric conditions (e.g. airmass, seeing) taken throughout the year and at different sites without compromising the signal-to-noise ratio. Comparison stars in each field were used to perform an image zero-point calibration at each epoch. The AAVSO Photometric All-Sky Survey (APASS) DR10 (Hernández Santisteban et al., 2020) for the g', r', i', B and V filters, and for zs Pan-STARRS1 (Flewelling et al., 2020). For the u' band, where no APASS information was available, the Swift/UVOT U band images were used to obtain the fluxes of reference stars in the field. All colour correction and atmospheric extinction coefficients were obtained from Valenti et al. (2016) and applied before the photometric calibration. 3σ clipping was applied to the zero-point estimates and bootstrap samples used to estimate uncertainties. This procedure is identical to the one outlined in Hernández Santisteban et al. (2020); Donnan et al. (2023). Since multiple telescopes contributed to the data, the observations from different telescopes were intercalibrated and merged to form a single light curve for a given filter. The method, firstly, determines telescope-specific scale factors arising from different CCD sensitivities and the filter and telescope transmissions. And secondly, background flux offsets, arising from different angular aperture sizes or angular resolution. The light curve photometry and inter-calibration were pre-processing steps conducted before this investigation obtained them.

The presence of strong broad emission lines (BELs) within some of the photometric windows of the optical bands means that there are expected to be flux excesses in certain bands (table 3.3), hence, multiple bands were used as the 'driver' in the reverberation mapping analysis. Table 3.3 presents the line flux estimates for the fluxes of the strongest lines, this is to estimate the contribution and influence of the broad-line region (BLR) which is variable on the time scales of the accretion disc lags. The width of the Hα line is large enough that it might contribute to the r' band flux (see figure 3.1). Deviations from the expected power law could be

1m/Sinistro Filter	t_{exp} [s]	Epochs	Cadence [days]
u' (3540 Å)	2×300	268	0.415
B (4361 Å)	2×60	279	0.399
g' (4700 Å)	2×60	268	0.415
V (5448 Å)	2×60	280	0.397
r' (6215 Å)	2×60	265	0.420
i' (7545 Å)	2×60	257	0.433
z_s (8700 Å)	2×120	260	0.428

Table 3.2: LCO Photometry

due to diffuse continuum emission (DCE) from the BLR. This was accounted for by Hernández Santisteban et al. (2020). Furthermore, the Balmer bound-free continuum or Balmer jump can also contribute up to 40% of the observed continuum around the 3500 Å continuum as shown by figure 2 and table 3 of Edelson and Malkan (1986). The Balmer jump results from a stellar process whereby electrons in hydrogen atoms are ionised directly from the second energy level. This creates a continuum absorption at wavelengths shorter than 3500 Å. Mrk 1239 contains strong Balmer lines which correlate with the Balmer jump resulting in a continuum bump (Knigge et al., 1998) seen in figure 3.1.

1m/Sinistro Filter	Passband	BEL	Line Flux $\left[\times 10^{-13}\frac{erg}{cm^2 s}\right]$	t_{exp} $[s]$	Epochs	Cadence [days]
u' (3540 Å)	3250 − 3750 Å	−	−	2×300	268	0.415
B (4361 Å)	3916 − 4781 Å	Hδ, Hγ	$H\delta:$ 1.64	2×60	279	0.399
			$H\gamma:$ 2.82			
g' (4700 Å)	4020 − 5520 Å	Hδ, Hγ	$H\delta:$ 1.64	2×60	268	0.415
			$H\gamma:$ 2.82			
		Hβ	$H\beta:$ 4.74			
V (5448 Å)	5028 − 5868 Å	-	-	2×60	280	0.397
r' (6215 Å)	5520 − 6910 Å	$H\alpha$	$H\alpha:$ 21.0	2×60	265	0.420
i' (7545 Å)	6900 − 8190 Å	$H\alpha$	$H\alpha:$ 21.0	2×60	257	0.433
z_s (8700 Å)	8180 − 9220 Å	OI	$OI:$ 2.65	2×120	260	0.428

Table 3.3: LCO photometry for Mrk 1239, including the contaminant line fluxes estimated by fitting the broad emission lines (BELs) in the MIKE spectrum.

3.4 Time-series analysis and results

In this section, we first derive theoretical lag predictions and then present a continuum reverberation mapping analysis of Mrk 1239 using Javelin, PyROA and Sour. Tables 3.5, 3.6, 3.7 show the photometric lags from the LCO (Las Cumbres Observatory) light curves in the Bessel (U, B, V), SDSS (g', r', i'), and Pan-STARRS (z_s) filters.

3.4.1 Theoretical Lag Predictions

To validate the assumptions of reverberation mapping and the time lags the methodologies extracted, a theoretical disc model was fitted to a contemporaneously obtained optical spectrum of Mrk 1239 - obtained on 01/04/2022. The spectrum was measured from the red and blue arms of the MIKE echelle spectrograph (Bernstein et al., 2003) on the Magellan telescope. The combined spectrum spanning 3300Å − 9500Å. The black hole mass and bolometric luminosity were taken from Pan et al. (2021) and were $M_{BH} = 9.4 \times 10^6$ $M_\odot$ and $L_{Bol} = 2.5 \times 10^{45}$ ergs^{-1} respectively. These result in a mass accretion rate of $\dot{M} = 0.44$ $\frac{M_\odot}{Yr}$ from $L_{Bol} = \epsilon \dot{M} c^2$, assuming an efficiency factor of $\eta = 0.1$. The resulting Eddington ratio is then $\frac{L_{Bol}}{L_{Edd}} = 2.1$.

An Eddington ratio of 2.1 as suggested by Pan et al. (2021) is unusually large and instead, the SMBH mass is likely to be a factor of 10 larger. To demonstrate this we fit a thin disc model spectrum to the observed MIKE spectrum to derive an estimate of the mass accretion rate. Assuming the SMBH mass from Pan et al. (2021), a disc temperature profile can be constructed that relates disc temperature to disc radius (equation 3.17 from Peterson (1997)). Wien's law then allows the midpoint wavelengths of the LCO bands to be related to a characteristic disc temperature. However, the reality as mentioned in Chapter 1 equation 1.9 that every disc annuli contributes to a wide wavelength range of disc emission that can be red or blue

shifted which needs to be accounted for. Typically this comes in the form of a corrective factor of order unity and Mudd et al. (2018); Fausnaugh et al. (2016) state that is dependent on the wavelength of emission and black hole mass, for NGC 5548 they found it to be 2.49. RM assumes that the relevant time scales are light travel time across the disc radius so that the wavelengths of the LCO bands correspond to disc radii defined by an estimate of the mass accretion rate. Fig. 3.2 presents three thin discs over a smoothened MIKE spectrum from $3800\text{Å} - 4100\text{Å}$, a range informed by the known factors that affect the shape of the continuum as described in section 3.3. The green dash-dot line corresponding to the Eddington ratio from Pan et al. (2021) is a factor of a few larger than the MIKE continuum seen. By eye, the MIKE spectrum continuum suggests that the Eddington ratio is roughly $10\% - 15\%$ of the Pan et al. (2021) estimate as can be seen by the pink dashed line in figure 3.2. This continuum range was chosen from the blue end of the spectrum to maximise the amount of disc emission while fitting. It should be acknowledged that this is not a good fit beyond 4100 Å and is done solely to check the Eddington ratio estimate in Pan et al. (2021) and to inform the Eddington ratio for the theoretical lags. The theoretical lags will then later be used to scale the measured lags to illustrate the differences with the thin disc model. We take a value of 14% $L_{Bol} = 2.5 \times 10^{45}\,\mathrm{erg\,s^{-1}}$ (Pan et al., 2021) to calculate the theoretical lags in the second column of table 3.4 and the first column representing the mass accretion rate implied by 100% of Pan et al. (2021) is kept for reference. The 14% value was obtained by aligning a thin disc spectrum to the un-reddened z_s band RMS flux as can be seen in figure 3.20 and it fits within the $10 - 14\%$ range estimated above.

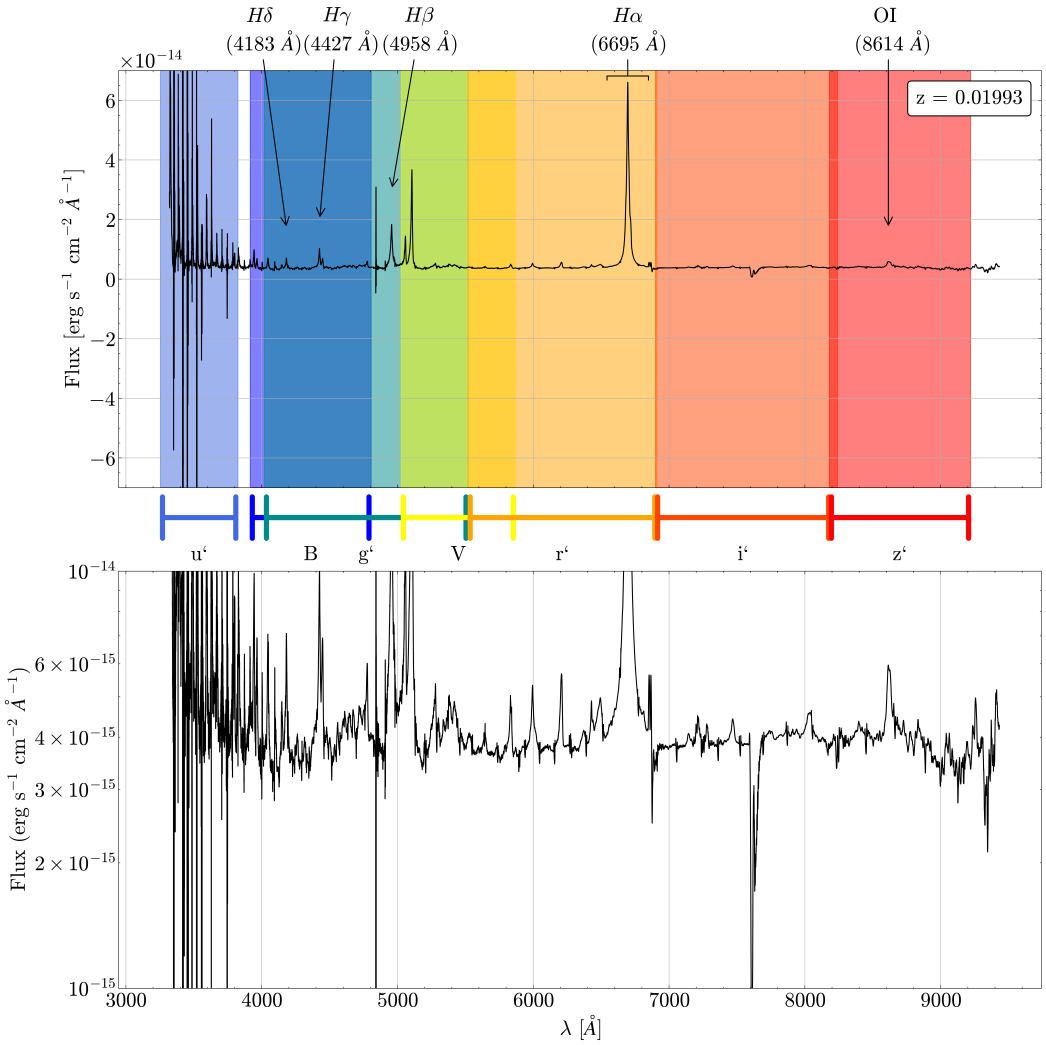

Figure 3.1: Top: MIKE Spectrum in the observed frame smoothened with a Savitzky-Golay filter (Savitzky and Golay, 1964) with a window length of 150 days and a fitting polynomial order of 3. The contaminant BELs are indicated by arrows and the coloured ranges represent the spectral widths of the photometric bands. The Hα line width may also influence the i' band. Bottom: MIKE spectrum plotted with a log flux scale to see the continuum level.

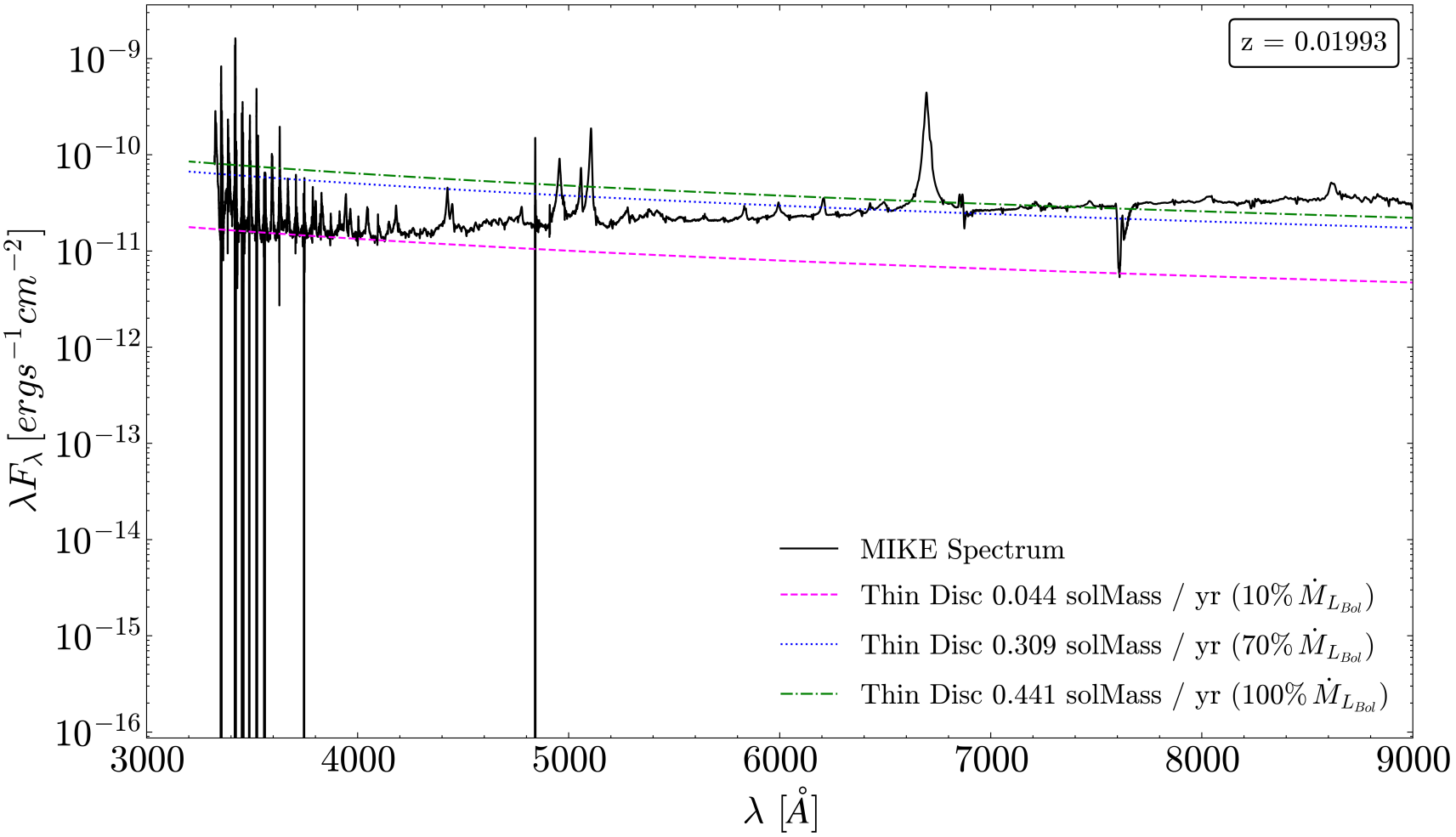

Figure 3.2: Thin disc fits the MIKE spectrum in the rest frame at Eddington ratios $R_{Edd} = 0.21$, 1.48, and 2.12 corresponding to 10%, 70%, and 100% of L_{Bol} (Pan et al., 2021) fitted between 3800 Å − 4100 Å and shown between 3000 Å − 9000 Å.

	Time Lag [days]	
Band	$(0.44\frac{M_\odot}{Yr})$ $\dot{m} = 2.12$	$(0.06\frac{M_\odot}{Yr})$ $\dot{m} = 0.30$
u (3540 Å)	–	–
B (4361 Å)	0.322	0.161
g (4700 Å)	0.451	0.236
V (5448 Å)	0.751	0.386
r (6215 Å)	1.073	0.558
i (7545 Å)	1.663	0.869
z (8700 Å)	2.210	1.148

Table 3.4: Theoretical lags as implied by Eddington ratios at 100% and 14% of the bolometric luminosity estimate from Pan et al. (2021) respectively.

3.4.2 Interband continuum lags

	u	B	g	V
u	–	$-0.975^{+0.502}_{-0.516}$	$-2.078^{+0.666}_{-0.634}$	$-1.765^{+0.583}_{-0.624}$
B	$1.113^{+0.337}_{-0.389}$	–	$-1.053^{+0.577}_{-0.559}$	$-0.521^{+0.875}_{-0.840}$
g	$1.386^{+0.479}_{-0.536}$	$1.001^{+0.531}_{-0.571}$	–	$0.634^{+0.692}_{-0.671}$
V	$1.403^{+0.403}_{-0.385}$	$1.452^{+0.586}_{-0.550}$	$1.538^{+0.560}_{-0.574}$	–
r	$1.910^{+0.554}_{-0.589}$	$1.803^{+0.465}_{-0.431}$	$1.678^{+0.538}_{-0.489}$	$1.608^{+0.579}_{-0.634}$
i	$2.410^{+0.571}_{-0.536}$	$2.124^{+0.804}_{-0.841}$	$2.030^{+0.700}_{-0.761}$	$2.077^{+0.644}_{-0.653}$
z	$3.600^{+0.751}_{-0.799}$	$2.497^{+1.056}_{-1.054}$	$2.595^{+0.916}_{-0.941}$	$2.758^{0.845}_{0.852}$

Table 3.5: Matrix of interband continuum lags for the Javelin algorithm. Each column is the lag measured relative to one of u, , B , g or V bands.

	u	B	g	V
u	–	$-0.908^{+0.295}_{-0.305}$	$-0.614^{+0.310}_{-0.317}$	$-1.607^{+0.258}_{-0.270}$
B	$0.886^{+0.309}_{-0.313}$	–	$0.268^{+0.259}_{-0.272}$	$-0.716^{+0.207}_{-0.207}$
g	$0.631^{+0.303}_{-0.310}$	$-0.259^{+0.260}_{-0.261}$	–	$-0.969^{+0.222}_{-0.223}$
V	$1.601^{+0.267}_{-0.279}$	$0.711^{+0.201}_{-0.209}$	$0.988^{+0.216}_{-0.226}$	–
r	$1.595^{+0.285}_{-0.294}$	$0.698^{+0.228}_{-0.241}$	$0.984^{+0.249}_{-0.255}$	$-0.014^{+0.186}_{-0.193}$
i	$2.340^{+0.309}_{-0.327}$	$1.448^{+0.272}_{-0.286}$	$1.730^{+0.264}_{-0.275}$	$0.733^{+0.228}_{-0.233}$
z	$2.029^{+0.369}_{-0.385}$	$1.139^{+0.333}_{-0.353}$	$1.402^{+0.334}_{-0.355}$	$0.430^{+0.289}_{-0.297}$

Table 3.6: Matrix of interband continuum lags for the PyROA algorithm.

3.4.3 Cross-correlation Analysis

The multi-band light curves were first normalised using a Z-score, subtracting the mean and dividing by the standard deviation. The mean and variances were cal-

	u	B	g	V
u	$-$	$-0.497^{+0.377}_{-0.400}$	$-2.001^{+0.626}_{-0.605}$	$-1.545^{+0.528}_{-0.656}$
B	$0.480^{+0.403}_{-0.401}$	$-$	$-0.654^{+0.551}_{-0.659}$	$-0.896^{+0.345}_{-0.315}$
g	$2.038^{+0.570}_{-0.643}$	$0.607^{+0.690}_{-0.604}$	$-$	$-0.679^{+0.704}_{-0.598}$
V	$1.481^{+0.667}_{-0.533}$	$0.848^{+0.336}_{-0.332}$	$0.611^{+0.596}_{-0.712}$	$-$
r	$2.695^{+0.482}_{-0.515}$	$1.653^{+0.376}_{-0.437}$	$1.219^{+0.614}_{-0.473}$	$0.780^{+0.528}_{-0.656}$
i	$2.665^{+0.673}_{-0.675}$	$1.712^{+0.479}_{-0.540}$	$1.535^{+0.302}_{-0.463}$	$0.901^{+0.372}_{-0.432}$
z	$3.553^{+0.960}_{-1.382}$	$1.161^{+0.759}_{-1.103}$	$1.998^{+1.589}_{-0.942}$	$1.274^{+0.658}_{-0.838}$

Table 3.7: Matrix of interband continuum lags for the Sour algorithm.

$Zero-point$	$Javelin$	$PyROA$	$Sour$
u	$-0.004^{+0.681}_{-0.667}$	$-0.049^{+0.388}_{-0.326}$	$0.004^{+0.286}_{-0.285}$
B	$0.008^{+0.773}_{-0.719}$	$-0.068^{-0.248}_{+0.358}$	$0.000^{+0.331}_{-0.312}$
g	$0.048^{+0.733}_{-0.691}$	$-0.051^{+0.249}_{-0.238}$	$0.012^{+0.560}_{-0.487}$
V	$-0.152^{+0.670}_{-0.940}$	$0.015^{+0.143}_{-0.155}$	$-0.000^{+0.379}_{-0.373}$

Table 3.8: zero point lag measurements for Javelin, PyROA and Sour.

culated locally using only pairs of data contributing to a given lag bin. The motivation behind this lies in the fact that AGN variability is weakly non-stationary (Hernández Santisteban et al., 2020) so a 'local' normalisation is more appropriate than a 'global' normalisation. Each CCF result consisted of a correlation power (in arbitrary units) against time lag, with a peak where the degree of similarity between the two input light curves is the highest. The location of this peak using the centroid midpoint at 80% of the highest point, was then taken as the time lag estimate. The centroid measure was chosen as Koratkar and Gaskell (1991) showed that it is correlated with the luminosity-weighted reprocessing region and so can be interpreted as a physical quantity.

Furthermore, due to the uneven sampling of the AGN light curves, a 'two-way' interpolation for each pair of bands was implemented. The CCF power was calculated, first, by interpolating in the driving light curve and then re-calculated by interpolating in the lagged light curve. These two CCFs were then averaged to produce a final CCF that is symmetric in keeping with the idea that an autocorrelation function is an even function and hence, symmetric and normally distributed (Peterson et al., 1998; Hernández Santisteban et al., 2020). The method of interpol-

ation used was ICCF (interpolated cross-correlation functions) whereby the method validity depends on whether the gaps between flux measurements are sufficiently small such that a linear interpolation between them is a reasonable approximation for the true behaviour of the light curve. The u and B bands were initially chosen as the driving light curve because they have the shortest wavelengths and therefore closest to the peak of the thermal disc emission. The analysis was then expanded to the g and V bands for consistency.

The FR/RSS (flux randomisation/ random subset selection Peterson et al. (1998)) method was then used to provide model-independent time lag uncertainties. This is a Monte Carlo technique that builds up a time lag distribution from multiple realisations of a CCF for a given pair of light curves. In each realisation, Gaussian noise is added onto each flux measurement depending on the flux error, assuming they are normally distributed. Additionally, for a light curve consisting of N points, the FR/RSS method picks a subset of points with replacement to create a new time series. The data points that were selected more than once had their error bars decreased by a factor of $R^{-\frac{1}{2}}$, where r' is the number of times a data point is selected. $\left(1-\frac{1}{N}\right)$ is the probability that a data point is not selected in a given realisation so that $\left(1-\frac{1}{N}\right)^N \rightarrow \frac{1}{e}$ is the fraction of the data set not selected in a given realisation. This is because each data point has the same independent probability of not being selected. The CCF is then measured and the weighted mean of all the points above 80% of the highest CCF power value. The time lags presented in table 3.7 are the median centroid lags determined from 500 realisations with the errors being the 68% confidence intervals. This number of realisations was chosen to optimise the running time and a larger number did not reduce the errors significantly.

3.4.4 Javelin

As per Zu et al. (2011)'s methodology, all light curves are assumed to be shifted, scaled, and smoothened versions of a user-specified 'driving' light curve. A DRW

model is defined by an exponential covariance function $\sigma^2_{DRW} exp^{\frac{-\Delta t}{\tau_{DRW}}}$, where $\Delta t = |t_i - t_j|$ is the time separating two observations in time. σ_{DRW} and τ_{DRW} are the DRW model parameters. Physically, τ_d is the exponential damping timescale of a random walk. Using a Markov Chain Monte Carlo (MCMC) calculation, the shifts and re-scaling parameters for all the light curves were fit simultaneously, providing a well-defined and self-consistent means of interpolating all the light curves.

For Javelin to avoid measuring aliased peaks, initial runs were conducted to qualitatively identify time-lag peaks that are symmetric around a time lag of 0 and then limits were set on the possible values for the time-lag values. Aliasing can occur due to the uneven sampling of AGN light curves (Zu et al., 2011). Three key parameters for the MCMC simulation were nwalker (50), nburn (100), and nchain (50) with the default values given in brackets. They are the number of MCMC walkers, the number of burn-in iterations, and the MCMC chain length. The default values were not sufficient to fit 7 light curves simultaneously and so were set to 250, 200, and 200 respectively. And the final time lag limits were set to different values depending on which band was set as the driver (table: 3.9).

	u‘	B	g‘	V
u	–	$[-2.5, 0.5]$	$[-3.5, 0.0]$	$[-3.5, 0.0]$
B	$[0.0, 2.0]$	–	$[-2.5, 0.5]$	$[-2.5, 0.5]$
g	$[0.0, 2.5]$	$[-0.5, 2.5]$	–	$[-1.0, 1.0]$
V	$[0.20, 2.5]$	$[0.0, 3.0]$	$[0.0, 3.0]$	–
r	$[0.50, 3.5]$	$[0.5, 3.0]$	$[0.5, 3.0]$	$[0.0, 3.0]$
i	$[0.75, 4.0]$	$[0.0, 4.0]$	$[0.0, 4.0]$	$[0.2, 4.0]$
z	$[1.0, 5.5]$	$[0.0, 5.0]$	$[0.0, 5.0]$	$[0.5, 5.0]$

Table 3.9: Matrix of time lag limits for Javelin. The left and right elements of each array represent the lower and upper limits of the possible lag value for that pair of light curves.

For this investigation, the Javelin ‘spectroscopic’ multi-band mode was utilised on the 7 LCO light curves (see figure 3.3) to measure the inter-band continuum lags to then compare for consistency with two other methodologies. The 16th, 50th, and 84th percentile of the MCMC samples (or time lag distributions) were taken as the 1σ and estimate values of the observed frame time lags for each light curve

pair in table 3.5. An alternative Javelin mode that directly fit a thin disc model parameters was tested but it found poorly constrained parameters. However, fixing one of the parameters enabled the disc size or the power-law value to be estimated.

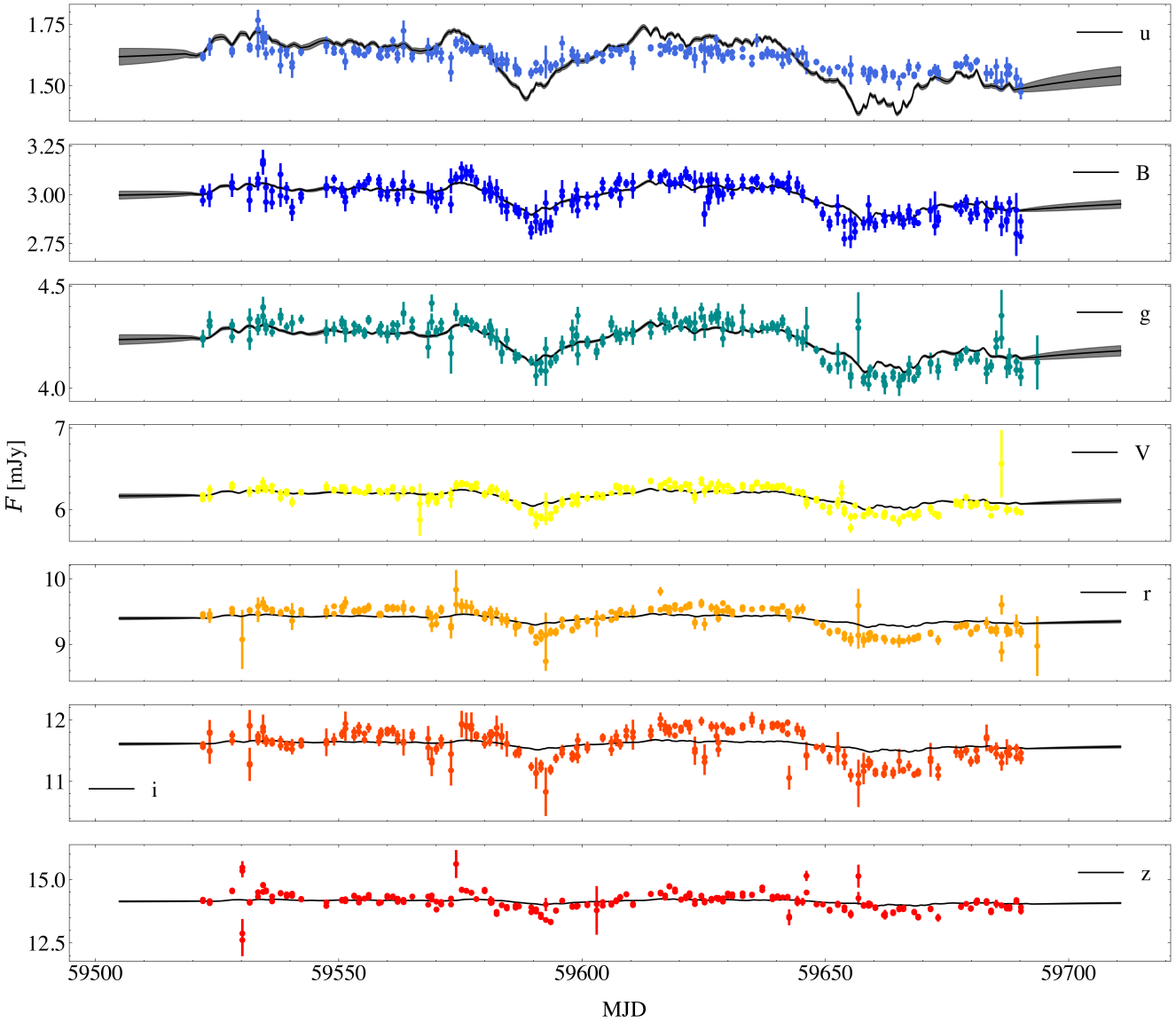

Figure 3.3: Model fits by the Javelin algorithm from the parameters used in table 3.9 when the u' band was set as the driver with wavelength increasing downward.

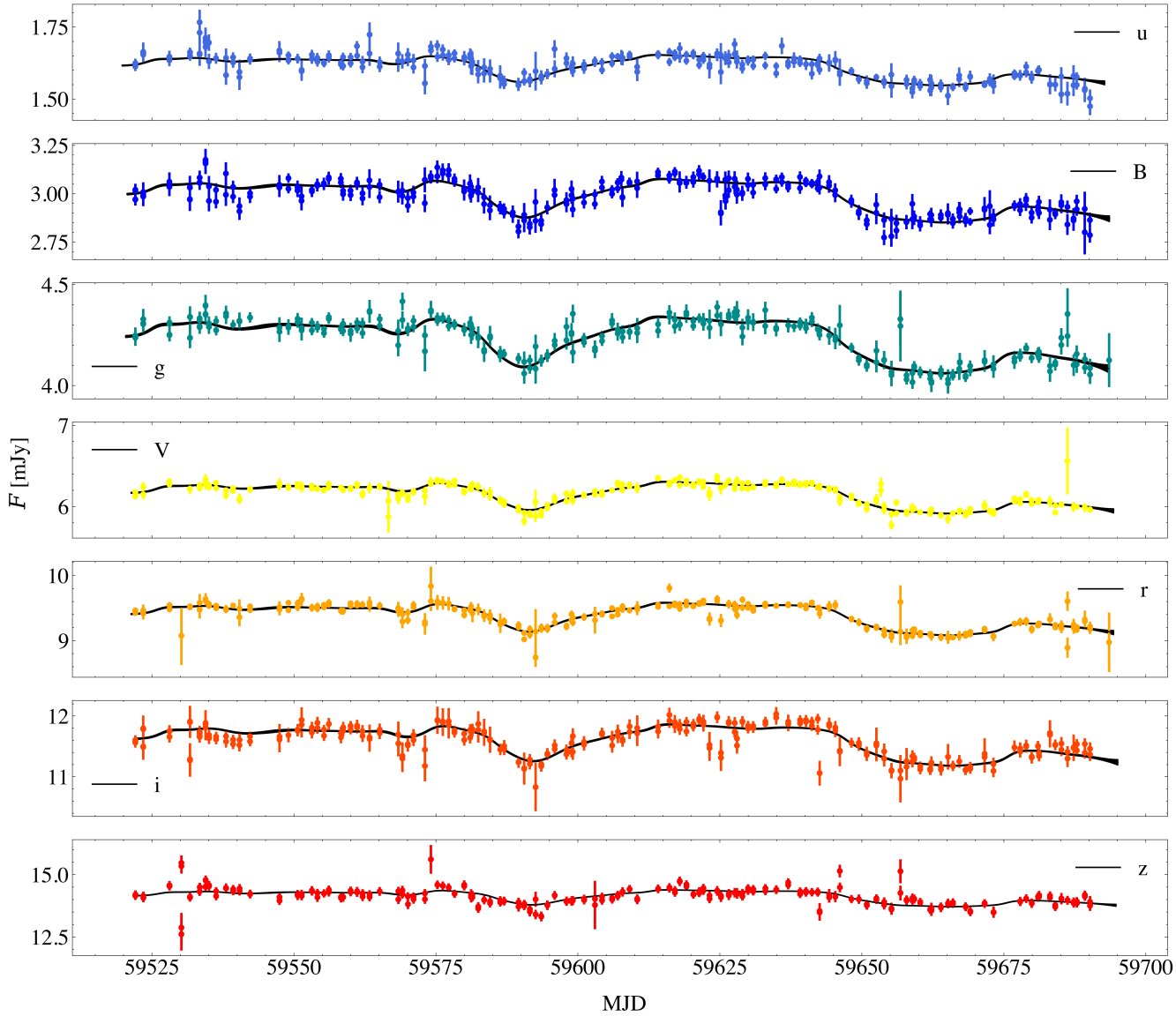

Figure 3.4: Model fits by the PyROA algorithm from the parameters used in table 3.10 when the u' band was set as the driver with wavelength increasing downward.

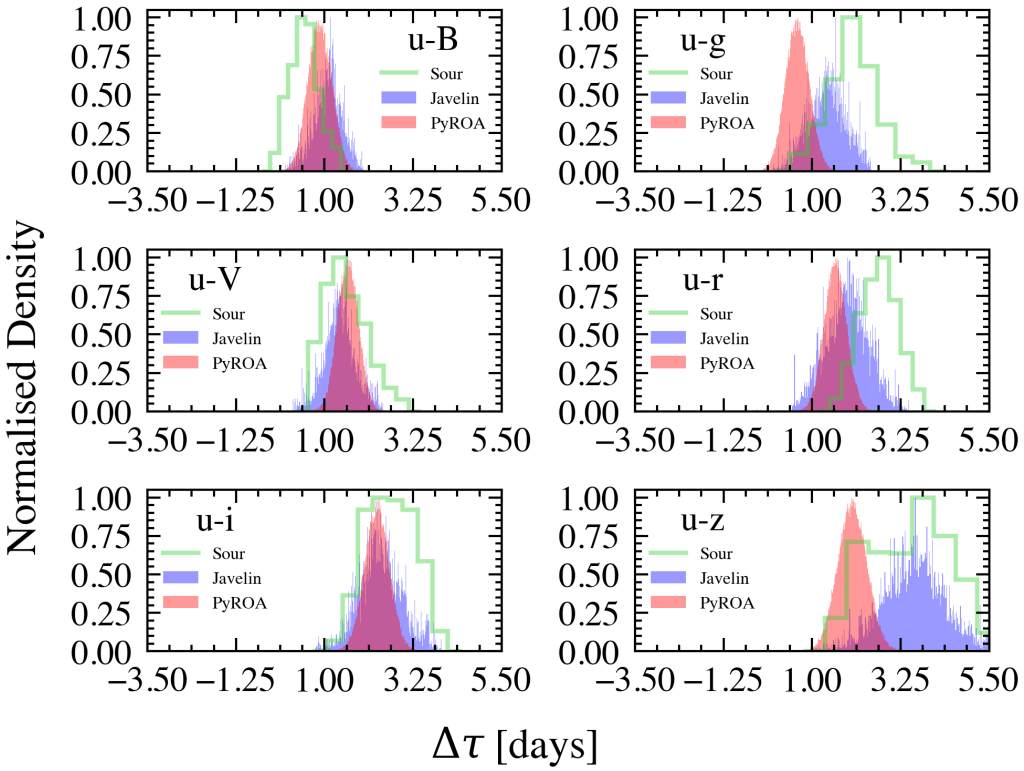

Figure 3.5: u band lag distributions for Javelin (blue) and PyROA (red) compared with the CCF centroid distribution (Sour) shown as the green outline.

3.4.5 PyROA

PyROA was applied to the 7 LCO light curves with the u‘, B, g‘, and V bands (see figure 3.4) set as the driving light curve (table 3.6) and again the 16th, 50th, and 84th percentiles of the MCMC time lag samples being taken as the 1σ errors and measured values respectively. To optimise for short run-times but small time lag errors the number of MCMC samples was set to 2500 with a burn-in iteration number of 5000. PyROA takes in a user-specified set of ranges for A_i, B_i, and τ_i - assumed to be the same range for all the light curves being fitted. Table 3.10 outlines the input ranges for the ROA model parameters used for all columns of table 3.6. Furthermore, extra variance was added to the flux errors for each light curve to account for additional uncertainty not included in the error bars (for further details refer to Donnan et al. (2021)).

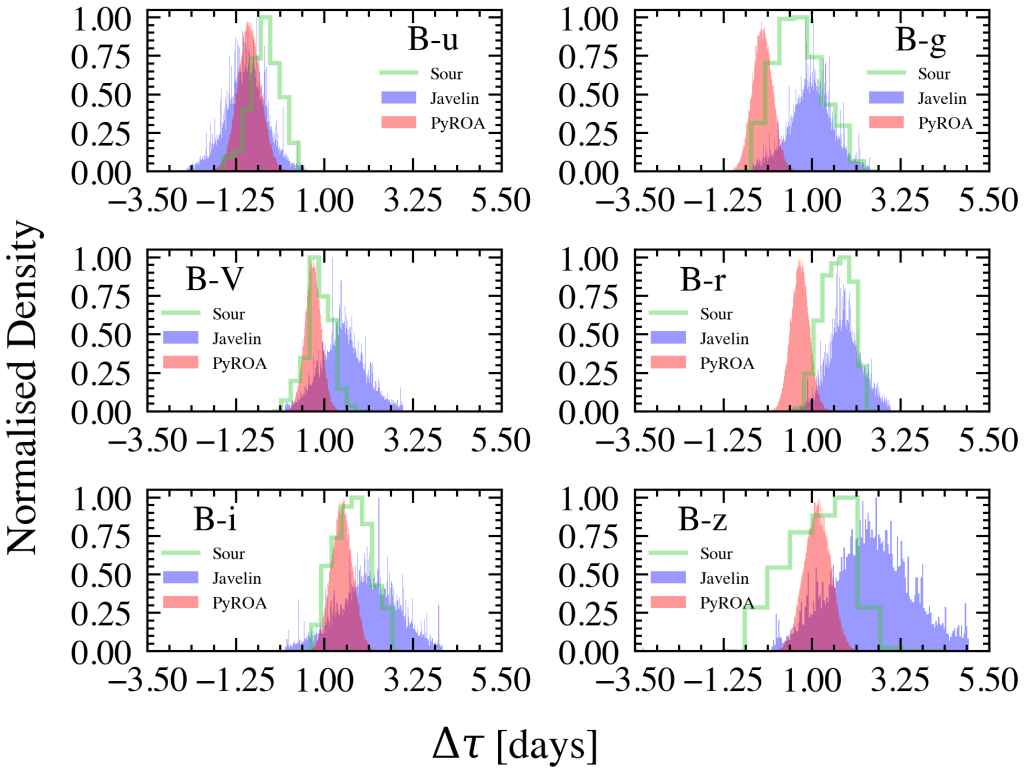

Figure 3.6: B band lag distributions for Javelin (blue) and PyROA (red) compared with the CCF centroid distribution (Sour) shown as the green outline.

A	B	τ	Δ	σ
$[0.0, 25.0]$	$[0.0, 25.0]$	$[-7.0, 7.0]$	$[0.01, 15.0]$	$[0.0, 10.0]$

Table 3.10: PyROA parameters used in table 3.6.

3.5 Interband Lag Results

Matrix tables 3.5, 3.6, and 3.7 present the results from Javelin, PyROA and Sour respectively. Each table's first, second and third columns represent the RM results with the u', B, g', and V bands set as the driver respectively. For the results to be consistent between different drivers, the expectation is that the lags are anti-symmetric ($\mathbf{L}^T = \mathbf{-L}$) about the leading diagonal of the matrix table. For example, the $u - B = -(B - u)$. Figures 3.6, 3.7, and 3.7 present the distributions from the three algorithms. The bins for Javelin and PyROA were set at 250 whereas the Sour bins were the default at 10 because the key comparison that was desired was

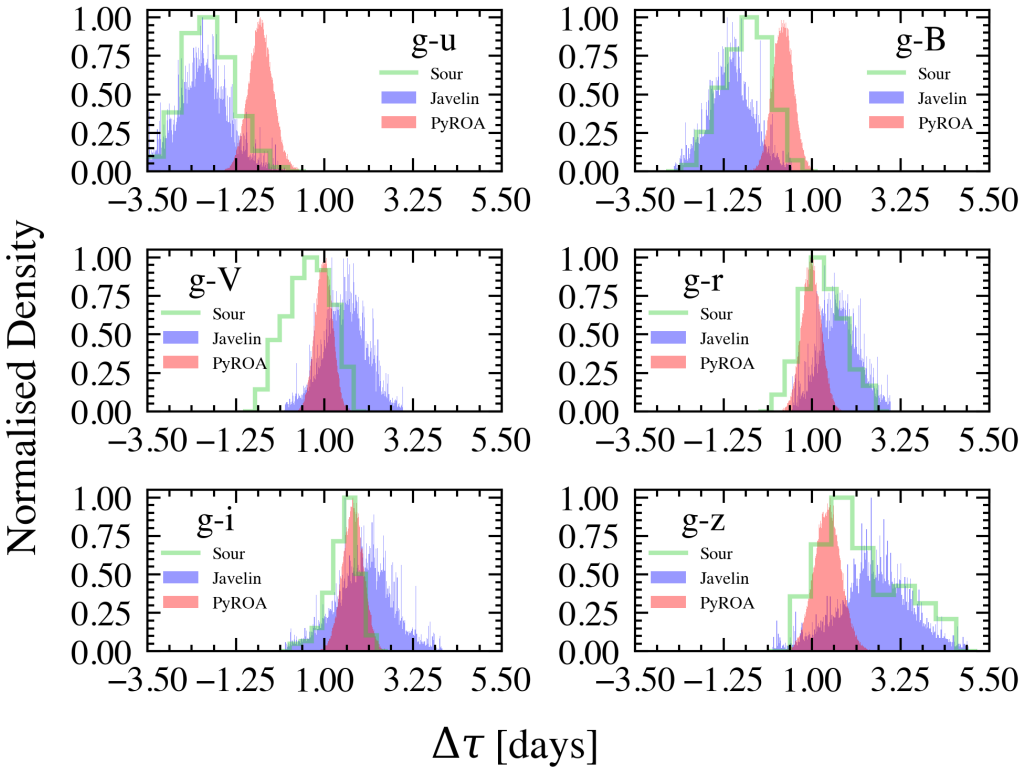

Figure 3.7: g band lag distributions for Javelin (blue) and PyROA (red) compared with the CCF centroid distribution (Sour) shown as the green outline.

between Javelin and PyROA as Sour is the legacy CCF algorithm.

It is vital to consider the significance level of each lag measurement from zero to motivate an interpretation of the lags. Generally, the longer the wavelength gap between a pair of bands the more important the lag measurement was. However, for Javelin, when the B and g' bands were set as drivers the lag errors were relatively larger than for the u' band. This meant only 3 out of 8 significant measurements that were not u' band driven. This was not the case for PyROA or Sour, which had consistent lag errors across different drivers. Table 3.8 presents estimates of the zero-point error from each of the three algorithms and the different drivers. The zero-point lag was found by duplicating the selected driving the light curve. The uncertainties were taken directly from the three algorithms, they are several orders of magnitude larger than the zero-point lags which suggests that the zero-point lag errors are consistent with 0 days. When the u band is set as the driver, the lags are

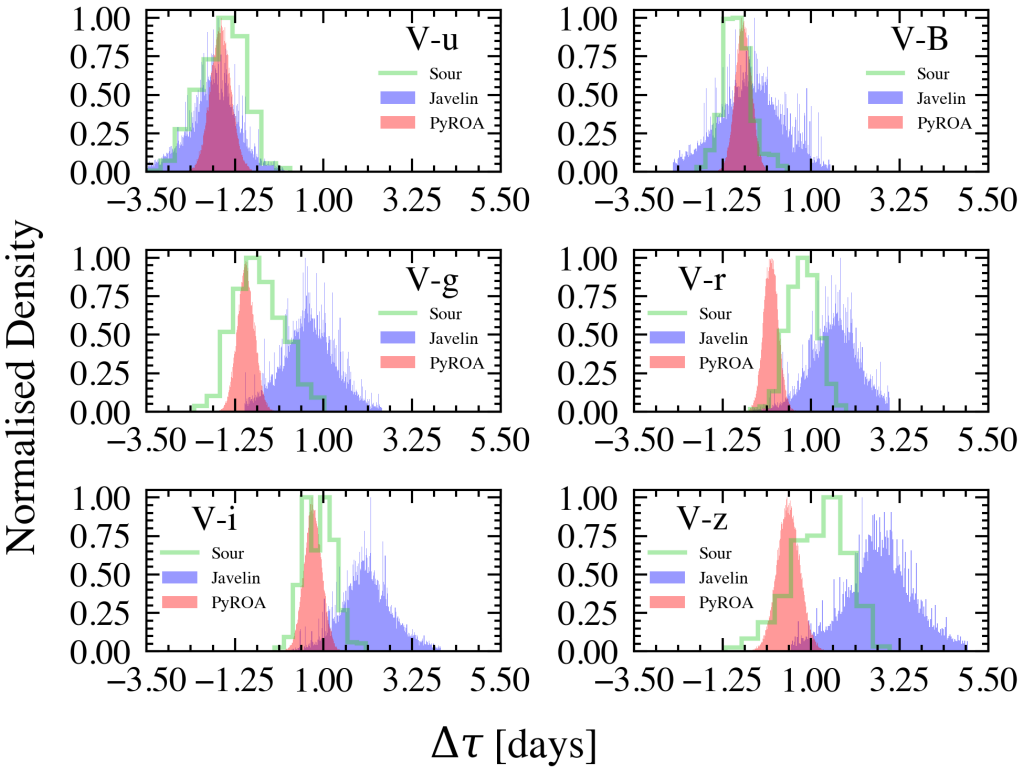

Figure 3.8: V band lag distributions for Javelin (blue) and PyROA (red) compared with the CCF centroid distribution (Sour) shown as the green outline.

greater than 2σ significance from the u' band zero point lag for wavelengths longer than the V band for Javelin and PyROA, and for wavelengths longer than the g' band for Sour. Interestingly, the zero point lag is larger in magnitude for Javelin as the driving light curve increases in wavelength. However, there is no consistent trend with PyROA or Sour.

Furthermore, it is also important to compare the deviation of the measured lags from their theoretical prediction as a function of wavelength. This is presented in fig. 3.9, 3.10, 3.11, and 3.12 representing the case when the u, B, g, or V bands are set as the driving light curve. The theoretical lag values used are the second column of table 3.4 representing 14% of L_{Bol} from Pan et al. (2021). Consistent across all the drivers there is a wavelength dependence of the divergence of the measured lags over the theoretical lags, with the lags in the u' and B bands being more divergent than those at longer wavelengths. However, PyROA is generally

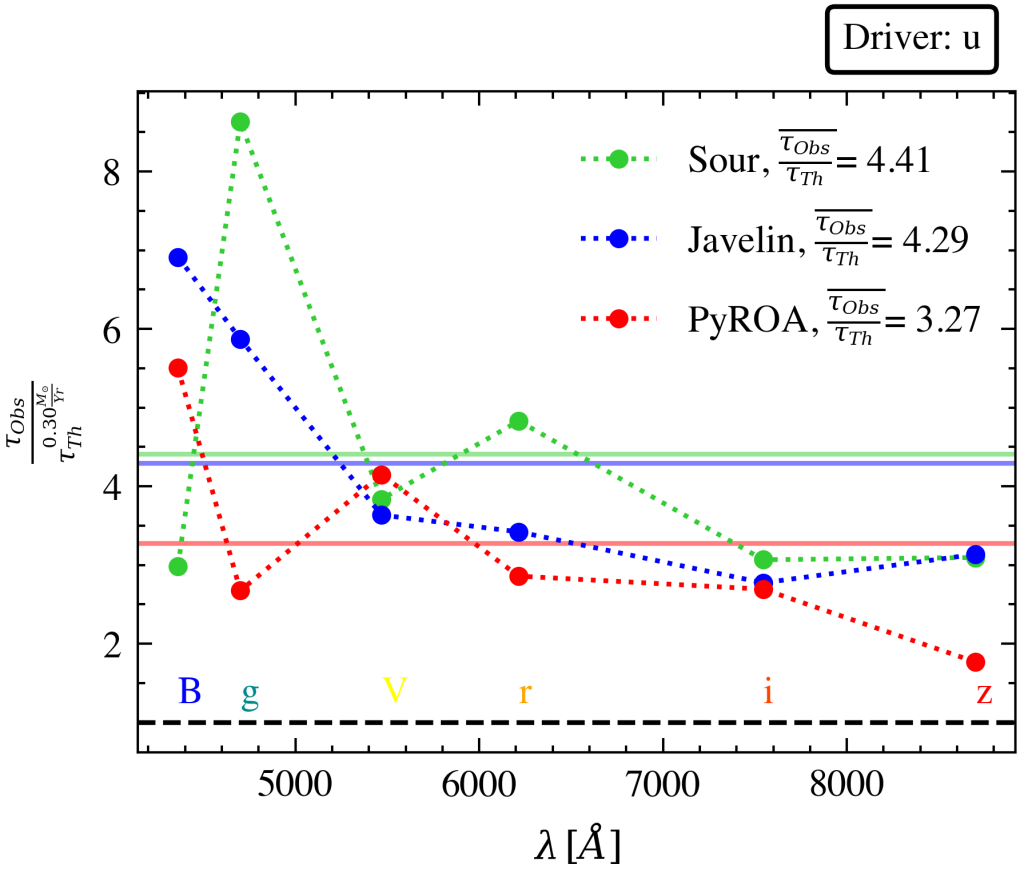

Figure 3.9: Measured lags scaled by theoretical lags relative to the u band for the B, g, V, r, i, z band. Horizontal solid green, blue and red lines are the average difference from the theoretical lags for Sour, Javelin and PyROA respectively.

the least divergent compared to Javelin and Sour. All three converge to 3× the theoretical estimate from the g' band onwards.

3.5.1 Lag Spectrum

The standard thin-disc model for irradiation comes from the lamp-post model (shown in figure 3.17 and Dovc˘iak et al.) which is a gross idealisation to simplify the calculations of the influence of light on the disc emission. The model states that most of the AGN power originates from a point-like patch of corona sitting above the plane of the disc and emitting power-law radiation. Although this model is non-physical, and there is a developing consensus from data against

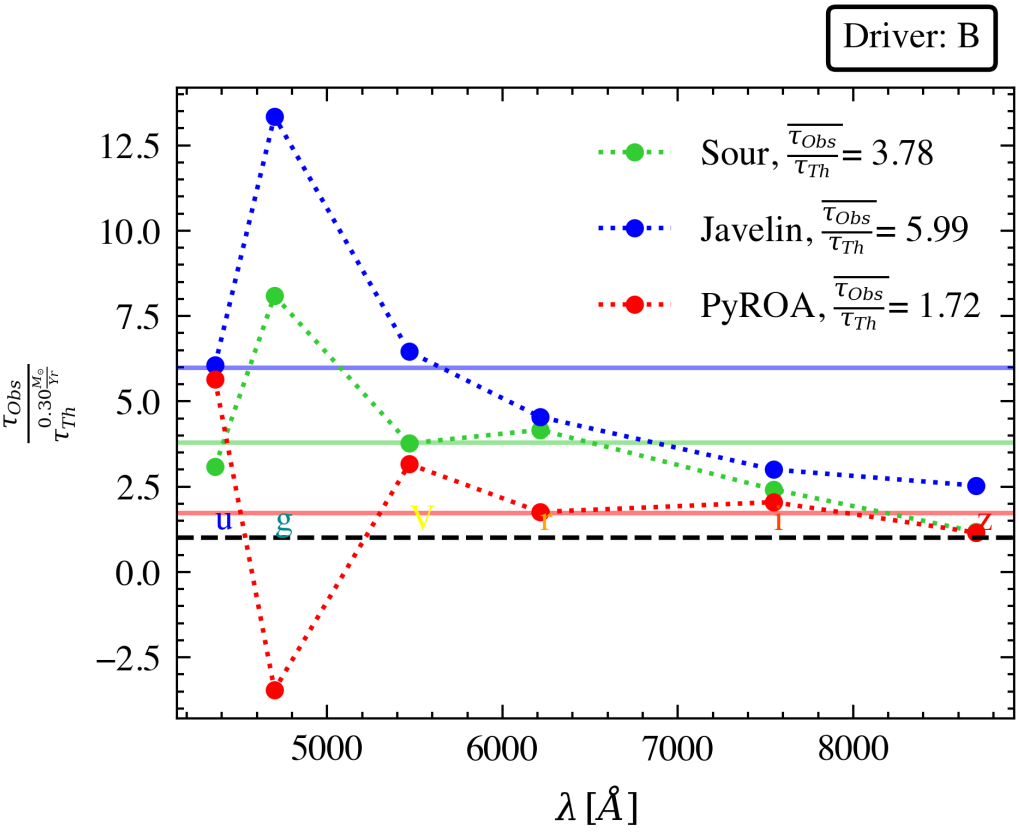

Figure 3.10: Measured lags over theoretical lags relative to the B band for the u, g, V, r, i, z band. Horizontal solid green, blue and red lines are the average difference from the theoretical lags for Sour, Javelin and PyROA respectively.

this model (Zoghbi et al., 2021), it still provides a useful comparison for the measured data and a test of alternative physical disc models (for example the rimmed disc model or discs that take into account relativistic corrections) because there is strong evidence for the reverberation of optical wavelengths within AGN. Section 4.5 and figure 8 in Krolik et al. (1991) also outline the thin disc model geometry required for disc fluctuations at different radii to reverberate. They claim that disc emission must be turned off completely within a certain gravitational radius.

The lamp post model predicts a disc radius-wavelength relation of $R \propto \lambda^{\frac{4}{3}}$, to test this prediction the lag spectrum, r', as a function of λ was fitted using the functional form:

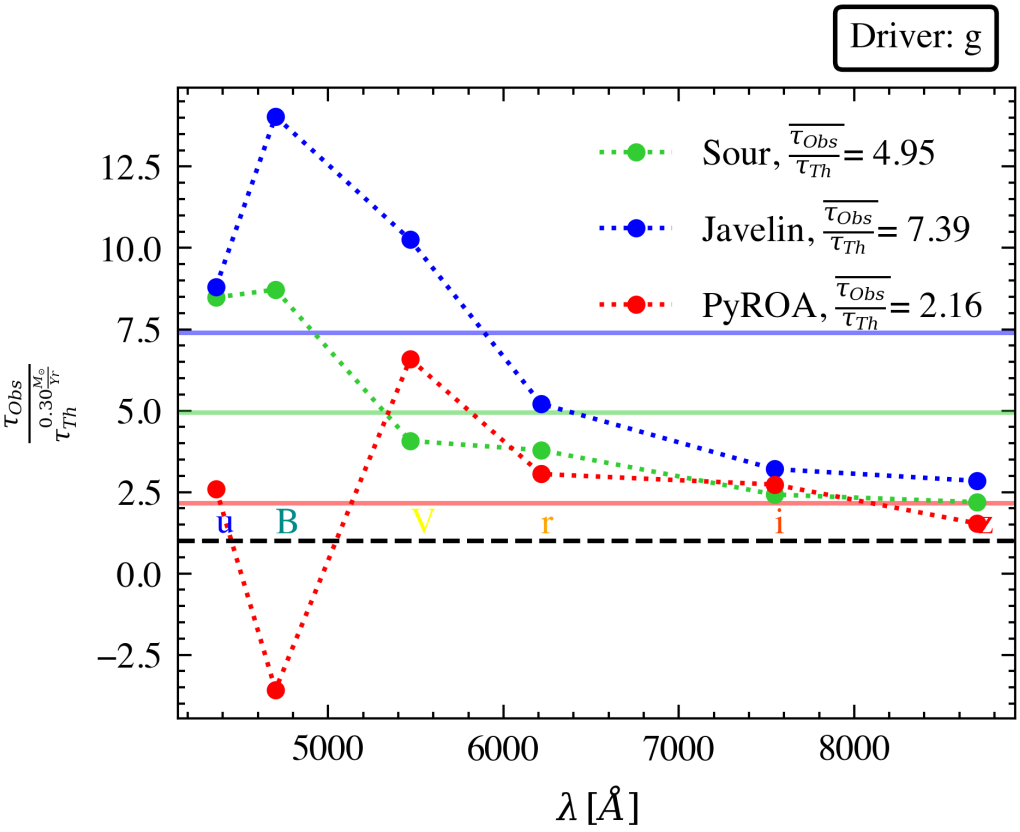

Figure 3.11: Measured lags over theoretical lags relative to the g band for the u, B, V, r, i, z band. Horizontal solid green, blue and red lines are the average difference from the theoretical lags for Sour, Javelin and PyROA respectively.

$$\tau = \tau_\lambda - \tau_{\lambda_0} = \tau_{\lambda_0}\left[\left(\frac{\lambda}{\lambda_0}\right)^\beta - 1\right], \tag{3.1}$$

where τ_{λ_0} is the disc radius at an effective emitting wavelength λ_0. The lag results from all three algorithms (tables 3.5, 3.6, and 3.7), with the u band set as the driver, were plotted against the photometric band centre wavelengths shown as the pink dots in fig. 3.13 - 3.16. Equation 3.1 allows for two possible free parameters τ_{λ_0} and β. Fitting or fixing these parameters allowed for 4 combinations outlined in tables 3.11, 3.12, 3.13, and 3.14. When β was fixed to $\frac{4}{3}$ as expected from a standard thin-disc. Secondly, when τ_{λ_0} was fixed it was estimated from equation 5 in Kokubo (2018). The best-fit errors were derived from the square root of the parameter covariance of the least squares fitting.

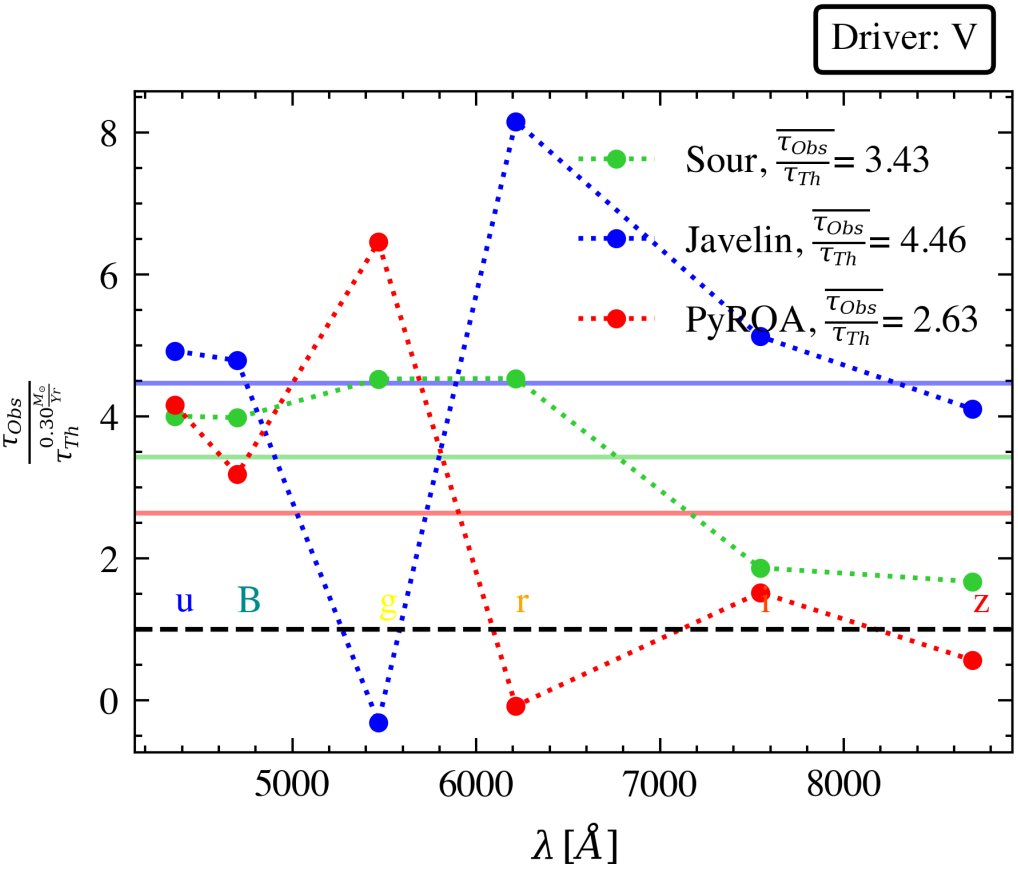

Figure 3.12: Measured lags over theoretical lags relative to the V band for the u, B, g, r, i, z band. Horizontal solid green, blue and red lines are the average difference from the theoretical lags for Sour, Javelin and PyROA respectively.

	β	$\tau_{\lambda_0}[days]$	$\chi^2/d.o.f.$	$d.o.f$
(1)	0.93 ± 0.70	2.50 ± 2.63	1.83	4
(2)	$\mathbf{\frac{4}{3}}$	1.46 ± 0.12	2.23	5
(3)	1.24 ± 0.07	**1.61**	2.13	5
(4)	$\mathbf{\frac{4}{3}}$	**1.61**	1.69	6

Table 3.11: Fit parameters and chi-squared goodness of fit - u band driver. Bold values are fixed, in the case of β it is fixed to $\frac{4}{3}$ for cases (2) and (4). For τ_{λ_0} it is fixed to 1.61 *days* for the u band, calculated from the flux-weighted disc radius (Kokubo, 2018) in cases (1) and (3).

The first fit in fig. 3.13 - 3.16 was produced by limiting $\frac{4}{3} - 0.4 \leq \beta \leq \frac{4}{3} + 0.4$ based on a range of measurements from Edelson et al. (2019) and Hlabathe et al. (2020). Without this limit the fitting algorithm produces an unrealistically large $\tau^u_{\lambda_0} = 11935.34 \pm 1.12 \times 10^7$ *days* and $\beta^u = 0.0 \pm 2.63 \times 10^{-1}$ with a $\chi^2/4 = 0.43$ indicating an over-fitting of the data. Similarly, unrealistic parameters were found when the

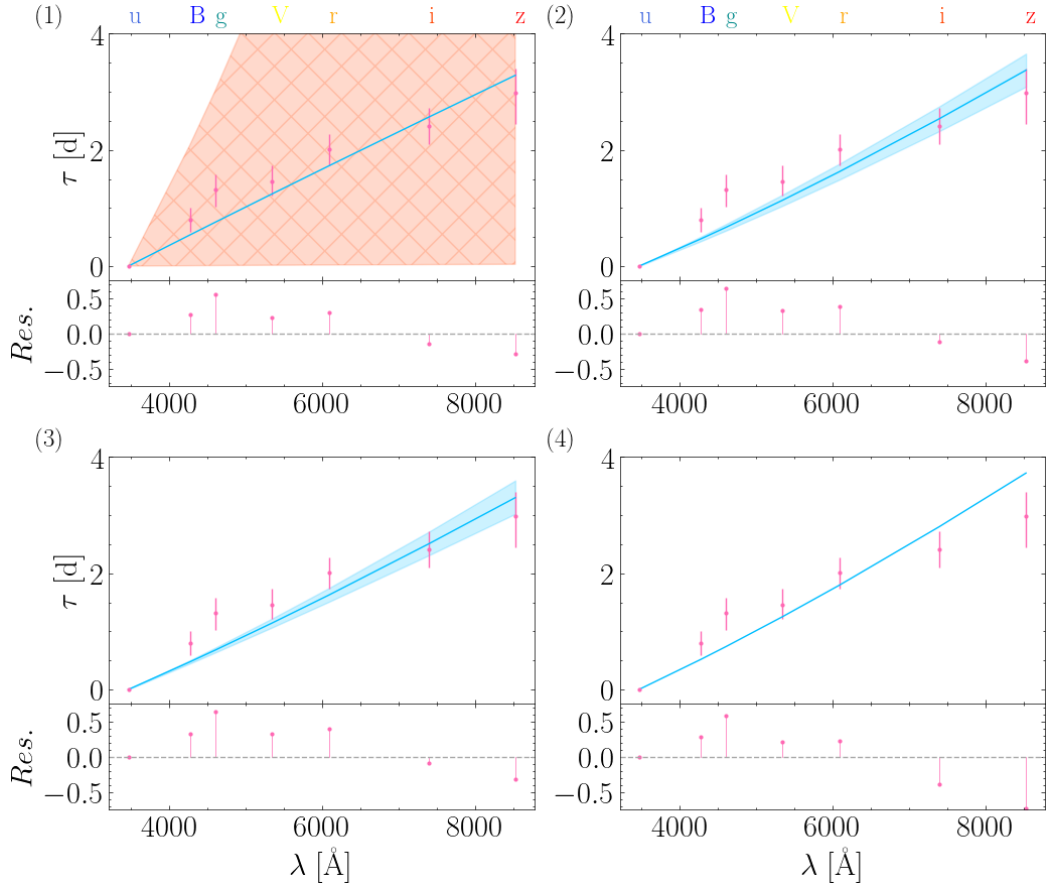

Figure 3.13: $R_\lambda - \lambda$ of the thin-disc expectation compared with the error propagated averages of the Javelin, PyROA, and Sour lags. (1) β and τ_{λ_0} are left as free parameters to be fit. (2) β is fixed at $\frac{4}{3}$ and τ_{λ_0} is left as a free parameter to be fit. (3) β is left as a free parameter and τ_{λ_0} is fixed as in table 3.11. (4) β is fixed at $\frac{4}{3}$ and τ_{λ_0} as in table 3.11. The solid blue line is a power-law best fit of the lag averages. The shaded blue region represents the error-propagated uncertainty overlay for the lag averages at 1σ. The shaded orange cross-hatch error overlay in (1) is indicated differently due to the poorly constrained fit parameters.

driving light curve was set to the B, g, and V bands. Imposing this limit on β results in (1) in tables 3.11 - 3.14 with a more realistic but poorly constrained $\tau^u_{\lambda_0} = 2.50 \pm 2.63\, days$, $\tau^B_{\lambda_0} = 2.32 \pm 5.00\, days$, $\tau^g_{\lambda_0} = 2.26 \pm 5.66$ days, $\tau^V_{\lambda_0} = 3.36 \pm 2.77$ days. These are 0.34σ, 0.04σ, 0.02σ, and 0.18σ respectively away from the theoretical estimates of 1.61 days, 2.12 days, 2.35 days and 2.86 days. And 0.40σ, 0.18σ, 0.02σ, and 0.22σ respectively away from the (2) estimates of $\tau^u_{\lambda_0} = 1.46 \pm 0.12$ days, $\tau^B_{\lambda_0} = 1.40 \pm 0.22$ days, $\tau^g_{\lambda_0} = 1.39 \pm 0.30$ days, and $\tau^V_{\lambda_0} = 2.19 \pm 0.30$ days. The small significances are due to the poorly constrained fit estimates in (1). When β is

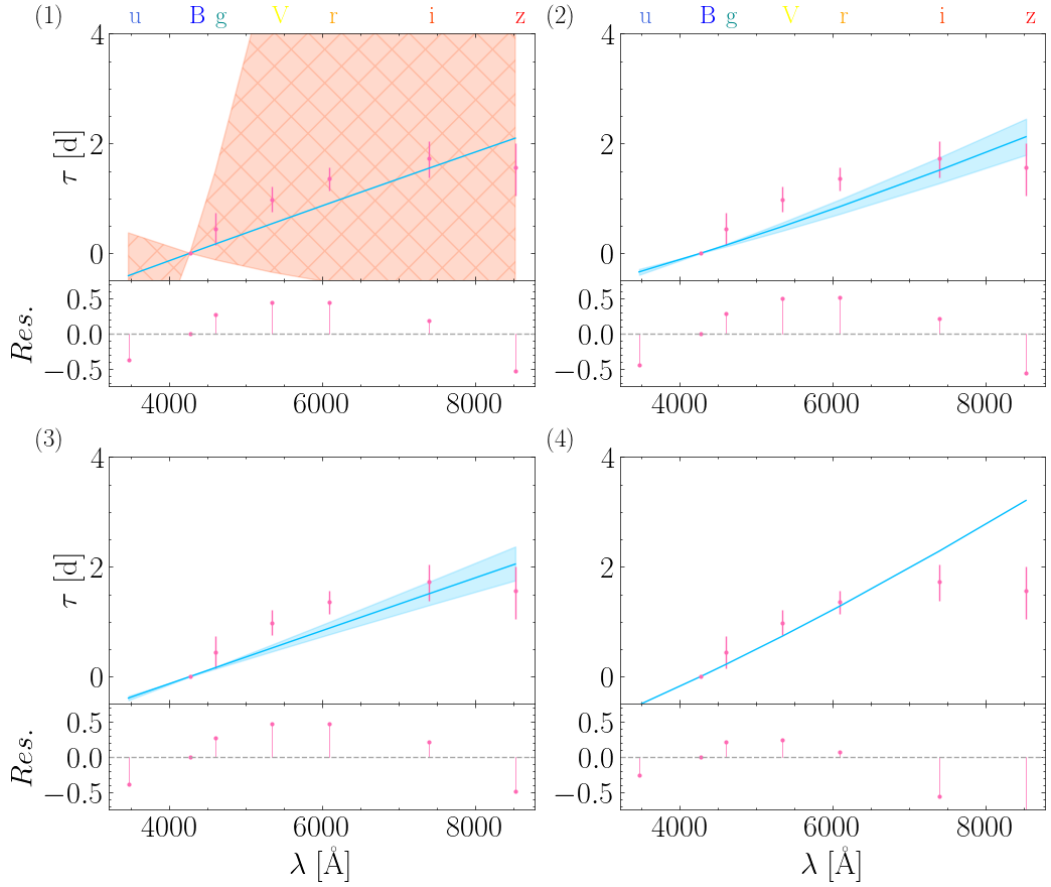

Figure 3.14: $R_\lambda - \lambda$ of the thin-disc expectation compared with the error propagated averages of the Javelin, PyROA, and Sour lags. (1) β and τ_{λ_0} are left as free parameters to be fit. (2) β is fixed at $\frac{4}{3}$ and τ_{λ_0} is left as a free parameter to be fit. (3) β is left as a free parameter and τ_{λ_0} is fixed as in table 3.12. (4) β is fixed at $\frac{4}{3}$ and τ_{λ_0} as in table 3.12. The solid blue line is a power-law best fit of the lag averages. The shaded blue region represents the error-propagated uncertainty overlay for the lag averages at 1σ. The shaded orange cross-hatch error overlay in (1) is indicated differently due to the poorly constrained fit parameters.

fixed to $\frac{4}{3}$, $\tau^u_{\lambda_0} = 1.46 \pm 0.12$ days, and $\tau^B_{\lambda_0} = 1.40 \pm 0.22$ days, $\tau^g_{\lambda_0} = 1.39 \pm 0.30$ days, and $\tau^V_{\lambda_0} = 2.19 \pm 0.30$ days which are 2.50σ, 3.27σ, 3.20σ, and 2.23σ away from and in agreement with the theoretical estimate.

However, when τ_{λ_0} is fixed in (3), β was estimated to be $\beta^u = 1.24 \pm 0.07$, $\beta^B = 0.98 \pm 0.11$, $\beta^g = 0.88 \pm 0.14$, and $\beta^V = 1.04 \pm 0.11$ respectively (tables 3.11, 3.12, 3.13, 3.14) which are 1.56σ, 3.21σ, 3.24σ, and 2.67σ respectively away from the theoretical $\frac{4}{3}$ expectation. And 0.44σ, 0.03σ, 0.03σ, and 0.16σ respectively away from the β estimates in (1) where both β and τ_{λ_0} were left as free parameters.

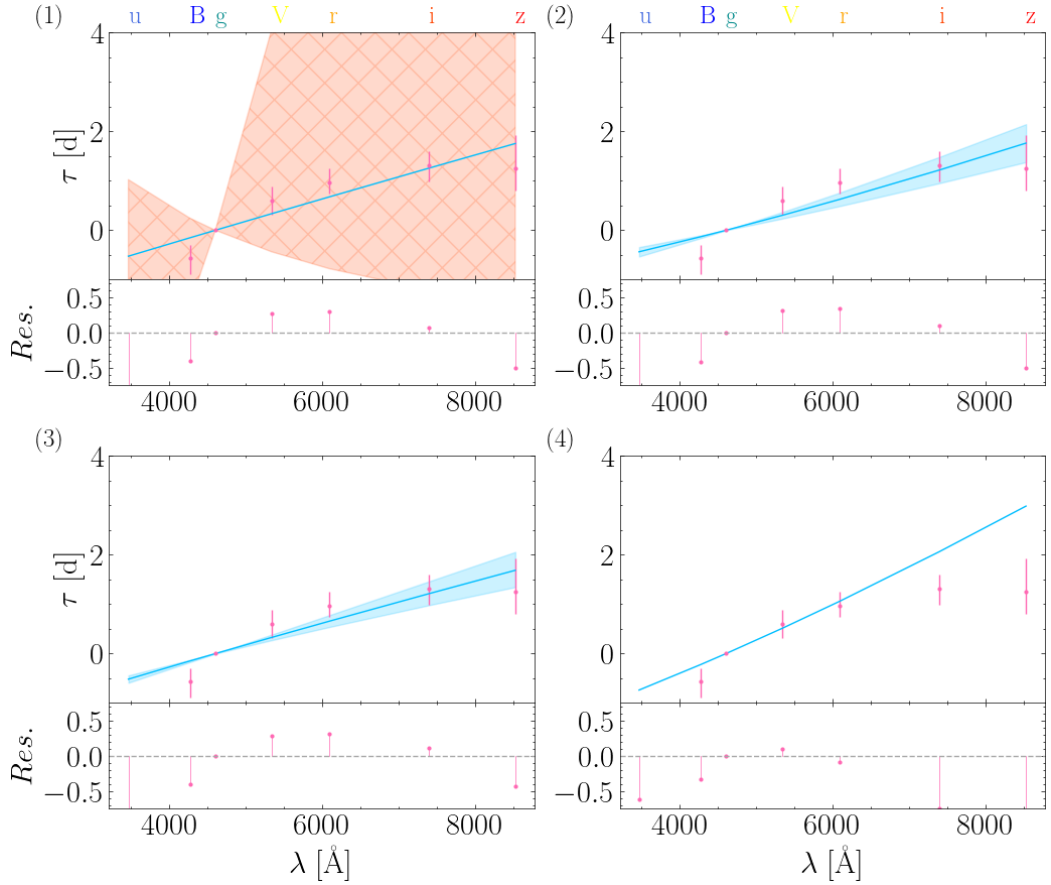

Figure 3.15: $R_\lambda - \lambda$ of the thin-disc expectation compared with the error propagated averages of the Javelin, PyROA, and Sour lags. (1) β and τ_{λ_0} are left as free parameters to be fit. (2) β is fixed at $\frac{4}{3}$ and τ_{λ_0} is left as a free parameter to be fit. (3) β is left as a free parameter and τ_{λ_0} is fixed as in table 3.13. (4) β is fixed at $\frac{4}{3}$ and τ_{λ_0} as in table 3.13. The solid blue line is a power-law best fit of the lag averages. The shaded blue region represents the error-propagated uncertainty overlay for the lag averages at 1σ. The shaded orange cross-hatch error overlay in (1) is indicated differently due to the poorly constrained fit parameters.

The fits in fig. 3.13 either do not fully capture the data, especially for (2) and (3) but less so for (1) and (4). Suggesting that the power law in equation 3.1 is not an appropriate function to fit the data. This seems to be in contrast with Hernández Santisteban et al. (2020).

When the driving light curve is set to the B band, shown in fig. 3.14, the fitting algorithm achieves worse results in (1), (2), and (3) with the $\chi^2/d.o.f.$s all being further away from 1. Indicating that the model is underfitting the data which can be seen by several points being missed out by the fit. The theoretical $\tau^B_{\lambda_0} = 2.12$ days is

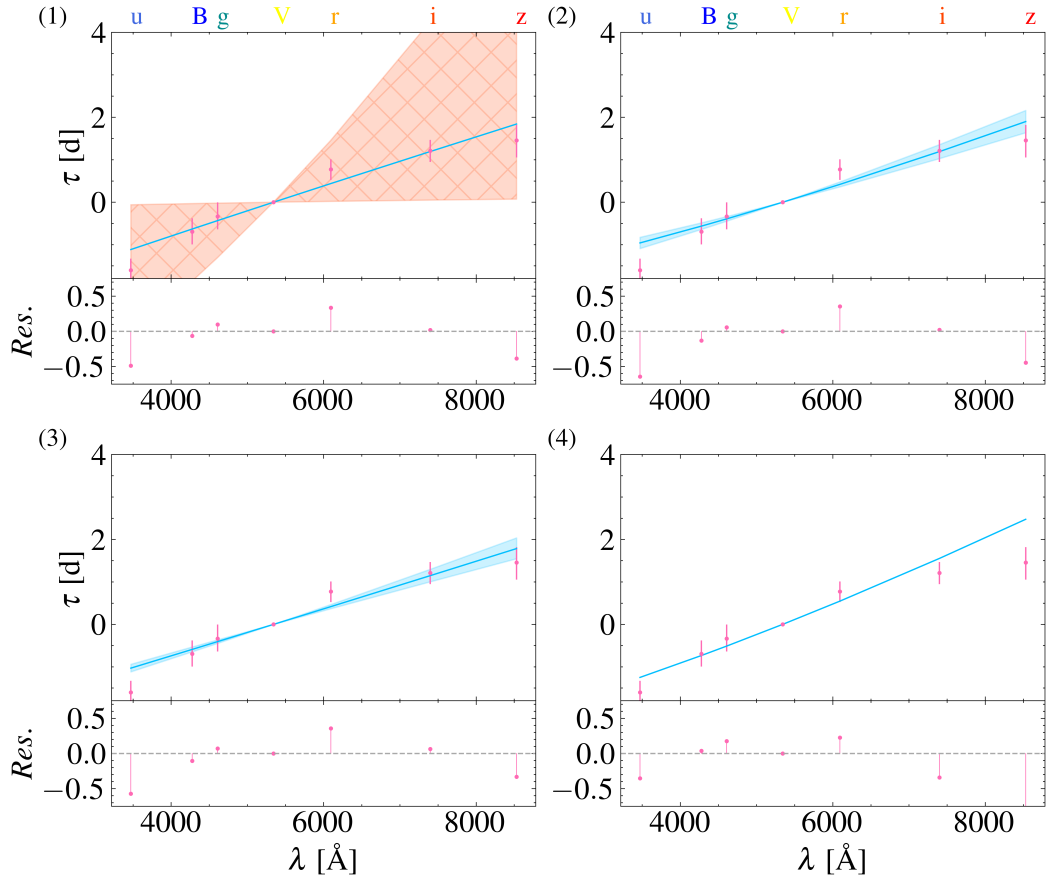

Figure 3.16: $R_\lambda - \lambda$ of the thin-disc expectation compared with the error propagated averages of the Javelin, PyROA, and Sour lags. (1) β and τ_{λ_0} are left as free parameters to be fit. (2) β is fixed at $\frac{4}{3}$ and τ_{λ_0} is left as a free parameter to be fit. (3) β is left as a free parameter and τ_{λ_0} is fixed as in table 3.13. (4) β is fixed at $\frac{4}{3}$ and τ_{λ_0} as in table 3.13. The solid blue line is a power-law best fit of the lag averages. The shaded blue region represents the error-propagated uncertainty overlay for the lag averages at 1σ. The shaded orange cross-hatch error overlay in (1) is indicated differently due to the poorly constrained fit parameters.

expectedly greater than for the u band being the driver at 1.61 days, however, the fit estimates are slightly lower at 2.32 ± 5.00 days for an unfixed β and 1.40 ± 0.22 days for $\beta = \frac{4}{3}$ compared to 2.50 ± 2.63 days and 1.46 ± 0.12 days respectively when the u band is the driver. This trend continues when the g band is set as the driver in table 3.13 such that that $\tau^g_{\lambda_0}$ is lower than both $\tau^u_{\lambda_0}$ and $\tau^B_{\lambda_0}$. This cannot be physical as it suggests that the accretion disc gets smaller with wavelength. A potential explanation could be because the B and g bands have a notable lag excess present, biasing the best-fit line to a smaller magnitude y-axis intercept. Secondly, when

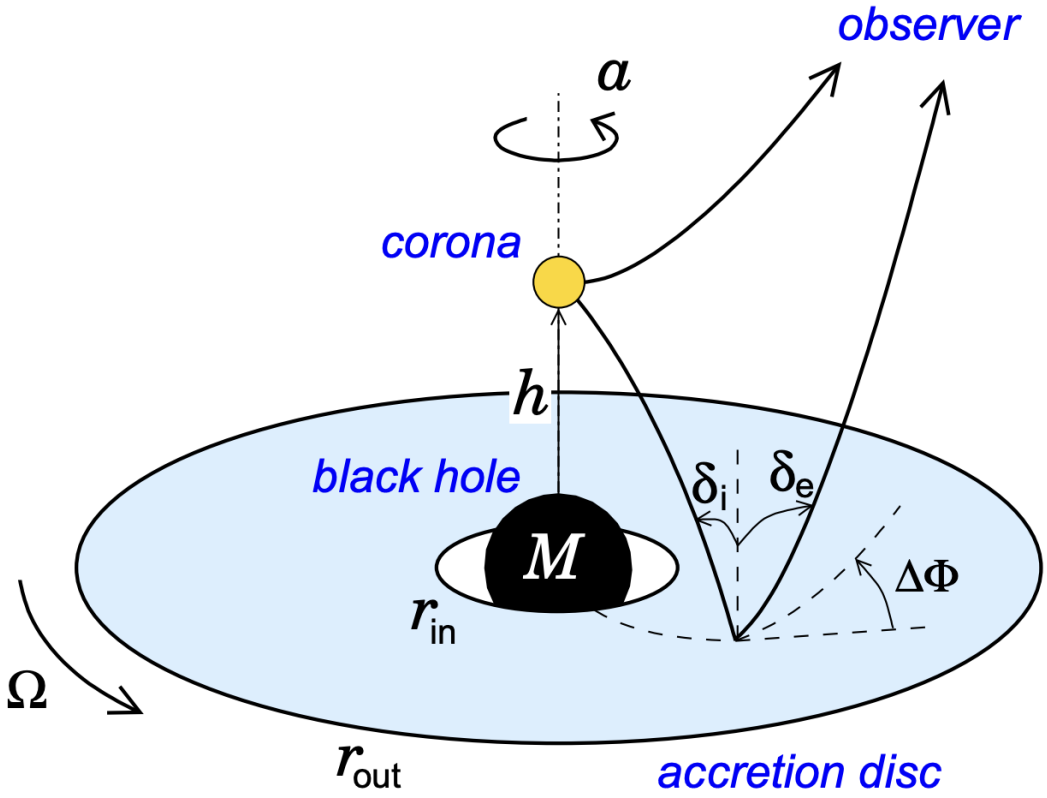

Figure 3.17: Lamp post model geometry with a geometrically thin and optically thick accretion disc being irradiated by a hot corona above the plane of the disc. This image was taken from Dovc˘iak et al.

	β	τ_{λ_0}[days]	$\chi^2/d.o.f.$	$d.o.f$
(1)	0.93 ± 1.55	2.32 ± 5.00	3.16	4
(2)	$\mathbf{\frac{4}{3}}$	1.40 ± 0.22	3.22	5
(3)	0.98 ± 0.11	**2.12**	2.75	5
(4)	$\mathbf{\frac{4}{3}}$	**2.12**	2.68	6

Table 3.12: Fit parameters and chi-squared goodness of fit - B band driver. Bold values are fixed, in the case of β it is fixed to $\frac{4}{3}$ for cases (2) and (4). For τ_{λ_0} it is fixed to 2.12 days for the u band, calculated from the flux-weighted disc radius (Kokubo, 2018) in cases (1) and (3).

looking at $\tau^V_{\lambda_0}$ in table 3.14, both (1) and (2) are greater than their respective values in table 3.11.

It is notable that the fits when the V band is set as the driving light curve are better than when the driving light curve is the B and g bands as the $\chi^2/d.o.f.$ values are closer to 1. The fits in fig. 3.14 and 3.15 do not fully capture the data, as the $\chi^2/d.o.f.$ values are greater than 2. Suggesting that the power law in equation 3.1

	β	$\tau_{\lambda_0}[days]$	$\chi^2/d.o.f.$	$d.o.f$
(1)	0.93 ± 1.86	2.26 ± 5.66	2.75	4
(2)	$\mathbf{\frac{4}{3}}$	1.39 ± 0.30	2.77	5
(3)	0.88 ± 0.14	**2.35**	2.33	5
(4)	$\mathbf{\frac{4}{3}}$	**2.35**	2.84	6

Table 3.13: Fit parameters and chi-squared goodness of fit - g band driver. Bold values are fixed, in the case of β it is fixed to $\frac{4}{3}$ for cases (2) and (4). For τ_{λ_0} it is fixed to 2.35 days for the u band, calculated from the flux-weighted disc radius (Kokubo, 2018) in cases (1) and (3).

	β	τ_{λ_0}[days]	$\chi^2/d.o.f.$	$d.o.f$
(1)	0.93 ± 0.69	3.36 ± 2.77	1.34	4
(2)	$\mathbf{\frac{4}{3}}$	2.19 ± 0.30	1.55	5
(3)	1.04 ± 0.11	**2.86**	1.27	5
(4)	$\mathbf{\frac{4}{3}}$	**2.86**	1.75	6

Table 3.14: Fit parameters and chi-squared goodness of fit - V band driver. Bold values are fixed, in the case of β it is fixed to $\frac{4}{3}$ for cases (2) and (4). For τ_{λ_0} it is fixed to 2.86 days for the u band, calculated from the flux-weighted disc radius (Kokubo, 2018) in cases (1) and (3).

is not an appropriate function to fit the data. This points to the contribution of the BEL contamination in both the B and g bands suggesting also that $\tau^B_{\lambda_0}$ and $\tau^g_{\lambda_0}$ are poor physical representations of light travel time.

3.5.2 Fractional Variability

$Filter$	F_{var}
u	0.024 ± 0.00036
B	0.025 ± 0.00027
g	0.021 ± 0.00027
V	0.020 ± 0.00031
r	0.017 ± 0.00036
i	0.019 ± 0.00037
z	0.024 ± 0.00041

Table 3.15: Fractional variability calculated using the procedure outlined by Fausnaugh et al. (2016). The uncertainties were calculated through error propagation and are shown for reference but they are effectively 0.000 given that they are all 2 orders of magnitude smaller than the estimated value.

The fractional variability (F_{var}) is a measure of the degree of variability of a light curve. F_{var} as a function of wavelength was calculated according to the procedure

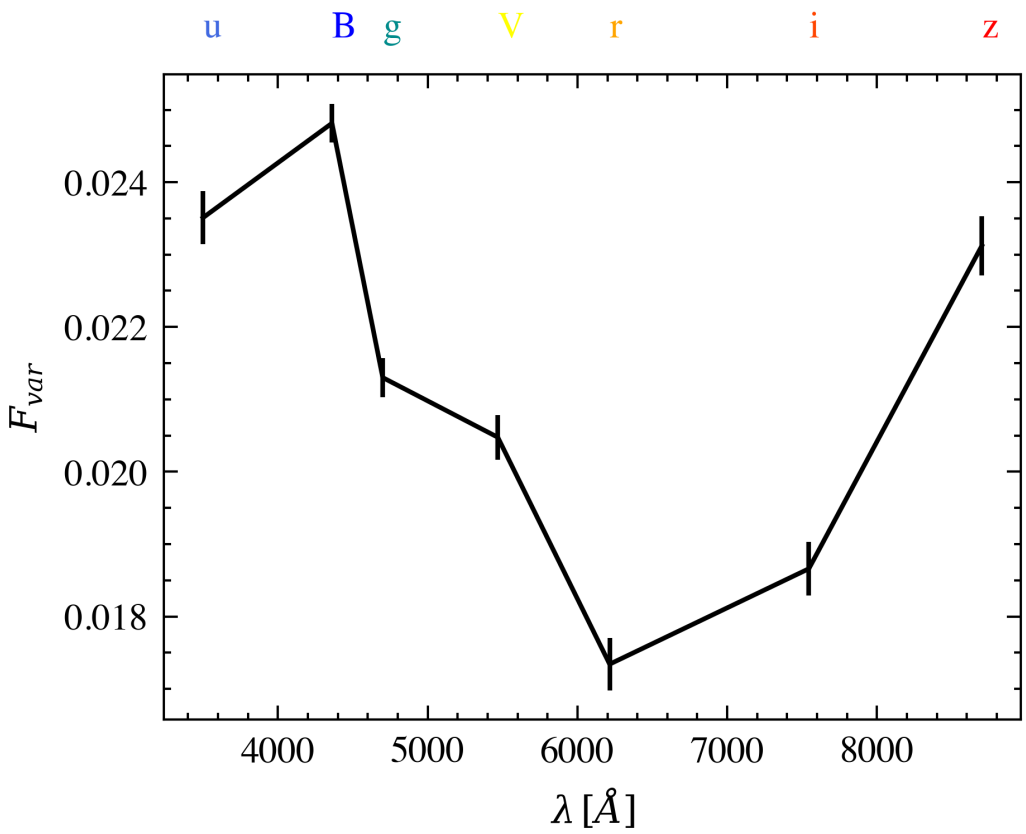

Figure 3.18: Fractional variability as a function of wavelength, in angstroms, with the band centres plotted above the plot in multi-colour.

outlined by Fausnaugh et al. (2016) and is shown in fig. 3.18. It was found that F_{var} steadily decreases from the B band to the r' band this is to be expected due to the increasing contribution of the underlying host galaxy, whose non-varying spectrum is redder than that of the varying AGN and dilutes the variability from the AGN. Interestingly, from the r' band to the z_s band F_{var} increases quite significantly. This might suggest strong dust extinction present in the g', V, r', and i' bands.

3.5.3 Spectral analysis

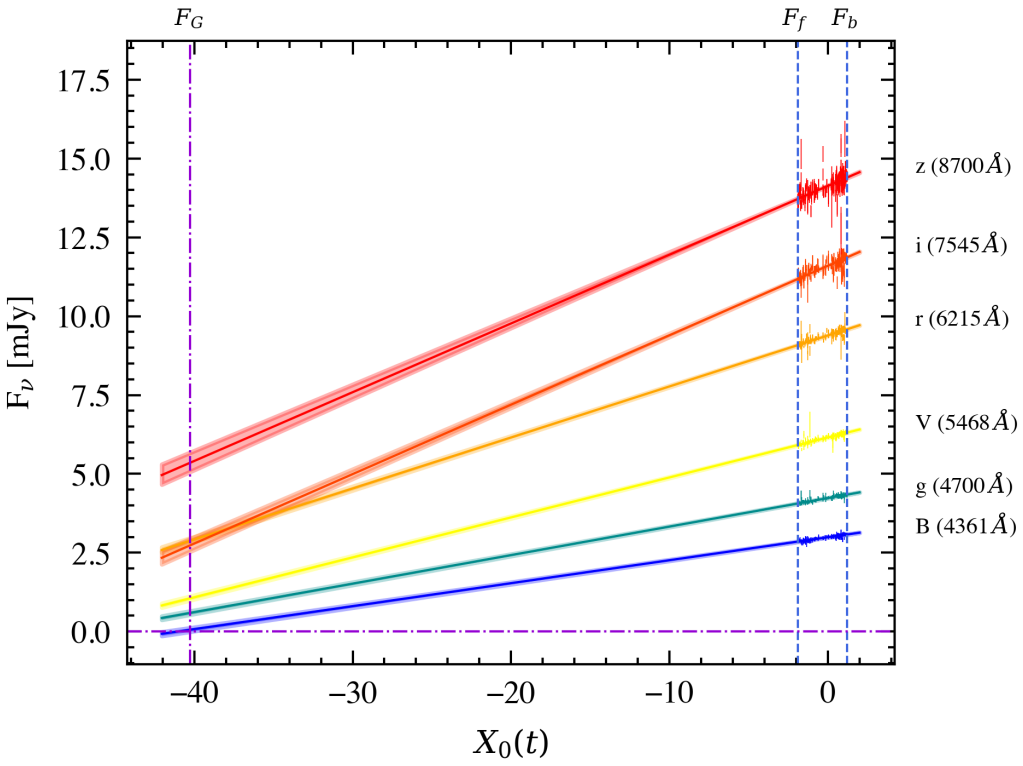

Figure 3.19: PyROA implementation of the Flux-Flux analysis, code taken mostly from J. Hernandez with some adaptations. U band is taken as the driver normalised, and plotted on the x-axis. The purple dot-dash lines (F_G) indicate a lower limit estimate of contamination from the host galaxy, the BLR, and the y-axis zero value. The blue dashed lines (F_f and F_b) indicate the bright and faint values of the driver (u band) over the campaign.

Filter	$\overline{F}$ $[mJy]$	Host Galaxy $[mJy]$	$F_b - F_f$ $[mJy]$	$\frac{RMS}{F_b - F_f}$ %	$\frac{RMS}{Mean}$ %	$F_b - F_f$ $[mJy]$ (Corrected)
B (4361 Å)	3.82 ± 0.001	0.07 ± 0.057	0.29 ± 0.004	32.347%	2.4361%	2.02 ± 0.027
g' (4700 Å)	4.66 ± 0.091	0.74 ± 0.071	0.35 ± 0.128	32.350%	2.4354%	2.03 ± 0.739
V (5448 Å)	6.26 ± 0.116	1.26 ± 0.100	0.47 ± 0.164	32.346%	2.4352%	1.94 ± 0.674
r' (6215 Å)	7.76 ± 0.152	3.36 ± 0.127	0.58 ± 0.214	32.351%	2.4355%	1.91 ± 0.700
i' (7545 Å)	10.14 ± 0.257	3.06 ± 0.173	0.76 ± 0.362	32.347%	2.4352%	1.92 ± 0.908
zs (8700 Å)	9.80 ± 0.370	5.86 ± 0.172	0.74 ± 0.520	32.353%	2.4356%	1.45 ± 1.018

Table 3.16: Reconstructed spectrum of the mean flux $\bar{F}$, constant host galaxy component, and variable bright minus faint $F_b - F_f$ component by decomposing the photometry flux assuming a linear driving relation equation 3.2. The last three columns also show the RMS spectrum as a fraction of the bright minus faint and the mean flux spectra; and the unreddened bright minus faint component that accounts for extinction. The RMS fractions in the penultimate two columns have been shown with more than necessary significant figures to demonstrate a difference but they are all consistent with 32.35% and 2.44%.

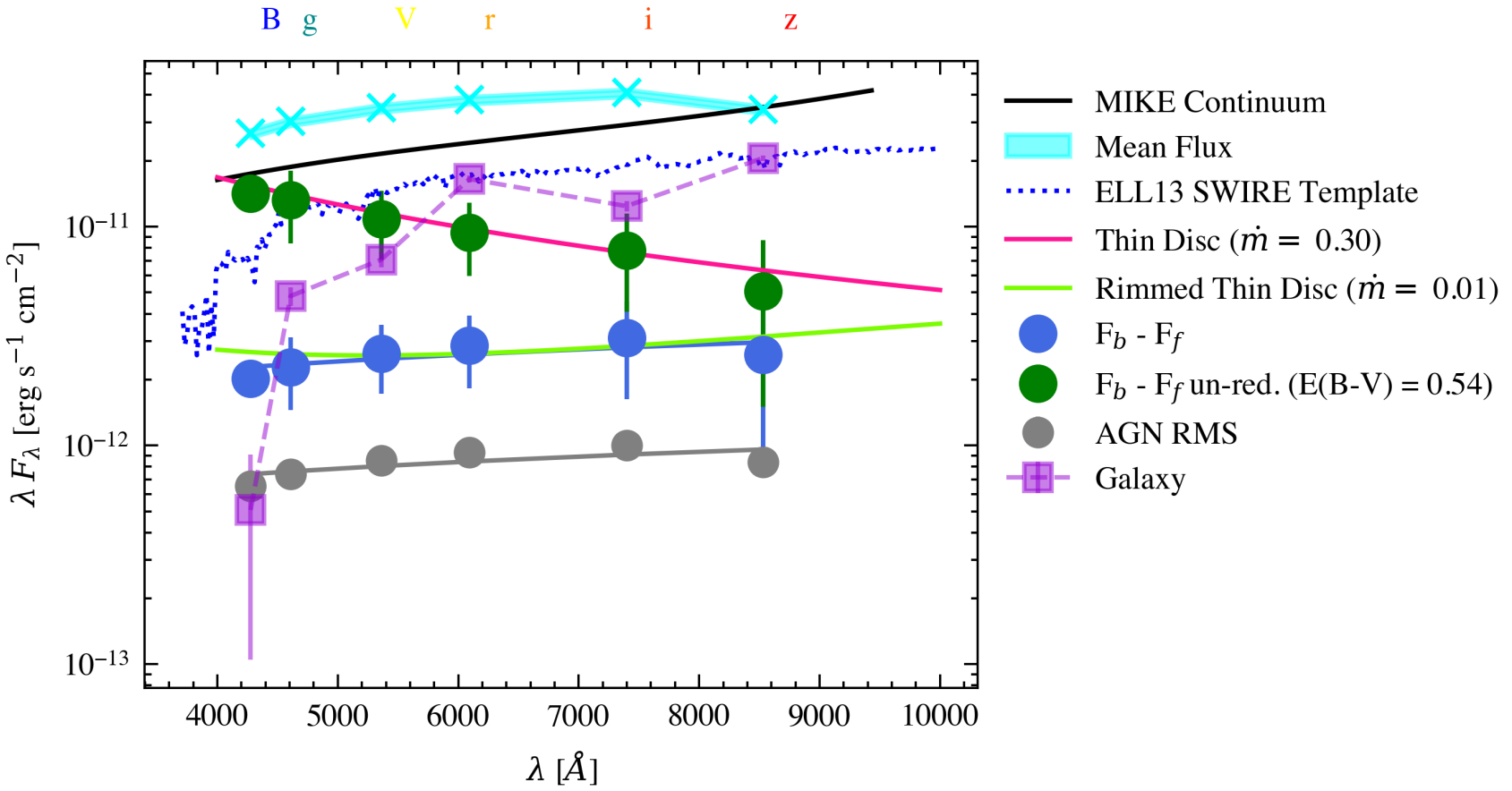

Figure 3.20: Spectral energy distribution in the rest frame of the bright-faint (blue), RMS (grey) component, and the AGN constant component (purple). The cyan line is the AGN mean flux and the pink line is the thin-disc power law expectation for an Eddington ratio of 0.3 that is obtained from a value of 14 % of $L_{Bol} = 2.5 \times 10^{45}\,\mathrm{erg\,s^{-1}}$ (Pan et al., 2021). The dotted blue line is the elliptical (13 Gyr) SWIRE template (Polletta et al., 2007) scaled to match the flux from the z_s band galaxy component in purple. Lime-green points indicate the un-reddened $F_b - F_f$ variable component accounting for an internal extinction of $E(B-V) = 1.6$.

The reprocessing model assumes that the variability in the lagged light curves linearly responds to the driver light curve, to test this, the fluxes of the lagged light curves can be plotted against the driving light curve flux ($X_0(t)$), which is normalised so that $\langle X_0 \rangle = 1$ and $\overline{X_0} = 0$. Alternatively, the lagged light curves are scaled and shifted versions of the driving light curve (taken from Hernández Santisteban et al. (2020));

$$F(\lambda) = C(\lambda) + S(\lambda)X(t). \tag{3.2}$$

Given a time at which there is driving light curve flux measurement the flux measurements in the lagged light curves at that time are assumed to be a linear combination of $C(\lambda)$ and $S(\lambda)$. $C(\lambda)$ and $S(\lambda)$ are functions of wavelength because they will vary with each lagged light curve. $C(\lambda)$ is a constant for each light curve and $S(\lambda)$ can be understood as the RMS (root-mean-square) spectra Cackett et al. (2020). Furthermore, contamination of the photometric bands from the host galaxy and diffuse continuum emission from the BLR can be estimated by extrapolating the linear model of the first band that crosses $F_\nu = 0$ (fig. 3.19). Then the non-varying contamination spectrum can be estimated by taking a vertical line F_G (dot-dashed lines in fig. 3.19) at the crossing point. Furthermore, fig. 3.19 and 3.20 also show that the maximum and minimum AGN spectra can be evaluated by taking vertical lines at the faintest and brightest driving light curve fluxes (shown by F_f and F_b). Fig. 3.19 and 3.20 illustrate that a linear response model fits well within the span of the observations which can be then extrapolated to estimate the extent of flux contamination.

Fig. 3.19 was produced by adapting the flux-flux analysis code published as an extension to the PyROA package. PyROA outputs MCMC samples of the $C(\lambda)$ and $S(\lambda)$ parameters directly which enabled each light curve to easily fit with the error overlay to be estimated from the 1σ bounds of the MCMC samples. Since Javelin utilises a different model to optimise the DRW parameters for the lagged

light curves to be scaled and reprocessed versions of the driver, it was necessary to manually fit each light curve against the normalised driver and using the least squares uncertainty to produce the error overlay. This ensures that F_G, F_f, and F_b are comparable to fig. 3.19. $F_b - F_f$ can be understood as the total amount of variable flux while AGN RMS flux is the amount that $F_b - F_f$ varies in units of flux. $F_b - F_f$ then is a measure of variability.

Before constructing the spectral energy distribution in fig. 3.20, all the flux values obtained from photometry were un-redden to account for dust in the Milky Way using the Fitzpatrick (1999) and a dust extinction of $E\,(B-V) = 0.064$ (Schlafly and Finkbeiner, 2011) before being shifted to the rest-frame. For consistency, fig. 3.20 overlays the continuum extracted from the MIKE spectrum from 6 wavelength bins over the range 4499Å – 8600Å selected to avoid emission lines and instrument noise. The spectral shape agrees with the mean flux from photometry and completely agrees with the z_s band.

Unexpectedly, the $F_b - F_f$ is flat across the photometric bands. The expectation is that emissions from shorter wavelength bands originate closer to the central black hole and their variability is driven more strongly. Secondly, shorter wavelength bands are expected to be less contaminated by host galaxy starlight that peaks in the red optical and NIR wavelengths. The variable component of flux should be strongest at the shorter wavelength bands; the flat $F_b - F_f$ spectrum motivates an investigation into whether reddening causes the observed flux deficit. Pan et al. (2021)'s analysis of the UV-optical-IR spectral energy distribution found a direct and transmitted component that is heavily obscured ($E(B-V) \approx 1.6$) and another indirect and scattered component with mild extinction ($E(B-V) \approx 0.5$). The effect of reddening can be seen in fig. 3.20 with the elliptical $13\,Gyr$ host galaxy SWIRE template being greater than the galaxy component extracted from the photometric bands for the shortest bands. The transmitted component was accounted for by un-reddening using a Small Magellanic Cloud (SMC) extinction curve resulting in the green $F_b - F_f$ points in fig. 3.20. The amount of variability after un-reddening

is then much closer to a disc shape. The thin-disc model in fig. 3.20 can then be qualitatively aligned to find an estimate of the Eddington ratio, $\dot{m} = 0.3$. This corresponding to 14 % of $L_{Bol} = 2.5 \times 10^{45}\,\mathrm{erg\,s^{-1}}$.

3.6 Discussion

3.6.1 Accretion disc size

The lag spectra are fit by a power law $\tau(\lambda) = \lambda^{\beta}$ ($\beta = \frac{4}{3}$ for a thin disc) when the V band is set as the driving light curve and when β and τ_{λ_0} are left free (table 3.14). However, this fit is poorly constrained, $\tau_{\lambda_0} = 3.66 \pm 2.64$ days and $\beta = 0.93 \pm 0.60$, and results in τ_{λ_0} estimate that is larger than the theoretical estimate from flux weighted thin disc by a factor of 6 (Kokubo, 2018; Mudd et al., 2018; Fausnaugh et al., 2016; Cackett et al., 2007) and by a factor of 10 by estimating the accretion rate from the $F_b - F_f$ fluxes. The fit is well constrained when β is fixed at $\beta = \frac{4}{3}$ as in (2) of fig. 3.16, with $\tau_{\lambda_0} = 2.38 \pm 0.30$ days. Which is a factor of 3 larger than the theoretical estimate from a flux-weighted thin disc and a factor of 7 larger than from the $F_b - F_f$ fluxes. Despite the enlarged disc size estimates (at the reference wavelength), the lags are consistent with a $\tau_{\lambda_0} \propto \lambda^{\frac{4}{3}}$ power law. Although the Javelin lags (table 3.5) are mostly consistent with PyROA and Sour, the fits in figure 3.3 fail to reproduce peak-to-peak amplitudes in the u and i' band which, on its own, rules it out as a viable algorithm.

The measured accretion disc sizes, after accounting for extinction, indicate inconsistency with predicted lags by a factor of $3 - 4$ on average depending on the algorithm. Some of the discrepancies between Javelin, PyROA and Sour are very large given the uncertainties they claim thus some lags are inconsistent with each other (for example the V-r lags in figure 3.8). Therefore, more work needs to be done to understand the systematic errors between the three algorithms before thin discs can be ruled out for certain. Figure 3.9 demonstrates this with the observed

lags scaled by the expected timescales so that the y-axis shows the multiples of difference from the expectation. The expected lags are the theoretical lags implied by the thin disc temperature profile in equation 1.6 with an accretion rate corresponding to 14% of L_{Bol} from Pan et al. (2021) which is $\dot{m} = 0.3$ (see table 3.4. Measured lags a factor of a few larger were expected and have been regularly seen, for example, Fian et al. (2023); Hlabathe et al. (2020); Fausnaugh et al. (2016). However, figure 1 of Sun and Malkan (1989) relativistic corrections might be large enough to account for the discrepancy between the expected and measured lags and figure 2 shows how little of the disc spectrum can be described by the $L_\nu \propto \nu^{\frac{1}{3}}$ relationship, and a huge effect of disc inclination which is in contradiction to the convention and idealisation we use in this thesis - summarised by figure 1.2. Therefore, it is likely that equation 1.5 is an oversimplification, especially for a rapidly spinning black hole, and equation 1.6 is incorrect for the disc regions that produce blue light. Despite this, there may be indications of diffuse continuum emission from the BLR (observed by Hernández Santisteban et al. (2020) for Fairall 9), indicated by deviations in the lag spectra from the best-fit line in the B, g', and r' bands (fig. 3.5) corresponding to BLR contaminant line fluxes (table 3.3 and figure 3.1). Using an MCMC procedure model, Hernández Santisteban et al. (2020) finds model parameters for a mixing of the DCE lag contribution (scaled from NGC 5548 accounting for relative luminosity Korista and Goad (2019)) and disc lag components. A similar analysis for Mrk 1239 may account for the enhanced lags and show a better fit to a thin disc model. As discussed in section 3.6, Cackett et al. (2022) developed a frequency-resolved accretion disc lag model that showed that for NGC 5548 the lags are more consistent with a standard-sized accretion disc with a BLR emission when compared to a larger-than-expected disc. A similar analysis should be done with Mrk 1239 to investigate the factor of $\sim 3-4$ difference between expected and observed disc sizes.

3.6.2 Flux-flux analysis

The unexpected shape of the fractional variability spectrum in fig. 3.18 motivated the investigation of the origin of the light curve variability using the Flux-Flux method (Starkey et al., 2017). The strong linear relationships between the faint and bright states in fig. 3.19 imply a constant flux distribution thus validating the linearised RM assumptions used by Javelin and PyROA. That is, each light curve is linearly related to the (hypothetical) driving light curve Starkey et al. (2017) using a variable and constant component; allowing for a decomposition of the photometry.

The corresponding spectral reconstruction in fig. 3.20 of the $F_b - F_f$ component does not match the spectral shape expected shape for a thin disc and the Eddington ratio from Pan et al. (2021) is $\dot{m} \approx 2$. Rodríguez-Ardila and Mazzalay (2006); Pan et al. (2021) propose and observe evidence for a dusty torus, accounting for this may resolve the spectral shape of the variable component with that of a thin disc. Although a dusty torus is only one potential explanation, the roughly flat spectral shape heavily implies that dust reddens the original disc emission.

3.6.3 Unreddening

The spectral shape is resolved to the expected $\lambda \propto \nu^{\frac{1}{3}}$ shape by applying an extinction based on an SMC extinction curve of $E(B-V) = 0.54$ (Rodríguez-Ardila and Mazzalay, 2006; Pan et al., 2021) to the $F_b - F_f$ fluxes accounting for dust in a torus located between the narrow line region and the broad line region. Fitting the thin accretion disc model to the un-reddened fluxes in fig. 3.20 corresponds to an Eddington ratio of $\dot{m} = 0.28$ or 14% of L_{Bol} from Pan et al. (2021). However, accounting for reddening does not resolve the disc size tension, measured disc radii are still $\sim 3 - 4\times$ the expected size (fig. 3.9).

The intercepts of the best-fitting linear relations in fig. 3.19 were used to derive the constant host galaxy spectrum in fig. 3.20. This is compared to an elliptical SWIRE

template with significant discrepancies observed at the B-band. Testing ruled out reddening as an explanation for the discrepancy and the cause of reddening on the variable component isolated to the disc emission.

It is also important to note that estimates at several wavelengths of the MIKE continuum flux in fig. 3.20 match the order of magnitude as the extinction-free template used in the SED composition by Pan et al. (2021).

For the standard thin disc model, the lag spectrum is constrained such that $\tau \propto \lambda^{\frac{4}{3}}$ and the expected disc SED to $F_\nu \propto \lambda^{-\frac{1}{3}}$. Starkey et al. (2023) seeks to tackle these constraints by demonstrating the effects of semi-analytic models with a finite disc thickness profile, $H(r)$. It is motivated by a desire to reconcile lag spectra implying high Eddington ratios and SED fits implying the opposite (please see fig. in Starkey et al. (2023)) by adjusting the disc shape, reducing the fraction of disc surface exposed to lamp post-irradiation while simultaneously increasing the temperature at the outer disc regions. A similar reconciliation of the time lags and a thin accretion disc was identified by Meeting and Bertout (1991) due to reprocessing in the outer parts of the thin accretion disc that can dominate the optical continuum. The Starkey et al. (2023) rimmed-disc model was fitted to the reddened, untreated, $F_b - F_f$ fluxes to test whether it could be an alternative to dust extinction. The rimmed-disc model is a finitely thick disc defined by an exponentially increasing disc thickness modelled as a power law. The case of a concave disc (power-law greater than 1) should increase irradiation for the outer disc by tilting it towards the central regions thereby increasing the disc temperature in the outer regions and allowing for inflated disc lags. Fig. 3.20 shows a rimmed disc with a height of $0.01\,\mathrm{light-days}$ at $\sim 1\,\mathrm{light-day}$ disc radius. The rimmed disc cannot match the spectral shape of the $F_b - F_f$ fluxes without a discrepancy at the B band and unreasonable model parameters. An Eddington ratio of $\dot{m} = 0.01$, a disc height of $\sim 20 - 25\,\mathrm{light-days}$ (at $\sim 1\,\mathrm{light-day}$ from the centre), and an inner disc radius less than the innermost stable circular orbit is required to fit the reddened $F_b - F_f$ fluxes. Furthermore, the implied theoretical disc sizes from the rimmed disc fit to

the reddened $F_b - F_f$ fluxes are a factor of $\sim 5-6$ smaller than the observed lags, making the disagreement worse when compared to a thin disc.

3.6.4 Obscuration

Table 3.3 shows the estimated flux from BELs (Balmer series) within the photometric bands which may be connected to the deviations of the B, g‘, and r‘ bands from the lag spectrum best fits in fig. 3.13, 3.14, 3.15, and 3.16. However, a stringent analysis has not been conducted to investigate the origin of the deviations from the best fits and for whether Mrk 1239 shows evidence of a flux excess. A lag excess may result from a flux excess around the Balmer break (3654 Å), which could introduce longer timescales of variability has been observed for several AGN (Edelson et al., 2015, 2017, 2019; Fausnaugh et al., 2016; Cackett et al., 2020; Hernández Santisteban et al., 2020). However, some AGN show no obvious lag excess in their lag spectra, such as Mrk 817 in Kara et al. (2021). The origin of the Balmer excess is also disputed and Mrk 1239 could be a good candidate to test the BLR origin proposed by Edelson et al. (2019) and the ionised obscurer origin proposed by Kara et al. (2021).

Kara et al. (2021) detect new narrow and broad UV absorption lines and depression of soft X-rays relative to a spectrum from 2009 (Winter et al., 2011) which they say implies the existence of a dust-free ionised wind acting as an obscurer inwards of the BLR. They also find that the optical Hβ emission line lags the optical continuum by 23 days, similar to previous Hβ RM campaigns, however, for the first 55 days of the campaigns the Lyα and C IV BELs from the BLR showed little correlation with the UV continuum but as the obscuration in the X-rays appeared to decrease, the next 42 days showed a consistent lag of around $2-3$ days, on the same timescale as accretion disc variability. An interesting connection is made by Neustadt et al. (2023), where to test the lamp post reverberation model (Krolik et al., 1991) they fit the UV/Optical light curves for Mrk 817 to produce maps of the temperature fluctuations of the accretion disc in time and radius. They find

that a significant component of the disc temperature variability is driven intrinsically and not through reverberation and they separated long-timescale variability intrinsically from the disc from reverberation by detrending the light curves. Furthermore, the residuals of unmodified light curves (relative to a lamp post-RM modelled light curves) for both Mrk 817 and NGC 5548 were consistent with a lag of around 0 days with Javelin.

A possible explanation could be that these residuals are a result of reprocessing by the mildly ionised clouds obscuring the disc proposed by Kara et al. (2021) because of its close proximity to the disc (see fig. 1 of Kara et al. (2021)). Anomalously broad Balmer emission lines should be expected if this obscurer contributes significant Balmer continuum flux but this is not seen and lag excesses in the U and u bands disappear after detrending (Cackett et al., 2023) suggesting that the lag excess originated from a long timescale variability such as the BLR. Interestingly, the lag excess does not disappear for NGC 5548 (Fausnaugh et al., 2016) despite Neustadt et al. (2023) finding that the residuals were consistent with a near 0 day lag. This could be a result of the second-order polynomial and running Gaussian average detrending methods used for NGC 5548 and Mrk 1239 respectively. Neustadt et al. (2023)'s disc model cannot reproduce a flux excess localised in wavelength because of the large overlap in disc radii that contribute to the emission in each band. Therefore, a BLR origin for this lag excess is possible for Mrk 817 and NGC 5548. Although Mrk 1239 is a NLS1 AGN with evidence of heavy dust obscuration, it has a luminosity of $L_{Bol} = 2.5 \times 10^{45}\,\mathrm{erg\,s^{-1}}$ (far larger than typical type 2 AGN luminosities of $5 \times 10^{44}\,\mathrm{erg\,s^{-1}}$). In comparison, type 1 Seyferts Mrk 817 and NGC 5548 have bolometric luminosities of $9.2 \times 10^{44}\,\mathrm{erg\,s^{-1}}$ (Miller et al., 2021) and $4.0 \times 10^{44}\,\mathrm{erg\,s^{-1}}$ (Landt et al., 2019) respectively.

The dip in the X-rays at $\sim 2\,\mathrm{keV}$ for Mrk 817 seen by Kara et al. (2021) that motivated the outflowing and X-ray obscuring ionised clouds is seen in Mrk 1239 (fig. 3.21). The right plot in fig. 3.21 also shows how the soft X-rays have changed over many years corresponding to a change of a factor of ~ 10 from 2009 to 2021.

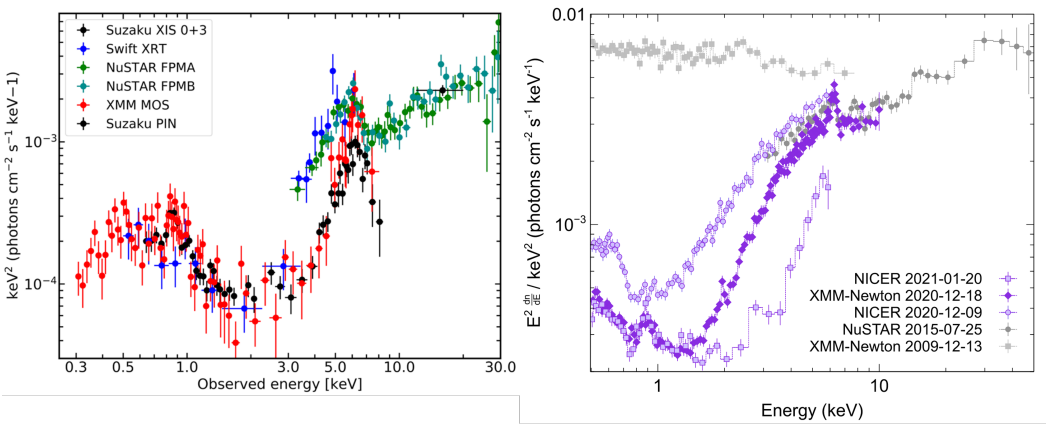

Figure 3.21: X-ray spectra for Mrk 1239 (left, Buhariwalla et al. (2020)) and Mrk 817 (right, Kara et al. (2021)) with the dip in the soft X-rays at $\sim 2\,\mathrm{keV}$.

This indicates that a similar structure could be present in Mrk 1239. If these clouds are extended enough they could account for BLR continuum emission and extinction in optical wavelengths. The presence of dust would be determined by the temperature of the material, with dust forming at $\sim 1500\,\mathrm{K}$ for pure silicate dust and $\sim 2000\,\mathrm{K}$ for pure graphite dust. The temperature is regulated by the material's opacity and the emission from the AGN's central regions, as well as the extent to which the emission is isotropic. Jiang (2023) recently discusses the obscured soft X-rays in Mrk 1239 connecting it to the existence of radiation-driven dusty winds enabling the effective Eddington ratio of dusty and dust-free gas to be different and enabling Mrk 1239 to have a high accretion rate. This radiation-driven dusty wind along with the outflowing ionised gas from Kara et al. (2021) might form a part of a radiative feedback mechanism, theorised by Jiang (2023), within Mrk 1239. To break the degeneracies of the origin of Balmer excess and the dust extinction, more high luminosity AGN with and without evidence for obscuration should be investigated from the X-rays to the near-IR to clarify whether RM lags indicating a flux excess near the Balmer break is connected to dust extinction seen in the spectra of obscured AGN such as Mrk 1239.

3.6.5 Rimmed disc and obscuration on unreddened fluxes

Disc models with infinitely thin profiles are unphysical because they are incompatible with the hydrostatic equilibrium that must be formed because of disc heating from either viscous dissipation or lamp-post irradiation. The analysis above suggests that a rimmed disc cannot explain the larger-than-expected disc sizes as well as the flat spectral shape of the $F_f - F_b$ fluxes and that dust reddening is the likely cause of the discrepancy between the observed and expected disc spectral shape. Nevertheless, a rimmed disc fits the unreddened $F_b - F_f$ fluxes well and it is similar in shape to a thin disc as seen in fig. 3.22. The implied disc sizes from a rimmed disc with an $\dot{m} = 0.30$ and a disc height of $0.01\,\mathrm{light-days}$ at $\sim 1\,\mathrm{light-days}$ from the centre are, on average, larger than the observed lags with the u' and B bands set as the driver (fig. 3.23 and 3.24) with a strong wavelength dependency. The u', $B.$ and g' implied disc lags indicate good agreement as they are less than a factor of 2 in difference from the observed lags; in contrast to the thin disc lags being a factor of $\sim 3-4$ smaller than observations (for example fig. 3.9). However, the r', i', and z_s implied lags are a factor of $\sim 2-3$ and $\sim 3-5$ larger than the observed when the u' and B bands are set as the drivers respectively. Therefore, the rimmed disc model by Starkey et al. (2023) reconciles the larger-than-expected RM lags for bands less than V (5548 Å) as well as the spectral shape when fit to the unreddened fluxes. A factor of $\sim 3-5$ difference remains for the longer wavelength bands. The observed flat spectral shape cannot then be a result of intrinsic disc emission and must result from a non-disc source.

A potential explanation for the smaller-than-expected lags when compared to the rimmed disc could result from a biasing towards smaller lag values. It is expected that RM algorithms measure the average lag Zu et al. (2011); Donnan et al. (2021); Edelson et al. (2017) (hence the need for detrending procedures as in Hernández Santisteban et al. (2020)). Variability time scales smaller than the intrinsic disc emission could, therefore, result in smaller-than-expected measured

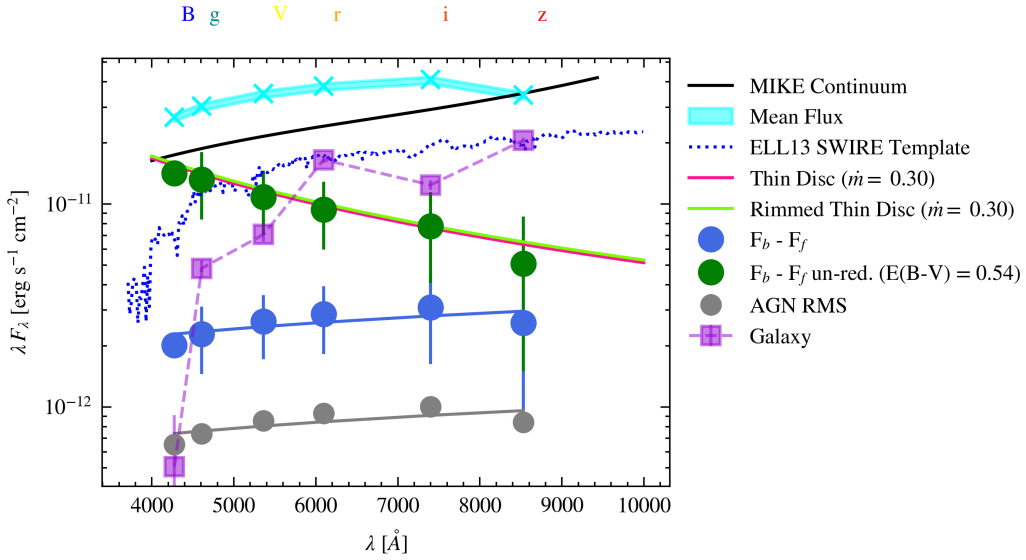

Figure 3.22: Spectral energy distribution in the rest frame of the bright-faint (blue), RMS (grey) component, and the AGN constant component (purple) that is very similar to fig. 3.20. The main difference is that the rimmed disc model is fit to the $F_b - F_f$ fluxes with a disc height of 0.01 light − days at 1 light − day from the centre and with an Eddington ratio of $\dot{m} = 0.30$ corresponding to 14% of L_{Bol} from Pan et al. (2021).

lags. Speculatively, an obscuring outflow model analogous to Kara et al. (2021) could be an explanation. Firstly, there is a dominant $H-\alpha$ BEL in the r' band with a line flux of $\approx 21 \times 10^{-13}\,\mathrm{ergs^{-1}cm^{-2}}$ (see table 3.3); allowing for the possibility of contaminant flux from a non-disc structure causing a bias to the lag. Secondly, the dip seen in the X-ray spectrum around $\sim 2\,\mathrm{keV}$ as in figure 3.21. Indeed, Pan et al. (2021) also refer to dusty outflows but on scales $\leq 100\,\mathrm{pc}$. Contemporaneous multi-wavelength spectroscopy could more precisely connect RM disc structure with spectral features, especially in highly luminous obscured AGN such as Mrk 1239 and the blue(or red)-shifting of the $H-\alpha$ BEL might ascertain the nature of any outflows that might affect RM lags. As Kang et al. (2017) states, blue-shifted $H-\alpha$ lines tend to be associated with biconical outflows in type 2 AGN. Alternatively, it may be the case that the rimmed disc model is invalid for this disc at radii larger than $\approx 1.5\,\mathrm{light-days}$ and, although beyond the scope of this thesis, further augmentations might be needed to the model as described by Starkey et al. (2023).

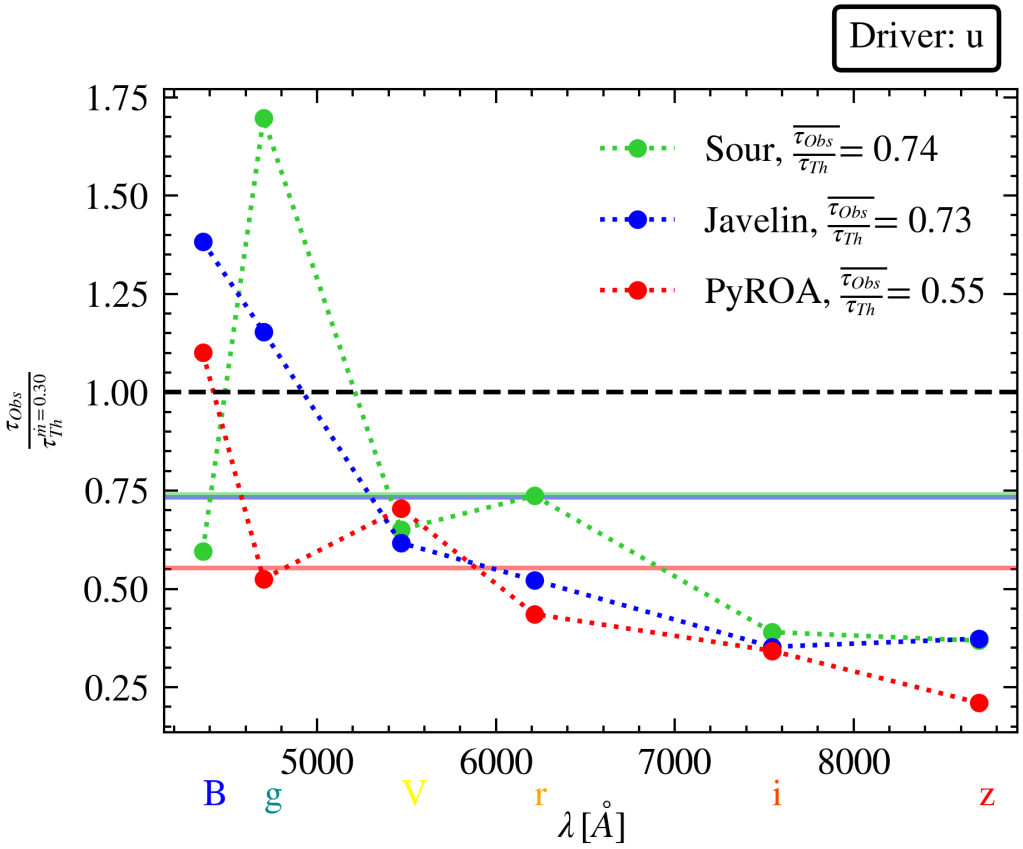

Figure 3.23: Measured lags over theoretical lags from a rimmed disc model relative to the u band for the B, g, V, r, i, z band. Horizontal solid green, blue and red lines are the average difference from the theoretical lags for Sour, Javelin and PyROA respectively.

3.7 Summary

We have performed the first accretion disk reverberation mapping campaign on the narrow-line Seyfert 1 galaxy Mrk 1239. For this study, we have used high-cadence optical light-curve data spanning the near-UV to the near-infrared collected by the Las Cumbres Observatory over $\sim$ 2 years. Our main results can be summarised as follows:

(i) We have used three algorithms; Javelin, PyROA and Sour, with a DRW model, an ROA model, and ICCF method to measure lags from photometric optical light curves. We find consistency between all three algorithms for most of the lag values

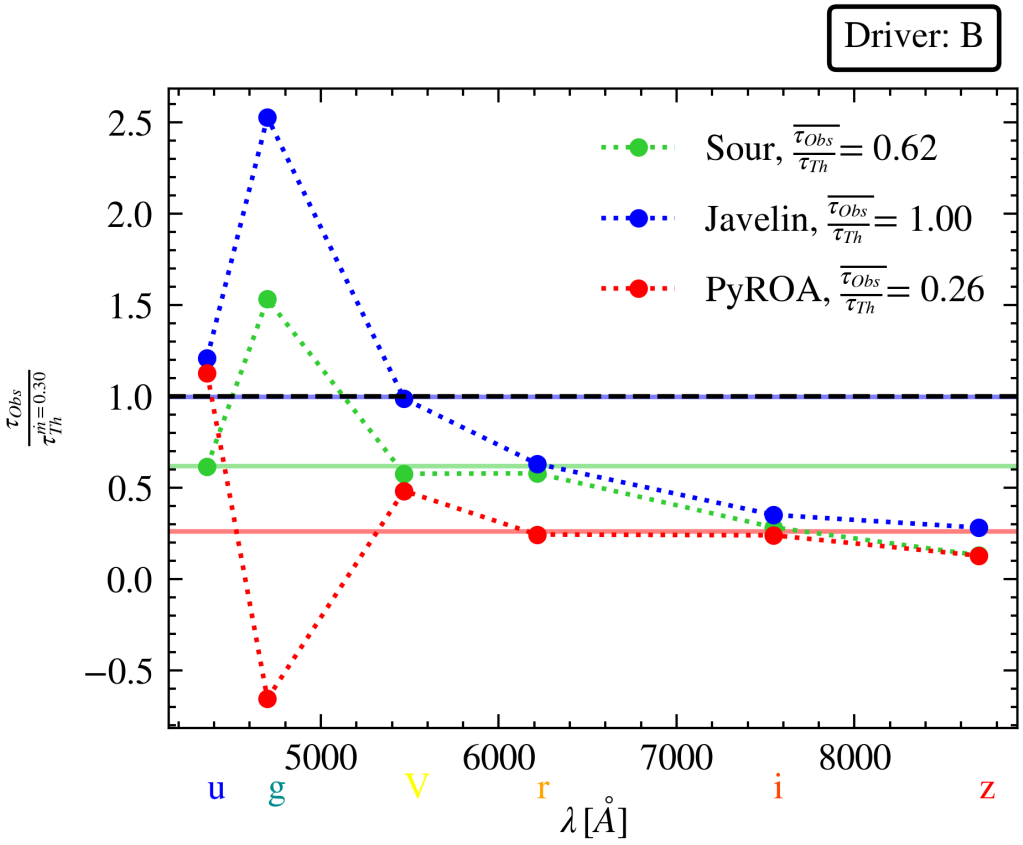

Figure 3.24: Measured lags over theoretical lags from a rimmed disc model relative to the B band for the u, g, V, r, i, z band. Horizontal solid green, blue and red lines are the average difference from the theoretical lags for Sour, Javelin and PyROA respectively.

in tables 3.5, 3.6, and 3.7. Inconsistencies for different driving bands are likely because of the algorithms understating the uncertainties and more investigation of the systematic differences between the three algorithms.

(ii) The lag-spectra best fit for when the V band is set as the driver is the best-constrained and results in a power-law of $\beta = 0.93 \pm 0.60$ with a disc size at the V band of $\tau_{\lambda_0} = 3.66 \pm 2.64$ days; which is a factor of $6 - 10$ larger than expected. Despite the larger-than-expected disc sizes, the lags are consistent with a $\tau \propto \lambda^{\frac{4}{3}}$ power-law expected for the lag-wavelength relationship.

(iii) The fractional variability of the light curves was unexpectedly not monotonically dropping, which prompted our decomposition of the light curves flux into a

variable ($F_f - F_b$) and host galaxy components. The variable component does not match the expected $F_\nu \propto \lambda^{-\frac{1}{3}}$ power law and is instead close to flat.

(iv) Accounting for reddening with an extinction of $E(B-V) = 0.54$ (Rodríguez-Ardila and Mazzalay, 2006) resolves the spectral shape with that of a thin disc for an accretion rate of $\dot{m} = 0.30$.

(v) Reddening does not resolve the disc size problem, however, as the expected disc sizes are still a factor of $3-4$ smaller than measured values. An alternative, rimmed disc model, is not able to accurately reproduce the spectral shape of the decomposed $F_b - F_f$ fluxes without an inner disc radius smaller than the innermost stable circular orbit and an accretion rate $\dot{m} = 0.01$. The average disc size discrepancy lies at a factor of 4.4, 4.3, and 3.3 for Sour, Javelin and PyROA respectively with an accretion rate of $\dot{m} = 0.3$. This is consistent with other RM studies.

(vi) The Starkey et al. (2023) rimmed disc model did, however, fit the $F_b - F_f$ unreddened fluxes as in fig. 3.22 as well as the observed lags except for the r', i', and z_s bands. The discrepancy for the longer wavelength bands could be related to contamination from the $H-\alpha$ line and may be explained with an outflow model analogous to Kara et al. (2021).

Chapter 4

Conclusions

Chapter 2 of this thesis sought a comprehensive comparison of two new RM algorithms, Javelin and PyROA with the legacy ICCF algorithm. Comparing different algorithms with independent methodologies informs the reliability of the RM results and the robustness of the RM theory. Secondly, the comparison was conducted on two different data sets with different variability scales. Koshida et al. (2014), an optical-NIR RM campaign for the dusty torus RM campaign on NGC 5548 and Edelson et al. (2019), a UV/optical RM campaign for the accretion disc of NGC 5548. The primary benchmark of comparison was the extent of agreement with the published results by Koshida et al. (2014). The results from all three algorithms were robust over multiple tests and found, qualitatively, in good agreement with the published figures, after overcoming aliasing problems with Javelin and Sour due to the limits of the parameter search being too large. Aliases were removed by qualitatively identifying peaks symmetric about a time lag of zero days and then constraining the limits of the possible values of time lags. For PyROA, we encountered unrealistic error overlays due to the default Gaussian transfer function and observational gaps in the data, however, this did not affect the lags and they were consistent with Javelin, Sour and Koshida et al. (2014)'s data set.

For the disc RM of NGC 5548, Javelin consistently overestimated the lags when compared to PyROA, Sour and the Edelson et al. (2019) data set itself. We at-

tribute this to further parameter optimisations that were not implemented due to time constraints and a lack of MCMC convergence. We also sought to find any lag excess as Edelson et al. (2019) observed in the U band due to diffuse continuum emission from the BLR contaminating the disc emission. This was observed clearly for PyROA and Sour but not Javelin due to the systematically larger lags. We also tested the expected thin-disc spectra relationship using the Javelin's disc mode and found that the lags fit best a shallower lag spectra with a beta parameter of around 1. This is in agreement with table 4 of Edelson et al. (2019) which suggests a similar power law of close to 1 including the UVOT wavelengths. We achieved consistency between algorithms with independent methods and were also consistent with two sources of RM data that operated on variability timescales with an order of magnitude difference. Validation of the RM theory and the assumptions that underpin it.

Mrk 1239 is an interesting object because it provided further tests of the assumptions of RM. After all, the extent of reddening is unusually high. It was an excellent object to test the commonly observed larger-than-expected disc sizes as observed by Fausnaugh et al. (2016); Mudd et al. (2018); Hlabathe et al. (2020) by a factor of a few from new perspectives and to test new models that seek to resolve the tension analytically, notably, the rimmed disc model by Starkey et al. (2023). We then concluded that the flat spectral shape is non-disc in origin. In this sense, the aims of the second chapter were more exploratory and we used a data-led approach. Applying the algorithm optimisations we learned from Chapter 2, we obtained consistent lags across all three algorithms and multiple RM 'drivers'. We found that although the RM lags were consistent with the $\tau \propto \lambda^{\frac{4}{3}}$ power law they were larger by a factor of $3-4$ than the thin disc model. The rimmed disc model and the disc wind/obscuration model (Kara et al., 2021; Cackett et al., 2023; Neustadt et al., 2023) were discussed as potential explanations for the disc size discrepancy. We reported an unusual fractional variability spectrum which motivated a flux-flux analysis (Hernández Santisteban et al., 2020) to separate the variable compon-

ents of flux from the constant component to reconstruct a disc spectrum using the bright minus faint fluxes and the host galaxy spectrum using the constant component. Crucially, the bright minus faint fluxes did not resemble a disc spectrum. We found with further testing the rimmed disc model to see if it could explain the unusual spectral shape and found that dust reddening is the most plausible cause of it. It became crucial to find an explanation for the spectral shape and Eddington ratio as well as the larger-than-expected disc sizes.

Another possibility that was explored was the disc wind model by Kara et al. (2021) that connects a potential excess in the B, g', and r' bands, a $\sim 2\,\mathrm{kev}$ dip in the x-rays, and the obscuration that produces the flat spectral shape of the disc component by suggesting that the disc winds might be expected enough to form dust but further testing of the Balmer excess should be done to test this. Finally, the rimmed disc model fits the unreddened fluxes well at an Eddington ratio of $\dot{m} = 0.3$, only in the u, B and g' bands does the rimmed disc model reconcile the spectral shape of the unreddened fluxes with the larger-than-expected disc size. The other bands then present lags that are smaller-than-expected concerning the rimmed disc model by a factor of 3-5 which we speculate could be made possible by the Kara et al. (2021) disc wind model creating H Alpha emission in the r band biasing RM analyses to lower lag values for the r, i and z bands.

Looking to the future, contemporaneous multi-wavelength spectroscopy to connect RM disc structures with spectral features with torus dust reddening would be key in the immediate future to validate the rimmed disc model for Mrk 1239 and similarly obscured AGN. Secondly, the cataloguing of AGN outflows and modelling to distinguish outflow emission from BLR emission for the Hydrogen line emission would bring clarity to the UV/X-ray outflow suggested by Kara et al. (2021); Neustadt et al. (2023). Next-generation Big Data surveys combined with advanced RM algorithms, such as Javelin and PyROA, have the potential to resolve an unprecedented number of AGN to high precision. The Legacy Survey of Space and Time (LSST) at the Vera C. Rubin Observatory is expected to cover

upwards of 10 million AGN during its lifetime. For example, extensive simulations by Pozo Nuñez et al. (2023) find that, for LSST, time lags can be recovered up to an accuracy of 5% for light curves with a cadence of 2 days depending on the redshift and contaminant features of the sources. Recent papers highlight specific gains that LSST might have for the field in the coming years. Secunda et al. (2023) find that Javelin can detect long lags of up to several hundred days with LSST mock light curves that might help the study of the vertical structure of accretion discs which would be helpful to put constraints on the rimmed disc model. Brandt and Xmm-Servs Team (2023) reports on the XMM-Newton survey results as well as the proposed STAR-X MIDEX mission would cover LSST deep drilling fields and could facilitate IR to X-ray SED fitting and hence connect spectral features with RM more precisely over a large sample of AGN.

Bibliography

M. A. Abramowicz, B. Czerny, J. P. Lasota, and E. Szuszkiewicz. Slim accretion disks. *The Astrophysical Journal*, 332:646, Sept. 1988. ISSN 0004-637X, 1538-4357. doi: 10.1086/166683. URL http://adsabs.harvard.edu/doi/10.1086/166683.

T. Almeyda, A. Robinson, M. Richmond, R. Nikutta, and B. McDonough. Modeling the Infrared Reverberation Response of the Circumnuclear Dusty Torus in AGNs: An Investigation of Torus Response Functions. *The Astrophysical Journal*, 891(1):26, Feb. 2020. ISSN 0004-637X. doi: 10.3847/1538-4357/ab6aa1. URL https://dx.doi.org/10.3847/1538-4357/ab6aa1. Publisher: The American Astronomical Society.

A. Baskin and A. Laor. Dust inflated accretion disc as the origin of the broad line region in active galactic nuclei. *Monthly Notices of the Royal Astronomical Society*, 474(2):1970–1994, Feb. 2018. ISSN 0035-8711. doi: 10.1093/mnras/stx2850. URL https://doi.org/10.1093/mnras/stx2850.

R. Bernstein, S. A. Shectman, S. M. Gunnels, S. Mochnacki, and A. E. Athey. MIKE: A Double Echelle Spectrograph for the Magellan Telescopes at Las Campanas Observatory. 4841:1694–1704, Mar. 2003. doi: 10.1117/12.461502. URL https://ui.adsabs.harvard.edu/abs/2003SPIE.4841.1694B. Confer-

ence Name: Instrument Design and Performance for Optical/Infrared Ground-based Telescopes ADS Bibcode: 2003SPIE.4841.1694B.

E. Bertin and S. Arnouts. SExtractor: Software for source extraction. *Astronomy and Astrophysics Supplement Series*, 117(2):393–404, June 1996. ISSN 0365-0138, 1286-4846. doi: 10.1051/aas:1996164. URL `https://aas.aanda.org/articles/aas/abs/1996/08/ds1060/ds1060.html`. Number: 2 Publisher: EDP Sciences.

H. Bondi and F. Hoyle. On the mechanism of accretion by stars. *Monthly Notices of the Royal Astronomical Society*, 104:273, Jan. 1944. ISSN 0035-8711. doi: 10.1093/mnras/104.5.273. URL `https://ui.adsabs.harvard.edu/abs/1944MNRAS.104..273B`. ADS Bibcode: 1944MNRAS.104..273B.

W. Brandt and Xmm-Servs Team. X-ray Coverage of the LSST Deep-Drilling Fields: Current XMM-SERVS Results and Future Prospects. 55:100.02, Sept. 2023. URL `https://ui.adsabs.harvard.edu/abs/2023HEAD...2010002B`. Conference Name: AAS/High Energy Astrophysics Division ADS Bibcode: 2023HEAD...2010002B.

A. A. Breeveld, W. Landsman, S. T. Holland, P. Roming, N. P. M. Kuin, and M. J. Page. An Updated Ultraviolet Calibration for the Swift/UVOT. 1358:373–376, Aug. 2011. doi: 10.1063/1.3621807. URL `https://ui.adsabs.harvard.edu/abs/2011AIPC.1358..373B`. Conference Name: Gamma Ray Bursts 2010 Place: eprint: arXiv:1102.4717 ADS Bibcode: 2011AIPC.1358..373B.

M. Z. Buhariwalla, S. G. H. Waddell, L. C. Gallo, D. Grupe, and S. Komossa. Uncovering the Primary X-Ray Emission and Possible Starburst Component in the Polarized NLS1 Mrk 1239. *The Astrophysical Journal*, 901(2):118, Oct. 2020. ISSN 0004-637X, 1538-4357. doi: 10.3847/1538-4357/abb08a. URL `https://iopscience.iop.org/article/10.3847/1538-4357/abb08a`.

M. Z. Buhariwalla, L. C. Gallo, J. Mao, S. Komossa, J. Jiang, A. Gonzalez, and D. Grupe. The collisional and photoionized plasma in the polarized NLS1 galaxy Mrk 1239. *Monthly Notices of the Royal Astronomical Society*, 521: 2378–2390, May 2023. ISSN 0035-8711. doi: 10.1093/mnras/stad265. URL https://ui.adsabs.harvard.edu/abs/2023MNRAS.521.2378B. ADS Bibcode: 2023MNRAS.521.2378B.

E. M. Cackett, K. Horne, and H. Winkler. Testing thermal reprocessing in active galactic nuclei accretion discs. *Monthly Notices of the Royal Astronomical Society*, 380(2):669–682, Aug. 2007. ISSN 0035-8711. doi: 10.1111/j.1365-2966.2007.12098.x. URL https://doi.org/10.1111/j.1365-2966.2007.12098.x.

E. M. Cackett, J. Gelbord, Y.-R. Li, K. Horne, J.-M. Wang, A. J. Barth, J.-M. Bai, W.-H. Bian, R. W. Carroll, P. Du, R. Edelson, M. R. Goad, L. C. Ho, C. Hu, V. C. Khatu, B. Luo, J. Miller, and Y.-F. Yuan. Supermassive Black Holes with High Accretion Rates in Active Galactic Nuclei. XI. Accretion Disk Reverberation Mapping of Mrk 142. *The Astrophysical Journal*, 896:1, June 2020. ISSN 0004-637X. doi: 10.3847/1538-4357/ab91b5. URL https://ui.adsabs.harvard.edu/abs/2020ApJ...896....1C. ADS Bibcode: 2020ApJ...896....1C.

E. M. Cackett, M. C. Bentz, and E. Kara. Reverberation mapping of active galactic nuclei: From X-ray corona to dusty torus. *iScience*, 24(6):102557, June 2021. ISSN 25890042. doi: 10.1016/j.isci.2021.102557. URL https://linkinghub.elsevier.com/retrieve/pii/S2589004221005253.

E. M. Cackett, A. Zoghbi, and O. Ulrich. Frequency-resolved lags in UV/optical continuum reverberation mapping. *The Astrophysical Journal*, 925(1):29, Jan. 2022. ISSN 0004-637X, 1538-4357. doi: 10.3847/1538-4357/ac3913. URL http://arxiv.org/abs/2109.02155. arXiv:2109.02155 [astro-ph].

E. M. Cackett, J. Gelbord, A. J. Barth, G. De Rosa, R. Edelson, M. R. Goad, Y. Homayouni, K. Horne, E. A. Kara, G. A. Kriss, K. T. Korista, H. Landt, R. Plesha,

N. Arav, M. C. Bentz, B. D. Boizelle, E. Dalla Bonta, M. Dehghanian, F. Donnan, P. Du, G. J. Ferland, C. Fian, A. V. Filippenko, D. H. Gonzalez Buitrago, C. J. Grier, P. B. Hall, C. Hu, D. Ilic, J. Kaastra, S. Kaspi, C. S. Kochanek, A. B. Kovacevic, D. Kynoch, Y.-R. Li, J. N. McLane, M. Mehdipour, J. A. Miller, J. Montano, H. Netzer, C. Panagiotou, E. Partington, L. C. Popovic, D. Proga, D. Rogantini, D. Sanmartim, M. R. Siebert, T. Storchi-Bergmann, M. Vestergaard, J.-M. Wang, T. Waters, and F. Zaidouni. AGN STORM 2. IV. Swift X-ray and ultraviolet/optical monitoring of Mrk 817, June 2023. URL `https://ui.adsabs.harvard.edu/abs/2023arXiv230617663C`. Publication Title: arXiv e-prints ADS Bibcode: 2023arXiv230617663C.

J. H.-H. Chan, M. Millon, V. Bonvin, and F. Courbin. Twisted quasar light curves: implications for continuum reverberation mapping of accretion disks. *Astronomy & Astrophysics*, 636:A52, Apr. 2020. ISSN 0004-6361, 1432-0746. doi: 10.1051/0004-6361/201935423. URL `https://www.aanda.org/10.1051/0004-6361/201935423`.

S. J. Collier. *Measuring the Hubble constant from reverberating accretion discs in active galaxies*. Thesis, University of St Andrews, 1999. URL `https://research-repository.st-andrews.ac.uk/handle/10023/14517`. Accepted: 2018-06-25T09:39:09Z.

B. Czerny. Slim accretion disks: theory and observational consequences, May 2019. URL `http://arxiv.org/abs/1905.00120`. arXiv:1905.00120 [astro-ph].

B. Czerny, Y.-R. Li, K. Hryniewicz, S. Panda, C. Wildy, M. Sniegowska, J.-M. Wang, J. Sredzinska, and V. Karas. Failed Radiatively Accelerated Dusty Outflow Model of the Broad Line Region in Active Galactic Nuclei. I. Analytical Solution. *The Astrophysical Journal*, 846(2):154, Sept. 2017. ISSN 0004-637X. doi: 10.3847/1538-4357/aa8810. URL `https://dx.doi.org/10.3847/1538-4357/aa8810`. Publisher: The American Astronomical Society.

S. W. Davis and A. Laor. THE RADIATIVE EFFICIENCY OF ACCRETION FLOWS IN INDIVIDUAL ACTIVE GALACTIC NUCLEI. *The Astrophysical Journal*, 728(2):98, Feb. 2011. ISSN 0004-637X, 1538-4357. doi: 10.1088/0004-637X/728/2/98. URL https://iopscience.iop.org/article/10.1088/0004-637X/728/2/98.

J. Dexter, J. Shangguan, S. Hönig, M. Kishimoto, D. Lutz, H. Netzer, R. Davies, E. Sturm, O. Pfuhl, A. Amorim, M. Bauböck, W. Brandner, Y. Clénet, P. T. d. Zeeuw, A. Eckart, F. Eisenhauer, N. M. F. Schreiber, F. Gao, P. J. V. Garcia, R. Genzel, S. Gillessen, D. Gratadour, A. Jiménez-Rosales, S. Lacour, F. Millour, T. Ott, T. Paumard, K. Perraut, G. Perrin, B. M. Peterson, P. O. Petrucci, M. A. Prieto, D. Rouan, M. Schartmann, T. Shimizu, A. Sternberg, O. Straub, C. Straubmeier, L. J. Tacconi, K. Tristram, P. Vermot, I. Waisberg, F. Widmann, and J. Woillez. The resolved size and structure of hot dust in the immediate vicinity of AGN. *Astronomy & Astrophysics*, 635:A92, Mar. 2020. ISSN 0004-6361, 1432-0746. doi: 10.1051/0004-6361/201936767. URL https://www.aanda.org/articles/aa/abs/2020/03/aa36767-19/aa36767-19.html. Publisher: EDP Sciences.

A. Doi, K. Wajima, Y. Hagiwara, and M. Inoue. A Fanaroff-Riley Type I Candidate in Narrow-Line Seyfert 1 Galaxy Mrk 1239. *The Astrophysical Journal*, 798: L30, Jan. 2015. ISSN 0004-637X. doi: 10.1088/2041-8205/798/2/L30. URL https://ui.adsabs.harvard.edu/abs/2015ApJ...798L..30D. ADS Bibcode: 2015ApJ...798L..30D.

F. R. Donnan, K. Horne, and J. V. Hernández Santisteban. Bayesian analysis of quasar light curves with a running optimal average: new time delay measurements of COSMOGRAIL gravitationally lensed quasars. *Monthly Notices of the Royal Astronomical Society*, 508:5449–5467, Dec. 2021. ISSN 0035-8711. doi: 10.1093/mnras/stab2832. URL https://ui.adsabs.harvard.edu/abs/2021MNRAS.508.5449D. ADS Bibcode: 2021MNRAS.508.5449D.

F. R. Donnan, J. V. Hernández Santisteban, K. Horne, C. Hu, P. Du, Y.-R. Li, M. Xiao, L. C. Ho, J. Aceituno, J.-M. Wang, W.-J. Guo, S. Yang, B.-W. Jiang, and Z.-H. Yao. Testing super-eddington accretion on to a supermassive black hole: reverberation mapping of PG 1119+120. *Monthly Notices of the Royal Astronomical Society*, 523(1):545–567, July 2023. ISSN 0035-8711. doi: 10.1093/mnras/stad1409. URL https://doi.org/10.1093/mnras/stad1409.

M. Dovc̆iak, E. Kara, V. Karas, B. D. Marco, G. Matt, G. Miniutti, and W. Alston. Reverberation mapping in the lamp-post geometry of the compact corona illuminating a black-hole accretion disc in AGN.

P. Du, K.-X. Lu, Z.-X. Zhang, Y.-K. Huang, K. Wang, C. Hu, J. Qiu, Y.-R. Li, X.-L. Fan, X.-E. Fang, J.-M. Bai, W.-H. Bian, Y.-F. Yuan, L. C. Ho, J.-M. Wang, and SEAMBH Collaboration. Supermassive Black Holes with High Accretion Rates in Active Galactic Nuclei. V. A New Size-Luminosity Scaling Relation for the Broad-line Region. *The Astrophysical Journal*, 825:126, July 2016. ISSN 0004-637X. doi: 10.3847/0004-637X/825/2/126. URL https://ui.adsabs.harvard.edu/abs/2016ApJ...825..126D. ADS Bibcode: 2016ApJ...825..126D.

J. Ebrero, J. S. Kaastra, G. A. Kriss, L. D. Gesu, E. Costantini, M. Mehdipour, S. Bianchi, M. Cappi, R. Boissay, G. Branduardi-Raymont, P.-O. Petrucci, G. Ponti, F. P. Núñez, H. Seta, K. C. Steenbrugge, and M. Whewell. Anatomy of the AGN in NGC 5548 - VI. Long-term variability of the warm absorber. *Astronomy & Astrophysics*, 587:A129, Mar. 2016. ISSN 0004-6361, 1432-0746. doi: 10.1051/0004-6361/201527808. URL https://www.aanda.org/articles/aa/abs/2016/03/aa27808-15/aa27808-15.html. Publisher: EDP Sciences.

R. Edelson, J. M. Gelbord, K. Horne, I. M. McHardy, B. M. Peterson, P. Arévalo, A. A. Breeveld, G. De Rosa, P. A. Evans, M. R. Goad, G. A. Kriss, W. N. Brandt, N. Gehrels, D. Grupe, J. A. Kennea, C. S. Kochanek, J. A. Nousek, I. Papadakis, M. Siegel, D. Starkey, P. Uttley, S. Vaughan, S. Young, A. J. Barth, M. C. Bentz, B. J. Brewer, D. M. Crenshaw, E. Dalla Bontà, A. De Lorenzo-

Cáceres, K. D. Denney, M. Dietrich, J. Ely, M. M. Fausnaugh, C. J. Grier, P. B. Hall, J. Kaastra, B. C. Kelly, K. T. Korista, P. Lira, S. Mathur, H. Netzer, A. Pancoast, L. Pei, R. W. Pogge, J. S. Schimoia, T. Treu, M. Vestergaard, C. Villforth, H. Yan, and Y. Zu. Space Telescope and Optical Reverberation Mapping Project. II. Swift and HST Reverberation Mapping of the Accretion Disk of NGC 5548. *The Astrophysical Journal*, 806:129, June 2015. ISSN 0004-637X. doi: 10.1088/0004-637X/806/1/129. URL `https://ui.adsabs.harvard.edu/abs/2015ApJ...806..129E`. ADS Bibcode: 2015ApJ...806..129E.

R. Edelson, J. Gelbord, E. Cackett, S. Connolly, C. Done, M. Fausnaugh, E. Gardner, N. Gehrels, M. Goad, K. Horne, I. McHardy, B. M. Peterson, S. Vaughan, M. Vestergaard, A. Breeveld, A. J. Barth, M. Bentz, M. Bottorff, W. N. Brandt, S. M. Crawford, E. D. Bontà, D. Emmanoulopoulos, P. Evans, R. F. Jaimes, A. V. Filippenko, G. Ferland, D. Grupe, M. Joner, J. Kennea, K. T. Korista, H. A. Krimm, G. Kriss, D. C. Leonard, S. Mathur, H. Netzer, J. Nousek, K. Page, E. Romero-Colmenero, M. Siegel, D. A. Starkey, T. Treu, H. A. Vogler, H. Winkler, and W. Zheng. Swift Monitoring of NGC 4151: Evidence for a Second X-Ray/UV Reprocessing. *The Astrophysical Journal*, 840 (1):41, May 2017. ISSN 0004-637X. doi: 10.3847/1538-4357/aa6890. URL `https://dx.doi.org/10.3847/1538-4357/aa6890`. Publisher: The American Astronomical Society.

R. Edelson, J. Gelbord, E. Cackett, B. M. Peterson, K. Horne, A. J. Barth, D. A. Starkey, M. Bentz, W. N. Brandt, M. Goad, M. Joner, K. Korista, H. Netzer, K. Page, P. Uttley, S. Vaughan, A. Breeveld, S. B. Cenko, C. Done, P. Evans, M. Fausnaugh, G. Ferland, D. Gonzalez-Buitrago, J. Gropp, D. Grupe, J. Kaastra, J. Kennea, G. Kriss, S. Mathur, M. Mehdipour, D. Mudd, J. Nousek, T. Schmidt, M. Vestergaard, and C. Villforth. The First *Swift* Intensive AGN Accretion Disk Reverberation Mapping Survey. *The Astrophysical Journal*, 870 (2):123, Jan. 2019. ISSN 1538-4357. doi: 10.3847/1538-4357/aaf3b4. URL `https://iopscience.iop.org/article/10.3847/1538-4357/aaf3b4`.

R. A. Edelson and M. A. Malkan. Spectral energy distributions of active galactic nuclei between 0.1 and 100 microns. *The Astrophysical Journal*, 308:59, Sept. 1986. ISSN 0004-637X, 1538-4357. doi: 10.1086/164479. URL `http://adsabs.harvard.edu/doi/10.1086/164479`.

Emma Alexander. unified_agn.png (968×834), Jan. 2023. URL `https://emmaalexander.github.io/images/unified_agn.png`.

ESA/Hubble. Active Galactic Nucleus, Apr. 2023. URL `https://esahubble.org/wordbank/active-galactic-nucleus/`. information@eso.org.

M. M. Fausnaugh. *Reverberation Mapping of the Continuum Source in Active Galactic Nuclei*. PhD thesis, The Ohio State University, 2017. URL `https://etd.ohiolink.edu/apexprod/rws_olink/r/1501/10?clear=10&p10_accession_num=osu1494244528720735`.

M. M. Fausnaugh, K. D. Denney, A. J. Barth, M. C. Bentz, M. C. Bottorff, M. T. Carini, K. V. Croxall, G. De Rosa, M. R. Goad, K. Horne, M. D. Joner, S. Kaspi, M. Kim, S. A. Klimanov, C. S. Kochanek, D. C. Leonard, H. Netzer, B. M. Peterson, K. Schnülle, S. G. Sergeev, M. Vestergaard, W. K. Zheng, Y. Zu, M. D. Anderson, P. Arévalo, C. Bazhaw, G. A. Borman, T. A. Boroson, W. N. Brandt, A. A. Breeveld, B. J. Brewer, E. M. Cackett, D. M. Crenshaw, E. Dalla Bontà, A. De Lorenzo-Cáceres, M. Dietrich, R. Edelson, N. V. Efimova, J. Ely, P. A. Evans, A. V. Filippenko, K. Flatland, N. Gehrels, S. Geier, J. M. Gelbord, L. Gonzalez, V. Gorjian, C. J. Grier, D. Grupe, P. B. Hall, S. Hicks, D. Horenstein, T. Hutchison, M. Im, J. J. Jensen, J. Jones, J. Kaastra, B. C. Kelly, J. A. Kennea, S. C. Kim, K. T. Korista, G. A. Kriss, J. C. Lee, P. Lira, F. MacInnis, E. R. Manne-Nicholas, S. Mathur, I. M. McHardy, C. Montouri, R. Musso, S. V. Nazarov, R. P. Norris, J. A. Nousek, D. N. Okhmat, A. Pancoast, I. Papadakis, J. R. Parks, L. Pei, R. W. Pogge, J. U. Pott, S. E. Rafter, H. W. Rix, D. A. Saylor, J. S. Schimoia, M. Siegel, M. Spencer, D. Starkey, H. I. Sung, K. G. Teems, T. Treu, C. S. Turner, P. Uttley,

C. Villforth, Y. Weiss, J. H. Woo, H. Yan, and S. Young. Space Telescope and Optical Reverberation Mapping Project. III. Optical Continuum Emission and Broadband Time Delays in NGC 5548. *The Astrophysical Journal*, 821: 56, Apr. 2016. ISSN 0004-637X. doi: 10.3847/0004-637X/821/1/56. URL https://ui.adsabs.harvard.edu/abs/2016ApJ...821...56F. ADS Bibcode: 2016ApJ...821...56F.

C. Fian, D. Chelouche, S. Kaspi, C. Sobrino Figaredo, T. Lewis, and S. Catalan. Continuum reverberation mapping of MCG 08-11-011. *Astronomy and Astrophysics*, 672:A132, Apr. 2023. ISSN 0004-6361. doi: 10.1051/0004-6361/202244905. URL https://ui.adsabs.harvard.edu/abs/2023A&A...672A.132F. ADS Bibcode: 2023A&A...672A.132F.

E. L. Fitzpatrick. Correcting for the Effects of Interstellar Extinction. *Publications of the Astronomical Society of the Pacific*, 111(755):63, Jan. 1999. ISSN 1538-3873. doi: 10.1086/316293. URL https://iopscience.iop.org/article/10.1086/316293/meta. Publisher: IOP Publishing.

H. A. Flewelling, E. A. Magnier, K. C. Chambers, J. N. Heasley, C. Holmberg, M. E. Huber, W. Sweeney, C. Z. Waters, A. Calamida, S. Casertano, X. Chen, D. Farrow, G. Hasinger, R. Henderson, K. S. Long, N. Metcalfe, G. Narayan, M. A. Nieto-Santisteban, P. Norberg, A. Rest, R. P. Saglia, A. Szalay, A. R. Thakar, J. L. Tonry, J. Valenti, S. Werner, R. White, L. Denneau, P. W. Draper, K. W. Hodapp, R. Jedicke, N. Kaiser, R. P. Kudritzki, P. A. Price, R. J. Wainscoat, S. Chastel, B. McLean, M. Postman, and B. Shiao. The Pan-STARRS1 Database and Data Products. *The Astrophysical Journal Supplement Series*, 251(1):7, Oct. 2020. ISSN 0067-0049. doi: 10.3847/1538-4365/abb82d. URL https://dx.doi.org/10.3847/1538-4365/abb82d. Publisher: The American Astronomical Society.

J. Frank, A. King, and D. J. Raine. *Accretion Power in Astrophysics: Third Edition*. Jan. 2002. URL https://ui.adsabs.harvard.edu/abs/2002apa.

.book.....F. Publication Title: Accretion Power in Astrophysics ADS Bibcode: 2002apa..book.....F.

C. M. Gaskell and B. M. Peterson. The accuracy of cross-correlation estimates of quasar emission-line region sizes. *The Astrophysical Journal Supplement Series*, 65:1, Sept. 1987. ISSN 0067-0049, 1538-4365. doi: 10.1086/191216. URL http://adsabs.harvard.edu/doi/10.1086/191216.

C. M. Gaskell and L. S. Sparke. Line Variations in Quasars and Seyfert Galaxies. *The Astrophysical Journal*, 305:175, June 1986. ISSN 0004-637X. doi: 10.1086/164238. URL https://ui.adsabs.harvard.edu/abs/1986ApJ...305..175G. ADS Bibcode: 1986ApJ...305..175G.

R. W. Goodrich. Spectropolarimetry of "Narrow-Line" Seyfert 1 Galaxies. *The Astrophysical Journal*, 342:224, July 1989. ISSN 0004-637X. doi: 10.1086/167586. URL https://ui.adsabs.harvard.edu/abs/1989ApJ...342..224G. ADS Bibcode: 1989ApJ...342..224G.

C. M. Harrison. Observational constraints on the influence of active galactic nuclei on the evolution of galaxies. Feb. 2014.

J. V. Hernández Santisteban, R. Edelson, K. Horne, J. M. Gelbord, A. J. Barth, E. M. Cackett, M. R. Goad, H. Netzer, D. Starkey, P. Uttley, W. N. Brandt, K. Korista, A. M. Lohfink, C. A. Onken, K. L. Page, M. Siegel, M. Vestergaard, S. Bisogni, A. A. Breeveld, S. B. Cenko, E. Dalla Bontà, P. A. Evans, G. Ferland, D. H. Gonzalez-Buitrago, D. Grupe, M. D. Joner, G. Kriss, S. J. LaPorte, S. Mathur, F. Marshall, M. Mehdipour, D. Mudd, B. M. Peterson, T. Schmidt, S. Vaughan, and S. Valenti. Intensive disc-reverberation mapping of Fairall 9: first year of Swift and LCO monitoring. *Monthly Notices of the Royal Astronomical Society*, 498(4):5399–5416, Oct. 2020. ISSN 0035-8711. doi: 10.1093/mnras/staa2365. URL https://doi.org/10.1093/mnras/staa2365.

M. S. Hlabathe, D. A. Starkey, K. Horne, E. Romero-Colmenero, S. M. Crawford, S. Valenti, H. Winkler, A. J. Barth, C. A. Onken, D. J. Sand, T. Treu, A. M. Diamond-Stanic, and C. Villforth. Robotic reverberation mapping of the broad-line radio galaxy 3C 120. *Monthly Notices of the Royal Astronomical Society*, 497(3):2910–2929, Sept. 2020. ISSN 0035-8711. doi: 10.1093/mnras/staa2171. URL `https://doi.org/10.1093/mnras/staa2171`.

Jeanette Gladstone. Multicoloured disc blackbody spectrum. URL `https://sites.ualberta.ca/~jgladsto/Site/accretion.html`.

V. K. Jha, R. Joshi, H. Chand, X.-B. Wu, L. C. Ho, S. Rastogi, and Q. Ma. Accretion Disk Sizes from Continuum Reverberation Mapping of AGN Selected from the ZTF Survey. *Monthly Notices of the Royal Astronomical Society*, 511(2): 3005–3016, Feb. 2022. ISSN 0035-8711, 1365-2966. doi: 10.1093/mnras/stac109. URL `http://arxiv.org/abs/2109.05036`. arXiv:2109.05036 [astro-ph].

J. Jiang. A Highly Accreting Low-Mass Black Hole Hidden in the Dust. 55: 100.17, Sept. 2023. URL `https://ui.adsabs.harvard.edu/abs/2023HEAD...2010017J`. Conference Name: AAS/High Energy Astrophysics Division ADS Bibcode: 2023HEAD...2010017J.

D. Kang, J.-H. Woo, and H.-J. Bae. Outflow kinematics manifested by the H-alpha line: gas outflows in Type 2 AGNs. IV. *The Astrophysical Journal*, 845 (2):131, Aug. 2017. ISSN 1538-4357. doi: 10.3847/1538-4357/aa80e8. URL `http://arxiv.org/abs/1707.05895`. arXiv:1707.05895 [astro-ph].

E. Kara, M. Mehdipour, G. A. Kriss, E. M. Cackett, N. Arav, A. J. Barth, D. Byun, M. S. Brotherton, G. De Rosa, J. Gelbord, J. V. Hernández Santisteban, C. Hu, J. Kaastra, H. Landt, Y.-R. Li, J. A. Miller, J. Montano, E. Partington, J. Aceituno, J.-M. Bai, D. Bao, M. C. Bentz, T. G. Brink, D. Chelouche, Y.-J. Chen, E. R. Colmenero, E. D. Bontà, M. Dehghanian, P. Du, R. Edelson, G. J. Ferland, L. Ferrarese, C. Fian, A. V. Filippenko, T. Fischer, M. R. Goad, D. H. González Buitrago, V. Gorjian, C. J. Grier, W.-J. Guo, P. B. Hall, L. C. Ho,

Y. Homayouni, K. Horne, D. Ilić, B.-W. Jiang, M. D. Joner, S. Kaspi, C. S. Kochanek, K. T. Korista, D. Kynoch, S.-S. Li, J.-R. Liu, I. M. M. cHardy, J. N. McLane, J. A. J. Mitchell, H. Netzer, K. A. Olson, R. W. Pogge, L. C. Popović, D. Proga, T. Storchi-Bergmann, E. Strasburger, T. Treu, M. Vestergaard, J.-M. Wang, M. J. Ward, T. Waters, P. R. Williams, S. Yang, Z.-H. Yao, T. E. Zastrocky, S. Zhai, and Y. Zu. AGN STORM 2. I. First results: A Change in the Weather of Mrk 817. *The Astrophysical Journal*, 922(2):151, Dec. 2021. ISSN 0004-637X, 1538-4357. doi: 10.3847/1538-4357/ac2159. URL `https://iopscience.iop.org/article/10.3847/1538-4357/ac2159`.

B. C. Kelly, J. Bechtold, and A. Siemiginowska. Are the Variations in Quasar Optical Flux Driven by Thermal Fluctuations? *The Astrophysical Journal*, 698: 895–910, June 2009. ISSN 0004-637X. doi: 10.1088/0004-637X/698/1/895. URL `https://ui.adsabs.harvard.edu/abs/2009ApJ...698..895K`. ADS Bibcode: 2009ApJ...698..895K.

M. Kishimoto, S. F. Hönig, R. Antonucci, F. Millour, K. R. W. Tristram, and G. Weigelt. Mapping the radial structure of AGN tori. *Astronomy & Astrophysics*, 536:A78, Dec. 2011. ISSN 0004-6361, 1432-0746. doi: 10.1051/0004-6361/201117367. URL `http://www.aanda.org/10.1051/0004-6361/201117367`.

C. Knigge, K. S. Long, R. A. Wade, R. Baptista, K. Horne, I. Hubeny, and R. G. M. Rutten. Hubble Space Telescope Eclipse Observations of the Nova-like Cataclysmic Variable UX Ursae Majoris*. *The Astrophysical Journal*, 499 (1):414, May 1998. ISSN 0004-637X. doi: 10.1086/305617. URL `https://iopscience.iop.org/article/10.1086/305617/meta`. Publisher: IOP Publishing.

Y. Kobayashi, Y. Yoshii, B. A. Peterson, S. Miyazaki, T. Aoki, T. Minezaki, K. Kawara, K. Enya, N. Okada, M. Suganuma, B. Greene, M. O'Brien, and L. K. Randall. MAGNUM (multicolor active galactic nuclei monitoring) Project. In *Advanced Technology Optical/IR Telescopes VI*, volume 3352,

pages 120–128. SPIE, Aug. 1998. doi: 10.1117/12.319247. URL https://www.spiedigitallibrary.org/conference-proceedings-of-spie/3352/0000/MAGNUM-multicolor-active-galactic-nuclei-monitoring-Project/10.1117/12.319247.full.

M. Kokubo. Constraints on accretion disk size in the massive type 1 quasar PG 2308+098 from optical continuum reverberation lags. *Publications of the Astronomical Society of Japan*, 70(5):97, Oct. 2018. ISSN 0004-6264. doi: 10.1093/pasj/psy096. URL https://doi.org/10.1093/pasj/psy096.

A. P. Koratkar and C. M. Gaskell. Radius-Luminosity and Mass-Luminosity Relationships for Active Galactic Nuclei. *The Astrophysical Journal*, 370:L61, Apr. 1991. ISSN 0004-637X. doi: 10.1086/185977. URL https://ui.adsabs.harvard.edu/abs/1991ApJ...370L..61K. ADS Bibcode: 1991ApJ...370L..61K.

K. T. Korista and M. R. Goad. Quantifying the impact of variable BLR diffuse continuum contributions on measured continuum interband delays. *Monthly Notices of the Royal Astronomical Society*, 489(4):5284–5300, Nov. 2019. ISSN 0035-8711. doi: 10.1093/mnras/stz2330. URL https://doi.org/10.1093/mnras/stz2330.

S. Koshida, T. Minezaki, Y. Yoshii, Y. Kobayashi, Y. Sakata, S. Sugawara, K. Enya, M. Suganuma, H. Tomita, T. Aoki, and B. A. Peterson. REVERBERATION MEASUREMENTS OF THE INNER RADIUS OF THE DUST TORUS IN 17 SEYFERT GALAXIES. *The Astrophysical Journal*, 788(2):159, June 2014. ISSN 0004-637X, 1538-4357. doi: 10.1088/0004-637X/788/2/159. URL https://iopscience.iop.org/article/10.1088/0004-637X/788/2/159.

J. H. Krolik. *Active Galactic Nuclei. From the Central Black Hole to the Galactic Environment.* Jan. 1999. URL https://ui.adsabs.harvard.edu/abs/1999agnf.book.....K. Publication Title: Active Galactic Nuclei. From the Central Black Hole to the Galactic Environment. Julian H. Krolik. ISBN: 9780691227474. Princeton University Press ADS Bibcode: 1999agnf.book.....K.

J. H. Krolik, K. Horne, T. R. Kallman, M. A. Malkan, R. A. Edelson, and G. A. Kriss. Ultraviolet variability of NGC 5548 - Dynamics of the continuum production region and geometry of the broad-line region. *The Astrophysical Journal*, 371:541, Apr. 1991. ISSN 0004-637X, 1538-4357. doi: 10.1086/169918. URL `http://adsabs.harvard.edu/doi/10.1086/169918`.

H. Landt, M. C. Bentz, B. M. Peterson, M. Elvis, M. J. Ward, K. T. Korista, and M. Karovska. The near-infrared radius-luminosity relationship for active galactic nuclei: Near-IR radius-luminosity relationship. *Monthly Notices of the Royal Astronomical Society: Letters*, 413(1):L106–L109, May 2011. ISSN 17453925. doi: 10.1111/j.1745-3933.2011.01047.x. URL `https://academic.oup.com/mnrasl/article-lookup/doi/10.1111/j.1745-3933.2011.01047.x`.

H. Landt, M. J. Ward, D. Kynoch, C. Packham, G. J. Ferland, A. Lawrence, J. U. Pott, J. Esser, K. Horne, D. A. Starkey, D. Malhotra, M. M. Fausnaugh, B. M. Peterson, R. J. Wilman, R. A. Riffel, T. Storchi-Bergmann, A. J. Barth, C. Villforth, and H. Winkler. The first spectroscopic dust reverberation programme on active galactic nuclei: the torus in NGC 5548. *Monthly Notices of the Royal Astronomical Society*, 489:1572–1589, Oct. 2019. ISSN 0035-8711. doi: 10.1093/mnras/stz2212. URL `https://ui.adsabs.harvard.edu/abs/2019MNRAS.489.1572L`. ADS Bibcode: 2019MNRAS.489.1572L.

R. L. Larson, S. L. Finkelstein, D. D. Kocevski, T. A. Hutchison, J. R. Trump, P. A. Haro, V. Bromm, N. J. Cleri, M. Dickinson, S. Fujimoto, J. S. Kartaltepe, A. M. Koekemoer, C. Papovich, N. Pirzkal, S. Tacchella, J. A. Zavala, M. Bagley, P. Behroozi, J. B. Champagne, J. W. Cole, I. Jung, A. M. Morales, G. Yang, H. Zhang, A. Zitrin, R. O. Amorín, D. Burgarella, C. M. Casey, A. C. Ortiz, I. G. Cox, K. Chworowsky, A. Fontana, E. Gawiser, A. Grazian, N. A. Grogin, S. Harish, N. P. Hathi, M. Hirschmann, B. W. Holwerda, S. Juneau, G. C. K. Leung, R. A. Lucas, E. J. McGrath, P. G. Pérez-González, J. R. Rigby, L.-M. Seillé, R. C. Simons, B. J. Weiner, S. M. Wilkins, L. Y. A. Yung, and T. C.

Team. A CEERS Discovery of an Accreting Supermassive Black Hole 570 Myr after the Big Bang: Identifying a Progenitor of Massive z > 6 Quasars, Mar. 2023. URL http://arxiv.org/abs/2303.08918. arXiv:2303.08918 [astro-ph].

L.-X. Li, E. R. Zimmerman, R. Narayan, and J. E. McClintock. Multitemperature Blackbody Spectrum of a Thin Accretion Disk around a Kerr Black Hole: Model Computations and Comparison with Observations. *The Astrophysical Journal Supplement Series*, 157(2):335, Apr. 2005. ISSN 0067-0049. doi: 10.1086/428089. URL https://iopscience.iop.org/article/10.1086/428089/meta. Publisher: IOP Publishing.

C. L. MacLeod, Ivezić, C. S. Kochanek, S. Kozłowski, B. Kelly, E. Bullock, A. Kimball, B. Sesar, D. Westman, K. Brooks, R. Gibson, A. C. Becker, and W. H. de Vries. Modeling the Time Variability of SDSS Stripe 82 Quasars as a Damped Random Walk. *The Astrophysical Journal*, 721:1014–1033, Oct. 2010. ISSN 0004-637X. doi: 10.1088/0004-637X/721/2/1014. URL https://ui.adsabs.harvard.edu/abs/2010ApJ...721.1014M. ADS Bibcode: 2010ApJ...721.1014M.

C. McCully, M. Turner, N Volgenau, D. Harbeck, S. Valenti, A. Riba, E. Bachelet, I. W. Snyder, B. Kurczynski, M. Norbury, and R. Street. LCOGT/banzai: Initial Release, June 2018. URL https://zenodo.org/record/1257560.

I. McHardy, S. Connolly, B. Peterson, A. Bieryla, H. Chand, M. Elvis, D. Emmanoulopoulos, E. Falco, P. Gandhi, S. Kaspi, D. Latham, P. Lira, C. McCully, H. Netzer, and M. Uemura. The Origin of UV-optical Variability in AGN and Test of Disc Models: XMM-Newton and ground based observations of NGC4395. *Astronomische Nachrichten*, 337(4-5):500–506, May 2016. ISSN 00046337. doi: 10.1002/asna.201612337. URL http://arxiv.org/abs/1601.00215. arXiv:1601.00215 [astro-ph].

I. A. Meeting and C. Bertout. Structure and emission properties of accretion disks : proceedings of the Sixth IAP Astro-

physics Meeting/IAU Colloquium no 129, July 2-6, 1990, Institut d'astrophysique de Paris. 1991. URL https://www.semanticscholar.org/paper/Structure-and-emission-properties-of-accretion-%3A-of-Meeting-Bertout/8adb419ce36154017b29963521af5f0caf8e4296.

J. M. Miller, A. Zoghbi, M. T. Reynolds, J. Raymond, D. Barret, E. Behar, W. N. Brandt, L. Brenneman, P. Draghis, E. Kammoun, M. J. Koss, A. Lohfink, and D. K. Stern. The Inner Accretion Flow in the Resurgent Seyfert-1.2 AGN Mrk 817. *The Astrophysical Journal Letters*, 911(1):L12, Apr. 2021. ISSN 2041-8205. doi: 10.3847/2041-8213/abef6f. URL https://dx.doi.org/10.3847/2041-8213/abef6f. Publisher: The American Astronomical Society.

C. W. Misner, K. S. Thorne, and J. A. Wheeler. *Gravitation*. Princeton University Press, Oct. 2017. ISBN 978-1-4008-8909-9. Google-Books-ID: zAAuDwAAQBAJ.

R. Morganti. The Many Routes to AGN Feedback. *Frontiers in Astronomy and Space Sciences*, 4, 2017. ISSN 2296-987X. URL https://www.frontiersin.org/articles/10.3389/fspas.2017.00042.

D. Mudd, P. Martini, Y. Zu, C. Kochanek, B. M. Peterson, R. Kessler, T. M. Davis, J. K. Hoormann, A. King, C. Lidman, N. E. Sommer, B. E. Tucker, J. Asorey, S. Hinton, K. Glazebrook, K. Kuehn, G. Lewis, E. Macaulay, A. Moeller, C. O'Neill, B. Zhang, T. M. C. Abbott, F. B. Abdalla, S. Allam, M. Banerji, A. Benoit-Lévy, E. Bertin, D. Brooks, A. Carnero Rosell, D. Carollo, M. Carrasco Kind, J. Carretero, C. E. Cunha, C. B. D'Andrea, L. N. da Costa, C. Davis, S. Desai, P. Doel, P. Fosalba, J. García-Bellido, E. Gaztanaga, D. W. Gerdes, D. Gruen, R. A. Gruendl, J. Gschwend, G. Gutierrez, W. G. Hartley, K. Honscheid, D. J. James, S. Kuhlmann, N. Kuropatkin, M. Lima, M. A. G. Maia, J. L. Marshall, R. G. McMahon, F. Menanteau, R. Miquel, A. A. Plazas, A. K. Romer, E. Sanchez, R. Schindler, M. Schubnell, M. Smith, R. C. Smith, M. Soares-Santos, F. Sobreira, E. Suchyta,

M. E. C. Swanson, G. Tarle, D. Thomas, D. L. Tucker, A. R. Walker, and DES Collaboration. Quasar Accretion Disk Sizes from Continuum Reverberation Mapping from the Dark Energy Survey. *The Astrophysical Journal*, 862: 123, Aug. 2018. ISSN 0004-637X. doi: 10.3847/1538-4357/aac9bb. URL `https://ui.adsabs.harvard.edu/abs/2018ApJ...862..123M`. ADS Bibcode: 2018ApJ...862..123M.

R. Narayan and I. Yi. Advection-dominated Accretion: Underfed Black Holes and Neutron Stars. *The Astrophysical Journal*, 452:710, Oct. 1995. ISSN 0004-637X. doi: 10.1086/176343. URL `https://ui.adsabs.harvard.edu/abs/1995ApJ...452..710N`. ADS Bibcode: 1995ApJ...452..710N.

H. Netzer. Revisiting the Unified Model of Active Galactic Nuclei. *Annual Review of Astronomy and Astrophysics*, 53(1):365–408, Aug. 2015. ISSN 0066-4146, 1545-4282. doi: 10.1146/annurev-astro-082214-122302. URL `https://www.annualreviews.org/doi/10.1146/annurev-astro-082214-122302`.

J. M. M. Neustadt, C. S. Kochanek, J. Montano, J. Gelbord, A. J. Barth, G. De Rosa, G. A. Kriss, E. M. Cackett, K. Horne, E. A. Kara, H. Landt, H. Netzer, N. Arav, M. C. Bentz, E. D. Bonta, M. Dehghanian, P. Du, R. Edelson, G. J. Ferland, C. Fian, T. Fischer, M. R. Goad, D. H. G. Buitrago, V. Gorjian, C. J. Grier, P. B. Hall, Y. Homayouni, C. Hu, D. Ilic, M. D. Joner, J. Kaastra, S. Kaspi, K. T. Korista, A. B. Kovacevic, C. Lewin, Y.-R. Li, I. M. McHardy, M. Mehdipour, J. A. Miller, C. Panagiotou, E. Partington, R. Plesha, R. W. Pogge, L. C. Popovic, D. Proga, T. Storchi-Bergmann, D. Sanmartim, M. R. Siebert, M. Signorini, M. Vestergaard, F. Zaidouni, and Y. Zu. AGN STORM 2. VI. Mapping Temperature Fluctuations in the Accretion Disk of Mrk 817, Oct. 2023. URL `http://arxiv.org/abs/2310.01497`. arXiv:2310.01497 [astro-ph].

F. Pacucci, P. Natarajan, M. Volonteri, N. Cappelluti, and C. M. Urry. Conditions for Optimal Growth of Black Hole Seeds. *The Astrophysical Journal*, 850:L42, Dec. 2017. ISSN 0004-637X. doi: 10.3847/2041-8213/aa9aea. URL

https://ui.adsabs.harvard.edu/abs/2017ApJ...850L..42P. ADS Bibcode: 2017ApJ...850L..42P.

X. Pan, H. Zhou, C. Yang, L. Sun, P. S. Smith, T. Ji, N. Jiang, P. Jiang, W. Liu, H. Lu, X. Shi, X. Dai, and S. Zhang. Mrk 1239: a Type-2 Counterpart of Narrow-line Seyfert-1? *The Astrophysical Journal*, 912(2):118, May 2021. ISSN 0004-637X, 1538-4357. doi: 10.3847/1538-4357/abf148. URL https://iopscience.iop.org/article/10.3847/1538-4357/abf148.

B. M. Peterson. *An Introduction to Active Galactic Nuclei*. Feb. 1997. URL https://ui.adsabs.harvard.edu/abs/1997iagn.book.....P. Publication Title: An introduction to active galactic nuclei ADS Bibcode: 1997iagn.book.....P.

B. M. Peterson. *Variability of Active Galactic Nuclei*. eprint: arXiv:astro-ph/0109495, Jan. 2001. doi: 10.1142/9789812811318_0002. URL https://ui.adsabs.harvard.edu/abs/2001sac..conf....3P. Conference Name: Advanced Lectures on the Starburst-AGN Pages: 3 ADS Bibcode: 2001sac..conf....3P.

B. M. Peterson, I. Wanders, K. Horne, S. Collier, T. Alexander, S. Kaspi, and D. Maoz. On Uncertainties in Cross-Correlation Lags and the Reality of Wavelength-Dependent Continuum Lags in Active Galactic Nuclei. *Publications of the Astronomical Society of the Pacific*, 110(748):660–670, June 1998. ISSN 0004-6280, 1538-3873. doi: 10.1086/316177. URL http://arxiv.org/abs/astro-ph/9802103. arXiv:astro-ph/9802103.

M. Polletta, M. Tajer, L. Maraschi, G. Trinchieri, C. J. Lonsdale, L. Chiappetti, S. Andreon, M. Pierre, O. Le Fèvre, G. Zamorani, D. Maccagni, O. Garcet, J. Surdej, A. Franceschini, D. Alloin, D. L. Shupe, J. A. Surace, F. Fang, M. Rowan-Robinson, H. E. Smith, and L. Tresse. Spectral Energy Distributions of Hard X-Ray Selected Active Galactic Nuclei in the XMM-Newton Medium Deep Survey. *The Astrophysical Journal*, 663:81–102, July 2007. ISSN

0004-637X. doi: 10.1086/518113. URL https://ui.adsabs.harvard.edu/abs/2007ApJ...663...81P. ADS Bibcode: 2007ApJ...663...81P.

T. S. Poole, A. A. Breeveld, M. J. Page, W. Landsman, S. T. Holland, P. Roming, N. P. M. Kuin, P. J. Brown, C. Gronwall, S. Hunsberger, S. Koch, K. O. Mason, P. Schady, D. vanden Berk, A. J. Blustin, P. Boyd, P. Broos, M. Carter, M. M. Chester, A. Cucchiara, B. Hancock, H. Huckle, S. Immler, M. Ivanushkina, T. Kennedy, F. Marshall, A. Morgan, S. B. Pandey, M. de Pasquale, P. J. Smith, and M. Still. Photometric calibration of the Swift ultraviolet/optical telescope. *Monthly Notices of the Royal Astronomical Society*, 383:627–645, Jan. 2008. ISSN 0035-8711. doi: 10.1111/j.1365-2966.2007.12563.x. URL https://ui.adsabs.harvard.edu/abs/2008MNRAS.383..627P. ADS Bibcode: 2008MNRAS.383..627P.

F. Pozo Nuñez, C. Bruckmann, S. Deesamutara, B. Czerny, S. Panda, A. P. Lobban, G. Pietrzyński, and K. L. Polsterer. Modelling photometric reverberation mapping data for the next generation of big data surveys. Quasar accretion discs sizes with the LSST. *Monthly Notices of the Royal Astronomical Society*, 522: 2002–2018, June 2023. ISSN 0035-8711. doi: 10.1093/mnras/stad286. URL https://ui.adsabs.harvard.edu/abs/2023MNRAS.522.2002P. ADS Bibcode: 2023MNRAS.522.2002P.

P. Rafanelli and C. Bonoli. Observations of emission line galaxies. II. The Seyfert galaxies MKN 1239, MKN 1298. *Astronomy and Astrophysics*, 131:186–191, Feb. 1984. ISSN 0004-6361. URL https://ui.adsabs.harvard.edu/abs/1984A&A...131..186R. ADS Bibcode: 1984A&A...131..186R.

Y. E. Rashed, A. Eckart, M. Valencia-S., M. García-Marín, G. Busch, J. Zuther, M. Horrobin, and H. Zhou. Line and continuum variability in active galaxies. *Monthly Notices of the Royal Astronomical Society*, 454(3):2918–2945, Dec. 2015. ISSN 0035-8711. doi: 10.1093/mnras/stv2066. URL https://doi.org/10.1093/mnras/stv2066.

J. A. Regan, T. P. Downes, M. Volonteri, R. Beckmann, A. Lupi, M. Trebitsch, and Y. Dubois. Super-Eddington accretion and feedback from the first massive seed black holes. *Monthly Notices of the Royal Astronomical Society*, 486(3): 3892–3906, July 2019. ISSN 0035-8711, 1365-2966. doi: 10.1093/mnras/stz1045. URL https://academic.oup.com/mnras/article/486/3/3892/5475131.

G. T. Richards, M. Lacy, L. J. Storrie-Lombardi, P. B. Hall, S. C. Gallagher, D. C. Hines, X. Fan, C. Papovich, D. E. Vanden Berk, G. B. Trammell, D. P. Schneider, M. Vestergaard, D. G. York, S. Jester, S. F. Anderson, T. Budavári, and A. S. Szalay. Spectral Energy Distributions and Multiwavelength Selection of Type 1 Quasars. *The Astrophysical Journal Supplement Series*, 166:470–497, Oct. 2006. ISSN 0067-0049. doi: 10.1086/506525. URL https://ui.adsabs.harvard.edu/abs/2006ApJS..166..470R. ADS Bibcode: 2006ApJS..166..470R.

A. Rodríguez-Ardila and X. Mazzalay. The near-infrared spectrum of Mrk 1239: direct evidence of the dusty torus? *Monthly Notices of the Royal Astronomical Society*, 367:L57–L61, Mar. 2006. ISSN 0035-8711. doi: 10.1111/j.1745-3933.2006.00139.x. URL https://ui.adsabs.harvard.edu/abs/2006MNRAS.367L..57R. ADS Bibcode: 2006MNRAS.367L..57R.

G. B. Rybicki and J. T. Kleyna. Study of Reverberation Lags and Spreads in NGC 5548. 69:85, Jan. 1994. URL https://ui.adsabs.harvard.edu/abs/1994ASPC...69...85R. Conference Name: Reverberation Mapping of the Broad-Line Region in Active Galactic Nuclei ADS Bibcode: 1994ASPC...69...85R.

Y. Sakata, T. Minezaki, Y. Yoshii, Y. Kobayashi, S. Koshida, T. Aoki, K. Enya, H. Tomita, M. Suganuma, Y. K. Uchimoto, and S. Sugawara. LONG-TERM OPTICAL CONTINUUM COLOR VARIABILITY OF NEARBY ACTIVE GALACTIC NUCLEI. *The Astrophysical Journal*, 711(1):461, Feb. 2010. ISSN 0004-637X. doi: 10.1088/0004-637X/711/1/461. URL https://dx.doi.org/10.1088/0004-637X/711/1/461. Publisher: The American Astronomical Society.

E. E. Salpeter. Accretion of Interstellar Matter by Massive Objects. *The Astrophysical Journal*, 140:796, Aug. 1964. ISSN 0004-637X, 1538-4357. doi: 10.1086/147973. URL http://adsabs.harvard.edu/doi/10.1086/147973.

A. Savitzky and M. J. E. Golay. Smoothing and Differentiation of Data by Simplified Least Squares Procedures. *Analytical Chemistry*, 36(8):1627–1639, July 1964. ISSN 0003-2700. doi: 10.1021/ac60214a047. URL https://doi.org/10.1021/ac60214a047. Publisher: American Chemical Society.

E. F. Schlafly and D. P. Finkbeiner. Measuring Reddening with Sloan Digital Sky Survey Stellar Spectra and Recalibrating SFD. *The Astrophysical Journal*, 737: 103, Aug. 2011. ISSN 0004-637X. doi: 10.1088/0004-637X/737/2/103. URL https://ui.adsabs.harvard.edu/abs/2011ApJ...737..103S. ADS Bibcode: 2011ApJ...737..103S.

A. Secunda, J. E. Greene, Y.-F. Jiang, P. Z. Yao, and A. Zoghbi. Negative Lags on the Viscous Timescale in Quasar Photometry and Prospects for Detecting More with LSST. *The Astrophysical Journal*, 956:81, Oct. 2023. ISSN 0004-637X. doi: 10.3847/1538-4357/ace7d2. URL https://ui.adsabs.harvard.edu/abs/2023ApJ...956...81S. ADS Bibcode: 2023ApJ...956...81S.

N. I. Shakura and R. A. Sunyaev. Black holes in binary systems. Observational appearance. *Astronomy and Astrophysics*, 24:337–355, 1973. ISSN 0004-6361. URL https://ui.adsabs.harvard.edu/abs/1973A&A....24..337S/abstract.

D. Starkey, K. Horne, M. M. Fausnaugh, B. M. Peterson, M. C. Bentz, C. S. Kochanek, K. D. Denney, R. Edelson, M. R. Goad, G. D. Rosa, M. D. Anderson, P. Arévalo, A. J. Barth, C. Bazhaw, G. A. Borman, T. A. Boroson, M. C. Bottorff, W. N. Brandt, A. A. Breeveld, E. M. Cackett, M. T. Carini, K. V. Croxall, D. M. Crenshaw, E. D. Bontà, A. D. Lorenzo-Cáceres, M. Dietrich, N. V. Efimova, J. Ely, P. A. Evans, A. V. Filippenko, K. Flatland, N. Gehrels, S. Geier, J. M. Gelbord, L. Gonzalez, V. Gorjian, C. J. Grier, D. Grupe, P. B. Hall, S. Hicks, D. Horenstein, T. Hutchison, M. Im, J. J. Jensen, M. D. Joner,

J. Jones, J. Kaastra, S. Kaspi, B. C. Kelly, J. A. Kennea, S. C. Kim, M. Kim, S. A. Klimanov, K. T. Korista, G. A. Kriss, J. C. Lee, D. C. Leonard, P. Lira, F. MacInnis, E. R. Manne-Nicholas, S. Mathur, I. M. McHardy, C. Montouri, R. Musso, S. V. Nazarov, R. P. Norris, J. A. Nousek, D. N. Okhmat, A. Pancoast, J. R. Parks, L. Pei, R. W. Pogge, J.-U. Pott, S. E. Rafter, H.-W. Rix, D. A. Saylor, J. S. Schimoia, K. Schnülle, S. G. Sergeev, M. H. Siegel, M. Spencer, H.-I. Sung, K. G. Teems, C. S. Turner, P. Uttley, M. Vestergaard, C. Villforth, Y. Weiss, J.-H. Woo, H. Yan, A. S. Young, W. Zheng, and Y. Zu. SPACE TELESCOPE AND OPTICAL REVERBERATION MAPPING PROJECT.VI. REVERBERATING DISK MODELS FOR NGC 5548. *The Astrophysical Journal*, 835(1):65, Jan. 2017. ISSN 1538-4357. doi: 10.3847/1538-4357/835/1/65. URL `https://iopscience.iop.org/article/10.3847/1538-4357/835/1/65`.

D. A. Starkey, J. Huang, K. Horne, and D. N. C. Lin. Rimmed and rippled accretion disc models to explain AGN continuum lags. *Monthly Notices of the Royal Astronomical Society*, 519:2754–2768, Feb. 2023. ISSN 0035-8711. doi: 10.1093/mnras/stac3579. URL `https://ui.adsabs.harvard.edu/abs/2023MNRAS.519.2754S`. ADS Bibcode: 2023MNRAS.519.2754S.

M. Suganuma, Y. Yoshii, Y. Kobayashi, T. Minezaki, K. Enya, H. Tomita, T. Aoki, S. Koshida, and B. A. Peterson. Reverberation Measurements of the Inner Radius of the Dust Torus in Nearby Seyfert 1 Galaxies. *The Astrophysical Journal*, 639(1):46, Mar. 2006. ISSN 0004-637X. doi: 10.1086/499326. URL `https://iopscience.iop.org/article/10.1086/499326/meta`. Publisher: IOP Publishing.

W.-H. Sun and M. A. Malkan. Fitting improved accretion disk models to the multiwavelength continua of quasars and active galactic nuclei. *The Astrophysical Journal*, 346:68, Nov. 1989. ISSN 0004-637X, 1538-4357. doi: 10.1086/167986. URL `http://adsabs.harvard.edu/doi/10.1086/167986`.

J. Thorne. Reverberation Mapping of the Accretion Discs in the Quasars 3C 273 and 1H 2106-099. Dec. 2022.

S. Valenti, D. A. Howell, M. D. Stritzinger, M. L. Graham, G. Hosseinzadeh, I. Arcavi, L. Bildsten, A. Jerkstrand, C. McCully, A. Pastorello, A. L. Piro, D. Sand, S. J. Smartt, G. Terreran, C. Baltay, S. Benetti, P. Brown, A. V. Filippenko, M. Fraser, D. Rabinowitz, M. Sullivan, and F. Yuan. The diversity of Type II supernova versus the similarity in their progenitors. *Monthly Notices of the Royal Astronomical Society*, 459(4):3939–3962, July 2016. ISSN 0035-8711. doi: 10.1093/mnras/stw870. URL `https://doi.org/10.1093/mnras/stw870`.

L. M. Winter, C. Danforth, R. Vasudevan, W. N. Brandt, J. Scott, C. Froning, B. Keeney, J. M. Shull, S. Penton, R. Mushotzky, D. P. Schneider, and N. Arav. Ultraviolet and X-ray Variability of the Seyfert 1.5 Galaxy Markarian 817. *The Astrophysical Journal*, 728:28, Feb. 2011. ISSN 0004-637X. doi: 10.1088/0004-637X/728/1/28. URL `https://ui.adsabs.harvard.edu/abs/2011ApJ...728...28W`. ADS Bibcode: 2011ApJ...728...28W.

Q. Yu and S. Tremaine. Observational constraints on growth of massive black holes. *Monthly Notices of the Royal Astronomical Society*, 335(4):965–976, Oct. 2002. ISSN 0035-8711, 1365-2966. doi: 10.1046/j.1365-8711.2002.05532.x. URL `https://academic.oup.com/mnras/article/335/4/965/963932`.

A. Zoghbi, J. M. Miller, and E. Cackett. A Hard Look At Relativistic Reverberation in MCG-5-23-16 & SWIFT J2127.4+5654: Testing the Lamp-Post Model. *The Astrophysical Journal*, 912(1):42, May 2021. ISSN 0004-637X, 1538-4357. doi: 10.3847/1538-4357/abebd9. URL `http://arxiv.org/abs/2103.04994`. arXiv:2103.04994 [astro-ph].

Y. Zu, C. S. Kochanek, and B. M. Peterson. An Alternative Approach to Measuring Reverberation Lags in Active Galactic Nuclei. *The Astrophysical Journal*, 735:80, July 2011. ISSN 0004-637X. doi: 10.1088/0004-637X/735/2/80. URL

https://ui.adsabs.harvard.edu/abs/2011ApJ...735...80Z. ADS Bibcode: 2011ApJ...735...80Z.